

**Extraction of jet properties from two particle azimuthal correlations in
pp and AuAu collisions at $\sqrt{s_{NN}} = 200$ GeV**

by

Paul Constantin

A thesis submitted to the graduate faculty
in partial fulfillment of the requirements for the degree of
DOCTOR OF PHILOSOPHY

Major: Nuclear Physics

Program of Study Committee:
John G. Lajoie, Major Professor
Craig A. Ogilvie
Marzia Rosati
James Cochran
Frank Krennrich

Iowa State University
Ames, Iowa
2004

Graduate College
Iowa State University

This is to certify that the doctoral thesis of
Paul Constantin
has met the thesis requirements of Iowa State University

Major Professor

For the Major Program

DEDICATION

To my wife Ileana and my daughter Maria.

ACKNOWLEDGEMENTS

First I would like to gratefully acknowledge my advisor, Professor John Lajoie, for his support and encouragement during my graduate studies. I was always inspired by his enthusiasm for the field. He helped me develop the sense of confidence necessary in becoming an accomplished scientist. His questions and observations provided valuable guidance for the analysis presented here.

Dr. Jan Rak was the closest collaborator and friend during the latest three years of graduate studies, especially in the period spent at the Brookhaven National Laboratory. The entire work presented in this thesis is the result of our collaboration. I would like to express my gratitude for his patience during the long hours of discussions which taught me so many things, both as a physicist and as a person.

I also thank all the members of the Nuclear Physics Group at Iowa State University: Professors Craig Ogilvie, Marzia Rosati, and John Hill, Dr. Alexander Lebedev, and fellow graduate students Nathan Grau and Hua Pei. Their suggestions, in private or as a part of our regular group meetings, have led to significant contributions to my work.

Finally, I would like to acknowledge all the members of the Hard Scattering and Photon Physics Working Group of the PHENIX collaboration and especially those who taught me so many things by sharing their vast expertise with me: Michael Tannenbaum, Paul Stankus, Brian Cole, Ajitanand Nuggehali, and Jiangyong Jia.

ABSTRACT

Two particle azimuthal correlation functions measured in pp and $AuAu$ collisions at $\sqrt{s_{NN}}=200$ GeV at midrapidity with the central arms of the PHENIX detector are analyzed in order to extract the properties of hadronic jets produced in QCD vacuum and highly excited QCD media.

Already, the published results on hadron spectra at high transverse momentum (p_T) in pp [13], dAu [16] and $AuAu$ [14] collisions at RHIC energies gave definitive proof for the discovery of hadronic jet quenching.

We use the method of two particle azimuthal correlation functions to gain more detailed information about this phenomenon, by extracting quantities like the jet shape parameters j_T and k_T , the jet conditional yields (number of associated hadrons per high p_T trigger hadron from jet fragmentation) and the jet fragmentation function.

The analysis of pp data starts with the measurement of the vacuum fragmentation function from which the p_T dependence of the mean fragmentation momentum fraction $\langle z \rangle$ is extracted. We obtain a constant value of $\langle z \rangle = 0.74 \pm 0.02$ for p_T above 3 GeV/c. Soft (non-perturbative) parton fragmentation becomes significant below 3 GeV/c and the slope of the fragmentation function is p_T dependent in this region. Gaussian fits to jet induced azimuthal correlations are employed to measure the mean jet fragmentation transverse momentum $\langle |j_{Ty}| \rangle = 359 \pm 11$ (stat) ± 6 (syst) MeV/c and the mean partonic transverse momentum $\langle |k_{Ty}| \rangle = 964 \pm 49$ (stat) ± 16 (syst) MeV/c.

The analysis of $AuAu$ data is based on azimuthal correlation functions between charged hadrons in the 1.5-3 GeV/c and 3-5 GeV/c p_T regions in five classes of collision centrality. The mean jet fragmentation transverse momentum $\langle |j_{Ty}| \rangle$ is centrality independent and consistent with the value in pp data mentioned above. Even though the statistical and systematical errors associated with the extracted mean partonic transverse momentum $\langle |k_{Ty}| \rangle$ (multiplied by $\langle z_{trigg} \rangle$) are rather large, a strong broadening with the

centrality is observed. This is an important finding because hadronic jet quenching through energy loss (medium induced gluon radiation) is expected to be accompanied by a broadening effect.

Another important finding is that the jet conditional yields in both the near ($\Delta\phi \sim 0$) and away ($\Delta\phi \sim \pi$) regions exhibit a slightly raising trend with centrality. This was also expected to accompany the jet quenching found at higher p_T based on simple energy conservation considerations.

This detailed study of hadronic jet properties is another piece of the Quark-Gluon Plasma puzzle that RHIC is trying to solve.

TABLE OF CONTENTS

ACKNOWLEDGEMENTS	iv
ABSTRACT	v
LIST OF TABLES	ix
LIST OF FIGURES	x
CHAPTER 1. Introduction	1
1.1 Quark Gluon Plasma	1
1.2 Short Introduction into the Physics of Hadronic Jets	3
1.2.1 The Parton Model and High- p_T Single Inclusive Spectra	3
1.2.2 k_T Effect, j_T Scaling and High- p_T Correlations	5
1.3 Quenching of Hadronic Jets in Quark Gluon Plasma	8
1.3.1 Theory of Jet Quenching and Broadening in QGP	8
1.3.2 Jet Quenching Discovery at RHIC	9
1.4 Thesis Organization	11
CHAPTER 2. Hadronic Jets and Other Sources of Two-Particle Az-	
imuthal Correlations	14
2.1 Definitions of Jet Kinematical Parameters	14
2.2 Derivation of the Equations for Jet Shape Parameters	17
2.2.1 Extraction of $\langle j_{Ty} \rangle$	17
2.2.2 $\langle p_{out} \rangle$ Formula and Extraction of $\langle k_{Ty} \rangle$	18
2.3 Jet Conditional Yields. Jet Fragmentation Function.	21
2.4 Collective Quadrupole Azimuthal Correlations.	23
2.5 Correlation Function with a Jet Source and a Collective Quadrupole Source	24
2.6 Other Sources of Azimuthal Correlations	29

CHAPTER 3. PHENIX Central Arm Detectors	33
3.1 Detector Overview	33
3.2 Global Detectors	34
3.3 Charged Hadron Tracking Detectors	37
3.4 Electromagnetic Calorimeters	43
CHAPTER 4. Data Analysis	46
4.1 Data Selection and Quality Analysis	46
4.1.1 Run and Event Selection	46
4.1.2 Single Particle Selection	49
4.1.3 Particle Pair Selection	51
4.2 Azimuthal Correlation Functions	54
4.2.1 Definition and Normalization	54
4.2.2 Mixed Event Technique	56
4.2.3 Fitting Methods for $AuAu$ analysis	57
4.3 Acceptance and Efficiency Corrections.	64
CHAPTER 5. Results	66
5.1 Jet Fragmentation Function in pp Collisions	66
5.2 Jet Shape Parameters	70
5.2.1 Jet Shape Parameters in pp Collisions	70
5.2.2 Jet Shape Parameters in $AuAu$ Collisions	74
5.3 Jet Conditional Yields in $AuAu$ Collisions	78
CHAPTER 6. Conclusions	81
APPENDIX A. Conditional Mean Fragmentation Momentum Fraction	86
APPENDIX B. The Seagull Effect	88
APPENDIX C. Correlation Functions in pp Collisions	90
APPENDIX D. Systematic Checks of pp Results	94
D.1 The Systematic Effects of Background Correlations	94
D.2 The Systematic Effects of the Analysis Method	95
D.3 Check of the Gaussian Jet Profile Assumption	96
APPENDIX E. Correlation Functions in $AuAu$ Collisions	101
APPENDIX F. Systematic Errors of $AuAu$ Results	104
BIBLIOGRAPHY	107

LIST OF TABLES

3.1	Pad Chamber Parameters	40
4.1	ERT trigger $\langle p_T \rangle$ shift	49
5.1	p_T dependence of $\langle x_E \rangle$ and $\langle z_{trigg} \rangle$	69
5.2	Fit results for $h^\pm - h^\pm$ correlations in pp collisions	71
5.3	$\langle j_{Ty} \rangle$ and $\langle k_{Ty} \rangle$ in pp collisions	74
5.4	V_2 from MJAP method	75
5.5	Final jet shape parameters in $AuAu$ collisions	76
5.6	Final conditional yields in $AuAu$ collisions	78
D.1	Systematic study of near angle width in pp collisions	97
D.2	Systematic study of away angle width in pp collisions	97
D.3	Example of near angle RMS calculation	99
D.4	Example of away angle RMS calculation	99
F.1	Near angle width variation with V_2	105
F.2	Away angle width variation with V_2	105
F.3	Near angle area variation with V_2	106
F.4	Away angle area variation with V_2	106

LIST OF FIGURES

1.1	The high- p_T pion cross section at ISR	5
1.2	Fragmentation function universality	6
1.3	Dijet acoplanarity at ISR	7
1.4	Jet Quenching at RHIC	10
1.5	x_T scaling at RHIC	12
2.1	Topology of a dijet event	16
2.2	Topology of a dijet event with $j_T = 0$ for both hadrons. . .	18
2.3	Topology of a dijet event with $j_T \neq 0$ only for the trigger hadron	19
2.4	Topology of a dijet event with $j_T \neq 0$ for the both hadrons	20
3.1	The PHENIX detector layout	35
3.2	Centrality Determination with PHENIX Global Detectors	38
3.3	The PHENIX Magnet	39
3.4	Charged Particle Tracking	42
4.1	$\langle p_T \rangle$ shift in ERT triggered events	48
4.2	Charged Hadron Combinatorial Background	51
4.3	Drift Chamber "Ghost" Tracks Cut	52
4.4	Pad Chamber Resolution Pair Cuts	53
4.5	$\pi/2$ Subtracted Correlation Functions	59
4.6	The Method of Minimum Jet Amplitude Point - Example	62
4.7	The Method of Minimum Jet Amplitude Point - Simula- tions	63
4.8	The efficiency correction for charged hadrons	65
5.1	Jet fragmentation function in vacuum	67
5.2	Parametrization of the π^0 spectrum	68

5.3	Extraction of the parton spectrum from the measured π^0 spectrum	69
5.4	p_T dependence of $\langle z \rangle$	70
5.5	Extraction of $\langle j_{Ty} \rangle$ and $\langle z \rangle \langle k_{Ty} \rangle$	72
5.6	Comparison between Gaussian widths in π^0 - h^\pm and h^\pm - h^\pm azimuthal correlations	73
5.7	$\langle k_{Ty} \rangle$ result	73
5.8	V_2 from MJAP method	75
5.9	Jet shape parameters in $AuAu$ collisions from MJAP method	76
5.10	Final jet shape parameters in $AuAu$ collisions	77
5.11	Near and away conditional yields from MJAP method	79
5.12	Near and away final conditional yields	80
6.1	Comparison with pp world data on k_T	82
6.2	Comparison between k_T in pp and dAu collisions	83
A.1	Monte Carlo $\langle z \rangle$ study	87
B.1	The Seagull Effect	89
C.1	$h^\pm - h^\pm$ fixed correlations and fits in pp collisions	91
C.2	$h^\pm - h^\pm$ assorted correlations and fits in pp collisions	92
C.3	x_E distributions in pp collisions	93
D.1	Charge dependence of the Gaussian widths in pp collisions	95
D.2	Invariant mass distributions	96
D.3	Systematic study of Gaussian widths in pp collisions	98
D.4	Example of RMS calculation	100
E.1	$h^\pm - h^\pm$ $AuAu$ assorted correlations: first step MJAP fit	102
E.2	$h^\pm - h^\pm$ $AuAu$ assorted correlations: second step MJAP fit	103

CHAPTER 1. Introduction

1.1 Quark Gluon Plasma

The building blocks of the universe as we see it now are protons, neutrons, and electrons; the first two belong to the large family of hadrons. All hadrons are held together by one of the four fundamental forces in nature - the strong force. For this reason, understanding its properties has become one of the major quests of contemporary physics.

Although there are multiple other theoretical approaches (string theory being a notable one), the Standard Model with its component **Quantum Chromo Dynamics** (QCD) has been proven to be the most successful in explaining the wealth of experimental data accumulated over the last three decades in various fields like particle physics, nuclear physics and astrophysics. QCD describes hadrons as colorless combinations of fundamental particles called quarks bound together by the strong force, which is mediated by gauge bosons known as gluons.

One particular feature of QCD is that not only the quarks carry color charge, but also the gluons; this allows them to interact with each other and generate additional gluons. As a consequence, the strength of the interaction quickly increases with distance or, equivalently, decreases with 4-momentum transfer Q^2 :

$$\alpha_S(Q^2) = \frac{\alpha(\mu^2)}{1 + \alpha(\mu^2) \frac{33-2n_f}{12\pi} \ln(-\frac{Q^2}{\mu^2})} \quad (1.1)$$

Note that $\alpha_S(Q^2 \rightarrow 0) \rightarrow 0$ ('*asymptotic freedom*').

Hence, two classes of processes mediated by the strong force arise:

- high- Q^2 processes (above $2 - 3 GeV^2$), also called **hard QCD processes**, are characterized by $\alpha_S(Q^2) \ll 1$ which allows calculations to be performed within the perturbative framework;

- low- Q^2 processes (below $2 - 3 GeV^2$), also called **soft QCD processes**, for which analytical calculations are much more difficult.

Many of the QCD phenomena related to the *confinement* of quarks in hadrons, generation of hadronic masses by dynamical spontaneous breaking of *chiral symmetry*, and other fundamental concepts of the Standard Model belong to the class of soft QCD processes. In this regime, perturbation methods cannot be employed.

Nonetheless, during the last years, the method of *lattice QCD simulations* [40] has gained a lot of momentum with the increase in computing power and development of new techniques. For the first time, realistic first-principle QCD calculations are performed in the soft QCD regime.

Lattice simulations predict that, at distance scales comparable with the hadronic size ($\approx 1 fm$), quarks interact with an effective potential that goes approximately linearly with the distance:

$$V_{qq}(\vec{r}; T) \approx k(T) \cdot r - \frac{4\alpha_S}{3r} \exp\left(-\frac{r}{\lambda_D(T)}\right) \quad (1.2)$$

where $\lambda_D \propto 1/T$ is the Debye screening length. Also, above a critical temperature of about $T_c \approx 150 - 170 MeV$, the system becomes unbound - $k(T > T_c) \approx 0$. Hence, a hadronic system heated above this temperature would “melt” into a soup of freely roaming quarks and gluons. Such a state of matter that reached equilibrium has been dubbed the **Quark Gluon Plasma** (QGP). Also, around the same critical temperature as for the quark *deconfinement* phase transition, lattice calculations predict another phase transition - the *chiral symmetry restoration* - to a QCD state made of massless quarks.

The experimental search for all the above soft QCD phenomena, and most notably for the QGP, has become the main subject of **Relativistic Heavy Ion Collisions** (RHIC). Nuclei are hadronic systems which, when collided at sufficient energy, are expected to produce the temperature and density conditions favorable for such phase transitions.

However, since quarks and gluons cannot escape freely from a QGP, it cannot be observed directly; rather, “signatures” of the transition from a hadronic system to a QGP (and back) are looked for through the large amount of particle debris of the collision. Some of them are: hadronic jet quenching, J/Ψ (charmonium) suppression, dilepton production, strangeness enhance-

ment, collective flow, direct photon production, Hanbury-Brown-Twiss (HBT) effect. Because of the complexity of the phenomena happening in a heavy ion collision, only a complete study of all these signatures can give a detailed description of the state of matter formed. For a brief description of them, see [27].

The work presented in this thesis is related to one of the proposed signatures of QGP formation - **hadronic jet quenching**.

1.2 Short Introduction into the Physics of Hadronic Jets

The observation of hadronic jets was one of the main experimental results leading to the development of QCD. This section briefly reminds us what are the basic concepts of hadronic jet physics and how they were introduced in the 70s and 80s.

By the mid 60s, experimental results of hadronic inclusive spectra were mostly at low $p_T (< 1\text{GeV}/c)$, for processes initiated by photons, leptons or hadrons. In this kinematical region, they had an exponential shape $E d^3\sigma/dp^3 \sim e^{-6p_T}$, independent of \sqrt{s} or p_{\parallel} . Also, hadrons emerged with uniform angular distributions. Hence, it was no surprise that statistical models worked fairly well.

1.2.1 The Parton Model and High- p_T Single Inclusive Spectra

In 1968, Bjorken discovered that the Deeply Inelastic Scattering (DIS) *structure function scales* [28], i.e. does not depend on the momentum transfer Q^2 and the virtual photon energy ν , but rather on their ratio:

$$F_2(Q^2, \nu) = F_2(x), \quad x \equiv \frac{Q^2}{2M\nu} \quad (1.3)$$

This led him to the introduction of the *parton model for protons (hadrons)*: the proton is composed of point-like particles called "partons". $F_2(x)$ gives the probability for a constituent parton to carry a fraction x of the hadron momentum.

Based on the parton model, Berman, Bjorken and Kogut (BBK) [29] predict that:

- the high- p_T hadronic cross section becomes power law, greatly exceeding the statistical exponential cross section:

$$E \frac{d^3\sigma}{dp^3} = \frac{4\pi\alpha^2}{p_T^n} F(x_1, x_2) \quad (1.4)$$

where $x_1 \equiv -\hat{u}/\hat{s}$, $x_2 \equiv -\hat{t}/\hat{s}$ are the two partons' x momentum fractions. They predicted the index $n = 4$ since partons interacted electromagnetically in their model (via single photon exchange).

- "final state hadrons emerge into corelike distributions along the virtual photon direction" or the scattered parton direction producing the already well known *hadronic jets*. They introduce the *fragmentation function* $G(x)$, $x \equiv p_{hadron}/p_{parton}$, which is \sqrt{s} (or, Q^2) -independent and universal (independent of the parton's production process): "the existence of $G(x)$ suggests an equality between the number distribution of the final observed hadrons in $e + p \rightarrow h + X$ and $e^+ + e^- \rightarrow h + X$ ".

Experiments at CERN-ISR in 1972-1973, like BS [1] and ABCS [8], measured high- $p_T (> 2\text{GeV}/c)$ pion production and found that, indeed, the low- p_T exponential e^{-6p_T} cross section turns into a power law that scales with $x_T \equiv 2p_T/\sqrt{s}$. However, the rates were much higher than those predicted by BBK suggesting that partons interact via the strong force and not the electromagnetic force. Also, the high- p_T cross section did have the form (1.4), but with $n \approx 8$ (more precisely, 8.24 ± 0.05) and not $n = 4$. The left panel of Fig.(1.1) shows a manifest x_T -scaling of the $p + p \rightarrow \pi^0 + X$ cross section at four different collision energies with an index $n = 8$.

Calahan *et al.* pointed out in 1975 that the index n in (1.4) is not a new scaling of the cross section, being dependent on \sqrt{s} and x_T [31]:

$$E \frac{d^3\sigma}{dp^3} = \frac{1}{p_T^{n(x_T, \sqrt{s})}} F(x_T) = \frac{1}{\sqrt{s}^{n(x_T, \sqrt{s})}} G(x_T) \quad (1.5)$$

CCOR experiments at the same CERN-ISR in 1978 [2] established that, indeed, $n \approx 5$ at higher- p_T : $E d^3\sigma/dp^3 \simeq p_T^{-5.1 \pm 0.4} (1-x)^{12.1 \pm 0.6}$ for $p_T > 7\text{GeV}/c$ and $53 \leq \sqrt{s} \leq 63\text{GeV}$. Right panel of Fig.(1.1) shows a systematic measurement of the power law index n for various x_T and \sqrt{s} values: it starts around 8 – 9 at $x_T \approx 0.1$ and decreases to 5 at $x_T \approx 0.5$; it also decreases with \sqrt{s} .

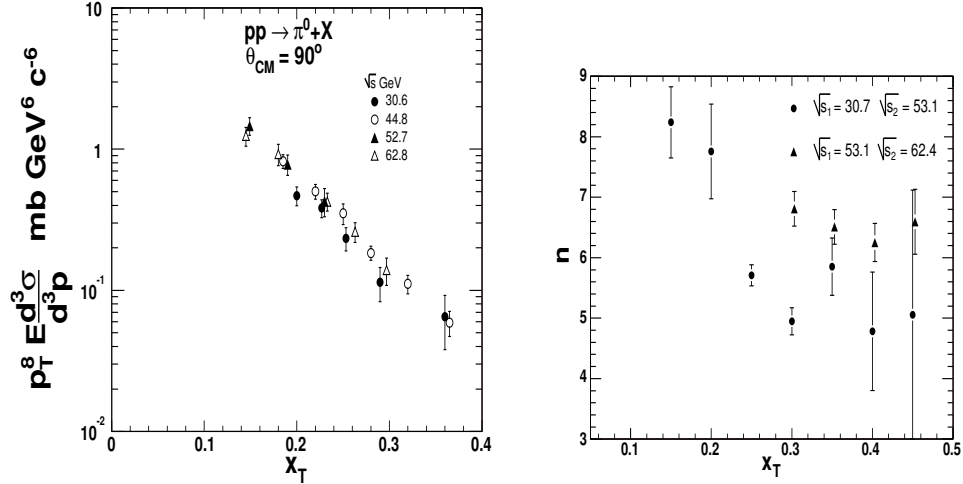


Figure 1.1 Left: $p + p \rightarrow \pi^0 + X$ cross section at $\theta_{CM} \sim 90^\circ$ and $\sqrt{s} = 31, 45, 53, 63 \text{ GeV}$ from [8]; it scales with x_T and has a power index $n = 8$; Right: dependency of the index n on x_T and \sqrt{s} from [2].

The first modern QCD calculations for high- p_T single hadron inclusive cross sections, including $n(x_T, \sqrt{s})$ and $k_T \neq 0$ (see next section), were done in 1978 by Owens *et al.*[32]. Leading order (LO) vector ($J = 1$) gluon exchange generate a power law index $n=4$, hence n is expected to become 4 for hadron spectra from fragmentation of infinite momentum partons; however, higher order corrections are significant even at very large x_T and \sqrt{s} and generate steeper spectra ($n > 4$).

The universality and Q^2 -independence of the fragmentation function has also been tested during same period by comparing the measured fragmentation function in pp collision with measurements in ep and νp collisions. Such a compilation from [33] is presented in the left panel of Fig.(1.2).

1.2.2 k_T Effect, j_T Scaling and High- p_T Correlations

However, calculations using the parton model or leading order QCD did not contain any transverse momentum imbalance k_T of the outgoing partons due to initial state radiation (gluon emission before the hard scattering process).

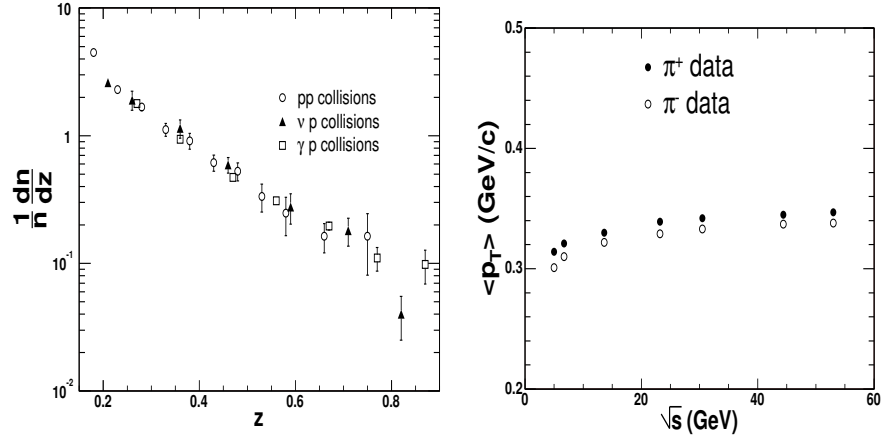


Figure 1.2 Left: collection of parton fragmentation functions from [33] measured in pp and νp collisions; Right: dependence of $\langle p_T \rangle$ on \sqrt{s} from same reference.

The CCHK experiment [7] discovered in 1977 **hadronic jet acoplanarity**: high- p_T hadrons from jet fragmentation had a considerable average transverse momentum component $\langle |p_{out}| \rangle$ out of the plane defined by the beam axis and another high- p_T hadron from the fragmentation of the back-to-back jet (we will define all the jet kinematical parameters in Section 2.1). They proposed that this was due to transverse momentum of partons inside the hadron (" k_T effect").

The k_T phenomenology was subsequently developed by Feynman, Field and Fox in [30]. They attributed it to two components: an "intrinsic transverse momentum" component from confinement inside the hadron which is a constant and to a NLO component due to hard gluon emission which varies with x and Q^2 . They also gave an approximate formula for the dependence of $\langle |p_{out}| \rangle$ on k_T which, with the standard notations in practice now, reads:

$$\langle |p_{out}| \rangle^2 = 2x_E^2 \langle k_T \rangle^2 + (1 + x_E^2) \langle j_T \rangle^2, \quad x_E \equiv -\frac{\vec{p}_T \cdot \vec{p}_{Ttrig}}{p_{Ttrig}^2} \quad (1.6)$$

where p_{Ttrig} is the "trigger" - highest p_T - hadron in the event and j_T is the transverse momentum of the fragment with respect to the parton direction (jet axis). We will come back to this equation in Section 2.2. Fig.(1.3) shows the measured $\langle |p_{out}| \rangle$ dependence on the fragmentation momentum fraction

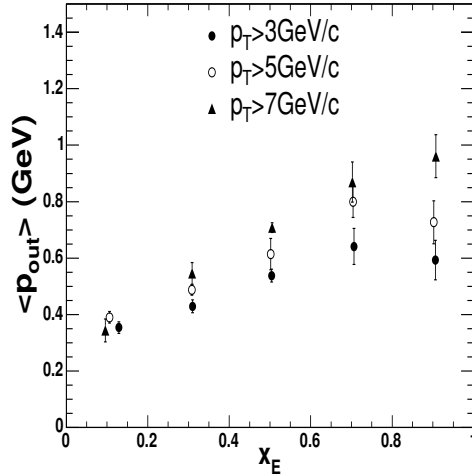


Figure 1.3 Dijet acoplanarity: p_{out} dependence on the fragmentation momentum fraction x_E for several p_T regions from [5].

from [5]. According to Eq.(1.6), the intercept of the $\langle |p_{out}| \rangle^2$ dependence on $\langle x_E \rangle^2$ gives the j_T value, while the slope of this dependence gives the k_T value. The CCOR experiment soon used this dependency to measure the \sqrt{s} and p_T dependence of j_T and k_T [5]. They observed **a slow increase of k_T with \sqrt{s} and p_{Ttrig} and an approximate scaling of j_T with \sqrt{s} and p_{Ttrig}** : all hadrons have $j_T \approx 400 \text{ MeV}$, independent of the collision energy or parton's momentum. This was related to another experimental observation: the mean transverse momentum of hadrons in pp collisions is $\langle p_T \rangle \simeq 340 \text{ MeV}/c$ and depends very weakly on the energy of the collision as shown in the right panel of Fig.(1.2).

A recent compilation of k_T measurements in various hard processes (Drell-Yan, jet-jet or direct photon-jet, etc.) is presented in [34].

Measurements in pA , πA , and γA [9] have shown that k_T **grows with the thickness of the nuclear medium as $A^{1/3}$** . This is attributed to the Cronin effect (multiple soft scattering) which will be introduced in the next Section.

1.3 Quenching of Hadronic Jets in Quark Gluon Plasma

Section 1.1 introduced our goal - the study of QGP -, and section 1.2 introduced our tool - hadronic jets. Now we will present briefly how they are connected and what we already discovered at RHIC about jets in heavy ion collisions.

1.3.1 Theory of Jet Quenching and Broadening in QGP

Hadronic jet quenching via gluon radiation by high momentum partons propagating through a quark-gluon plasma was proposed as a signature in 1982 by Bjorken [35] in a preprint entitled "Energy Loss of Energetic Partons in Quark-Gluon Plasma: Possible Extinction of High p_T Jets in Hadron-Hadron Collisions". He also mentions the possibility of the extreme case of QGP signature events with hard collisions such that one jet is escaping relatively unaffected while the other is fully absorbed.

The first extensive calculations of the energy loss by partons in a QGP were performed in the early 90s by Gyulassy, Wang, and collaborators [36] and Baier, Dokshitzer, Mueller and collaborators [38]. They showed that the average **energy loss** per unit length dE/dx grows linearly with the total length of the medium and its gluon density. This produces a suppression of the high- p_T spectra in heavy ion collisions that increases with the size of the interaction region (collision centrality). They also established the relationship between the energy loss dE/dx of the parton and its **transverse momentum broadening** Δk_T^2 due to multiple scatterings. Jet broadening (increase of the width of the transverse momentum distribution of fragments with respect to its axis), enhanced **acoplanarity** and energy imbalance of back-to-back jets are also among the possible manifestations of these effects.

An energetic parton produced in a hard collision interacts with the medium by emitting a gluon which travels with a mean free path $\lambda > 1/\mu$, which is the range of screened multiple gluon interactions. The medium dependence of this interaction is incorporated in the transport coefficient:

$$\hat{q} \sim \frac{\mu^2}{\lambda} \sim \rho \int d^2 q_T \cdot q_T^2 \frac{d\sigma}{d^2 q_T} \sim \frac{4\pi^2 N_c}{N_c^2 - 1} \alpha_s \rho \cdot x G(x, \hat{q}L) \quad (1.7)$$

where L is the medium thickness, ρ its density, and $xG(x, Q^2)$ the gluon struc-

ture function. All the important quantities described above are related to \hat{q} :

- differential energy loss:

$$-\frac{dE}{dx} = \alpha_s \hat{q} L \quad (1.8)$$

- k_T broadening:

$$\langle k_T^2 \rangle = \hat{q} L \quad (1.9)$$

- gluon saturation momentum scale (see below):

$$Q_s^2 = 2R_A \hat{q} \quad (1.10)$$

In the case of an expanding plasma the energy loss is expected to be at least twice as big compared to the case of a static plasma.

1.3.2 Jet Quenching Discovery at RHIC

One of the first important RHIC results was the discovery of high- p_T hadron suppression [14] [15]. It was quantified using the *nuclear modification factor*:

$$R_{AB}(p_T) \equiv \frac{d^2 N_{AB}/dp_T d\eta}{T_{AB} d^2 \sigma_{pp}/dp_T d\eta} \quad (1.11)$$

where $T_{AB} = \langle N_{coll} \rangle / \sigma_{pp}^{inel}$ is the nuclear thickness function and $\langle N_{coll} \rangle$ is the mean number of binary collisions (estimated with a Glauber model). If the nuclear collision is an incoherent superposition of binary pp collisions (negligible nuclear effects), then $R_{AB} = 1$. So, by definition, R_{AB} measures the modification of the hadronic p_T spectra due to any nuclear effects in AB collisions. A **strong suppression** ($R_{AuAu} \approx 0.2$ for $p_T > 4 \text{ GeV}/c$) has been observed in central 0-10% $AuAu$ collisions at RHIC, as shown in the left panel of Fig.(1.4); it gradually sets on from peripheral collisions, where binary scaling ($R_{AuAu} \approx 1$) is found, to central collisions.

However, this was not yet definitive proof of jet quenching since there are many other effects than final state energy loss that could produce a nuclear modification of high- p_T hadronic spectra:

- *Gluon Saturation Effects* in the initial state of the collision [42] - at low x the gluon wave functions grow until they become comparable with

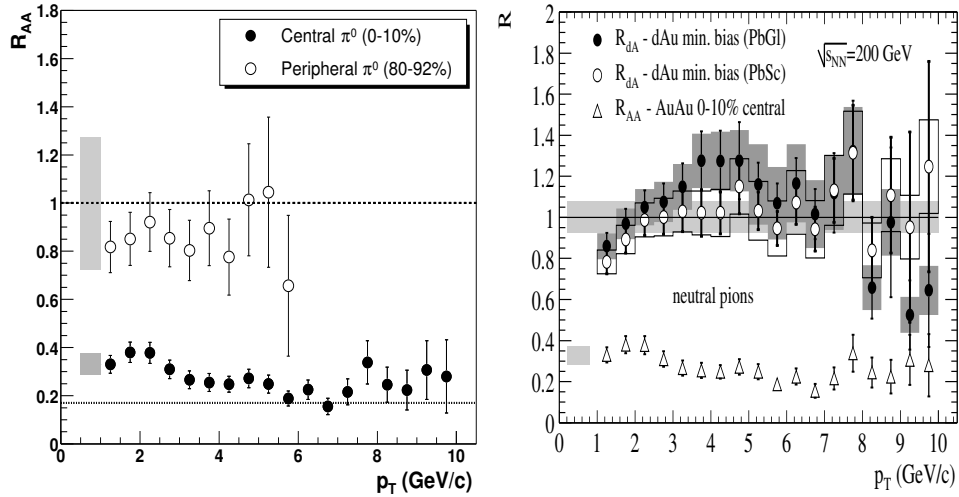


Figure 1.4 Jet Quenching at RHIC: Left Panel - the nuclear modification factor R_{AA} of π^0 spectra in central 0-10% and peripheral 80-92% $AuAu$ collisions exhibits a strong suppression; Right Panel - the nuclear modification factor R_{dAu} of π^0 spectra in minimum bias dAu collisions exhibits a Cronin enhancement.

the size of the nucleus and start to overlap with each other. When this happens (at the gluon saturation momentum scale given by Eq.(1.10)), large coherence effects set on, with deep consequences on the partonic interactions. Most notably, $2 \rightarrow 2$ parton scattering is no longer the leading process, but $2 \rightarrow 1$ gluon fusion ($g + g \rightarrow g$) becomes dominant. High- p_T hadronic spectra are predicted to be suppressed in such cases.

- *Cronin Effect* in the initial state of the collision [10] - multiple soft scattering before the hard scattering increase the transverse momentum of the parton, leading to an enhancement of the hadron spectra at high- p_T ; it leads to an enhancement of high p_T hadronic spectra proportional to $A^{\alpha(p_T)}$, with $\alpha(p_T > 2GeV/c) > 1$:

$$E \frac{d\sigma^{pA}}{d^3p} = E \frac{d\sigma^{pp}}{d^3p} A^{\alpha(p_T)} \quad (1.12)$$

The Cronin effect also produces a k_T increase with the nuclear mass A , as mentioned in the previous Section. This effect also happens in the

final state of the collision if it is cold nuclear matter (like in pA collisions).

- *Gluon Radiation Effect* (energy loss) in the final state of the nuclear collision - described in the previous section.

There is a simple way to disentangle experimentally final and initial state nuclear effects on the spectra: perform the same measurement (same collision energy, centrality, and p_T region) in dAu collisions. All the initial state effects listed above will be present, but no final state effect. Measurements [16] showed that the central dAu spectrum is enhanced ($R_{dAu} \approx 1.2$ in 0-20% centrality), while the peripheral one is in agreement with binary scaling. The right panel of Fig.(1.4) shows the nuclear modification factor of π^0 spectra in minimum bias dAu collisions (as a systematic check, for both electromagnetic calorimeters in PHENIX). This is solid proof that the high- p_T suppression in central $AuAu$ collisions is a final state effect, and hence a proof of **jet quenching** at RHIC.

Finally, the x_T dependence of the high- p_T hadronic spectra was extracted by the PHENIX collaboration [15]. As expected, peripheral collision π^0 spectra at both $\sqrt{s_{NN}} = 130$ and 200 GeV scale with x_T , suggesting that they indeed come from fragmentation of hard scattered partons. More interestingly, even the most central collision spectra were also found to scale with x_T with the same power index $n(x_T, \sqrt{s_{NN}}) = 6.3 \pm 0.6$ in the $0.025 \leq x_T \leq 0.06$ region, as shown in Fig.(1.5). In this kinematical region, partonic energy loss in the QGP preserves x_T scaling, a fact related to the apparent independency of R_{AA} on p_T .

1.4 Thesis Organization

We present the study of hadronic jets in pp and $AuAu$ collisions at $\sqrt{s_{NN}} = 200 \text{ GeV}$ based on the two-particle azimuthal correlation method. We extract more detailed information about their properties in vacuum and hot QCD matter (QGP). A comparison with the results for cold nuclear matter (dAu collisions) is also done.

Chapter 2 gives a detailed description of the sources of azimuthal correlations in high energy collisions. First, we define all the quantities used to describe jets: shape parameters (j_T, k_T), conditional yields, fragmentation

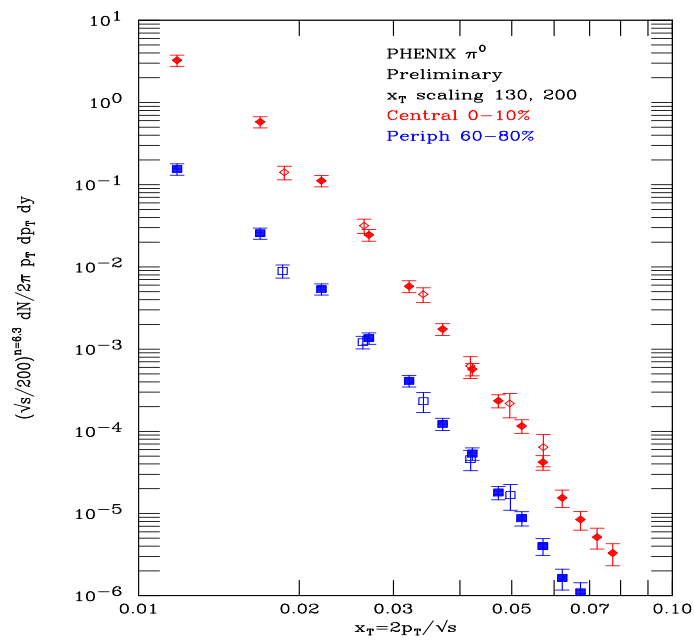


Figure 1.5 x_T scaling of π^0 spectra at RHIC: the $AuAu$ π^0 spectra scale with x_T and have the same power law index $n \approx 6.3$ for both collision energies (130 and 200 GeV) and for all centralities.

function (z and x_E distributions). Then we derive the basic equations that relate these quantities to the azimuthal correlation functions. In the last section, we develop the formalism of azimuthal correlation functions with multiple sources.

Chapter 3 contains a brief description of the PHENIX central arms detectors used in this analysis. We will describe the methods used to derive the physical quantities (event centrality, vertex, and trigger; charged hadron track kinematics, identification, and quality; electromagnetic cluster energy, position, and identification.)

Chapter 4 details the data analysis methods: data selection, analysis technique, and various corrections are presented. The definition and normalization of azimuthal correlation functions are presented. Also, we will discuss in detail the techniques used to extract jet physical quantities from the correlation functions.

Chapter 5 presents the results: the vacuum (pp) fragmentation function, the jet shape parameters in both pp and $AuAu$ collisions, and the centrality dependence of $AuAu$ conditional yields.

Finally, chapter 6 discusses the above results.

CHAPTER 2. Hadronic Jets and Other Sources of Two-Particle Azimuthal Correlations

2.1 Definitions of Jet Kinematical Parameters

We define here the kinematical parameters used to describe a dijet event (two roughly back-to-back hadronic jets generated by the fragmentation of two partons from a hard scattering process) and their relationship with parameters of a two-hadron azimuthal correlation function (CF). Figure (2.1) shows the topology of such an event. The "trigger" hadron has a high transverse momentum $p_{T,trigger}$ and the "associated" hadron has a lower p_T value; on average, the trigger carries a large fraction of its parent parton momentum (≈ 0.8) and also deviates very little from its direction.

Fragmentation Momentum Fraction z is the ratio between the component of fragment's p_T along the direction of its parent parton and parton's p_{Tq} :

$$z \equiv \frac{\vec{p}_T \cdot \vec{p}_{Tq}}{p_{Tq}^2} \quad (2.1)$$

However, since we usually do not have direct access to parton kinematic variables, experimental equivalent quantities are defined with respect to the trigger hadron:

$$x_E \equiv -\frac{\vec{p}_T \cdot \vec{p}_{Ttrigger}}{p_{Ttrigger}^2} \quad (2.2)$$

where the "-" sign is used to make x_E positively defined for hadrons from back-to-back jets.

Fragmentation Transverse Momentum j_{Ty} (1-D component) is the component of fragment's p_T orthogonal to the direction of its parent parton:

$$j_{Ty} \equiv p_T \sin(\phi - \phi_q) \quad (2.3)$$

where ϕ is the azimuthal angle of the fragment and ϕ_q of the parton. Since z describes the longitudinal component of the fragmentation and j_{Ty} the orthogonal one,

$$p_T^2 = j_{Ty}^2 + z^2 p_{Tq}^2 \quad (2.4)$$

Parton Transverse Momentum k_{Ty} (1-D component) is the component of parton's momentum orthogonal on its propagation direction; it has a random orientation (zero mean) and produces the axis acoplanarity and energy imbalance of the dijets (jets originating from the same hard scattering process). As mentioned in the first chapter, there are three components to k_{Ty} : vacuum (VAC) (with its own two subcomponents - confinement and NLO), initial state (IS) (generated by the Cronin effect), and final state (FS) (generated by interaction with the QGP via gluon radiation). By measuring it in various collision types, we can extract all these components:

$$\langle |k_{Ty}| \rangle^{(pp)} \equiv \langle |k_{Ty}| \rangle_{VAC} \quad (2.5)$$

$$\langle |k_{Ty}| \rangle^{(pA)} \equiv \langle |k_{Ty}| \rangle_{VAC} \oplus \langle |k_{Ty}| \rangle_{IS} \quad (2.6)$$

$$\langle |k_{Ty}| \rangle^{(AA)} \equiv \langle |k_{Ty}| \rangle_{VAC} \oplus \langle |k_{Ty}| \rangle_{IS} \oplus \langle |k_{Ty}| \rangle_{FS} \quad (2.7)$$

Hadron Momentum out of Trigger Plane p_{out} is the momentum component of the associated hadron out of the plane formed by the trigger hadron momentum and the beam axis. It is depicted by the thick black arrow in Figure (2.1) and depends on both j_{Ty} and k_{Ty} .

Throughout this work we will use the *Gaussian approximation* for the jet azimuthal profile with the understanding that it underpredicts the real distribution at large relative azimuthal angles. We will test this approximation in the case of jets in pp collisions.

If $G(x, y)$ is a symmetric ($\sigma_x = \sigma_y$) 2-D Gaussian, the following equations between the 2D rms, 1D rms and mean of 1D absolute coordinate hold:

$$\sqrt{\langle r^2 \rangle} = \sqrt{2} \sqrt{\langle x^2 \rangle} = \sqrt{\pi} \langle |x| \rangle \quad (2.8)$$

where $r \equiv \sqrt{x^2 + y^2}$. Note that mean of 1D coordinate is null $\langle x \rangle \equiv 0$. All processes that induce a k_T kick on the parton have a random orientation in

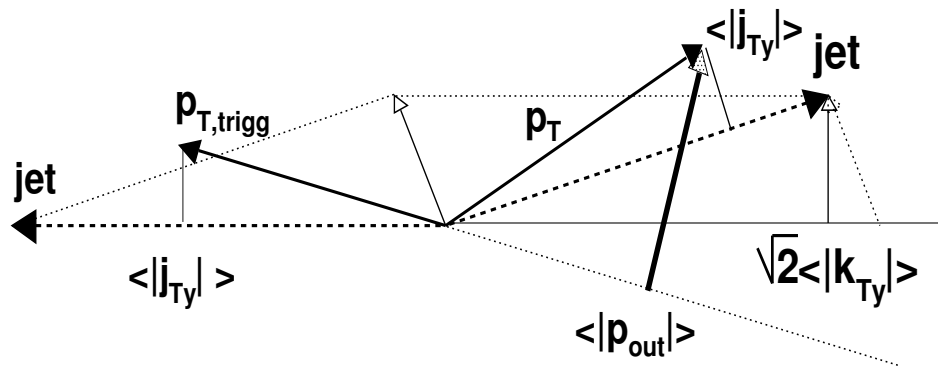


Figure 2.1 Topology of a dijet event (see text)

the plane orthogonal to the parton's propagation direction, hence k_{Tx} and k_{Ty} have symmetric distributions. The same is true for j_T .

A large fraction of this chapter deals with the relationship between the jet parameters and the parameters of the two-hadron azimuthal correlation of a jet source. The typical shape of such a correlation function, as can be seen in Fig.(C.1), comprises a near-angle gaussian (centered at $|\Delta\phi| = 0$) described by its **width** σ_N **and area** S_N and an away-angle gaussian (centered at $|\Delta\phi| = \pi$) also described by its **width** σ_A **and area** S_A . Note that two-hadron correlation functions in heavy ion collisions have another component - *collective flow* - that will be dealt with separately in Section 2.4.

Finally, two-hadron correlation functions can be mapped out as a function of both hadrons' momenta. We will refer to correlations of hadrons with momenta in the same interval ($\langle p_{Ttrigg} \rangle = \langle p_T \rangle$) as fixed (or symmetric) correlation functions, and to correlations of hadrons with momenta in different intervals ($\langle p_{Ttrigg} \rangle \neq \langle p_T \rangle$) as assorted (or asymmetric) correlation functions. In the later, it is usual to fix the trigger hadron and scan the p_T of the associated hadron.

2.2 Derivation of the Equations for Jet Shape Parameters

2.2.1 Extraction of $\langle |j_{Ty}| \rangle$

From Eq.(2.3), we can write:

$$\langle |j_{Ty}| \rangle \approx \langle p_T \rangle \sin \langle |\phi - \phi_{jet}| \rangle \quad (2.9)$$

where we neglected the covariance between hadron's momentum and azimuthal angle. This is known to break at low p_T (comparable to j_T) due to the *Seagull effect* which truncates the large relative azimuthal angles (see Appendix B).

The standard deviation of two-particle relative azimuthal distribution coming from the fragmentation of a parton is

$$\begin{aligned} \sigma_N^2 &\equiv \langle (\phi_1 - \phi_2)^2 \rangle = \langle ((\phi_1 - \phi_{jet}) - (\phi_2 - \phi_{jet}))^2 \rangle \\ &= \langle (\phi_1 - \phi_{jet})^2 \rangle + \langle (\phi_2 - \phi_{jet})^2 \rangle \\ &= \frac{\pi}{2} \left(\langle |\phi_1 - \phi_{jet}| \rangle^2 + \langle |\phi_2 - \phi_{jet}| \rangle^2 \right) \end{aligned} \quad (2.10)$$

where we used Eq.(2.8) and assumed statistical independent production of the two fragments ($\langle (\phi_1 - \phi_{jet})(\phi_2 - \phi_{jet}) \rangle \equiv 0$). In the case of symmetric (fixed) correlations, the two fragments have the same azimuthal distributions and

$$\sigma_N = \sqrt{\pi} \langle |\phi - \phi_{jet}| \rangle \quad (2.11)$$

so, the formula for symmetric (fixed) correlations is:

$$\langle |j_{Ty}| \rangle = \langle p_T \rangle \sin \frac{\sigma_N}{\sqrt{\pi}} \quad (2.12)$$

For asymmetric (assorted) correlations the angular dispersion is

$$\sigma_N = \sqrt{\frac{\pi}{2}} \sqrt{\arcsin^2 \frac{\langle |j_{Ty}| \rangle}{\langle p_{T1} \rangle} + \arcsin^2 \frac{\langle |j_{Ty}| \rangle}{\langle p_{T2} \rangle}} \quad (2.13)$$

where we used the scaling property of j_T . By inverting (2.13) and assuming that $\arcsin(arg) \approx arg$ (the small angle, or high p_T , approximation) one can extract

$$\langle |j_{Ty}| \rangle \approx \sqrt{\frac{2}{\pi}} \sigma_N \frac{\langle p_{T1} \rangle \langle p_{T2} \rangle}{\sqrt{\langle p_{T1} \rangle^2 + \langle p_{T2} \rangle^2}} \quad (2.14)$$

Notes:

- The scaling of j_T with p_T can also be tested using assorted correlations: fixed correlations are employed in a given "reference" p_T bin to measure its $\langle |j_{Ty}| \rangle$ using Eq.(2.12), then assorted correlations are employed with one hadron kept fixed in this reference bin and the other hadron scanning the entire p_T spectrum; this way, in Eq.(2.13), one $\langle |j_{Ty}| \rangle$ is known and fixed allowing the extraction of the other one without any scaling assumption.
- j_T scaling, in view of Eq.(2.12), tells us that the lower the p_T of a fragment, the broader its emission angle, such that $p_T \cdot \Delta\phi \approx const$; there is however an upper cutoff due to the Seagull effect (see Appendix B).

2.2.2 $\langle |p_{out}| \rangle$ Formula and Extraction of $\langle |k_{Ty}| \rangle$

In this section we will derive an equation for $\langle |p_{out}| \rangle$ similar with Eq.(1.6) obtained by Feynman, Field and Fox [30] and used in the CCOR experiment [5], but taking into account some factors explicitly neglected in [30].

Let us first examine the case of two hadrons from the fragmentation of two hard-scattered partons with zero fragmentation transverse momentum $\langle |j_{Ty}| \rangle$ as shown in Fig.(2.2).

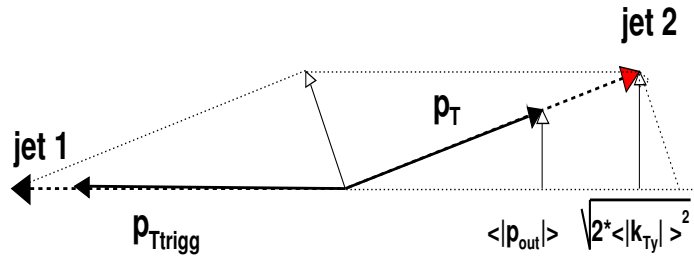


Figure 2.2 Topology of a dijet event with $j_T \equiv 0$ for both the trigger and the associated hadrons.

From Eq.(2.2) and Fig.(2.2) the $\langle |p_{out}| \rangle$ formula reads:

$$\langle |p_{out}| \rangle^2 = 2x_E^2 \langle k_{Ty} \rangle^2 \frac{\langle z_{trigg} \rangle^2}{1 - 2\langle k_{Ty} \rangle^2 \langle z_{trigg} \rangle^2 / \langle p_{Ttrigg} \rangle^2} \quad (2.15)$$

A comparison with Eq.(1.6) shows that the fraction in the right hand side is neglected. A much simpler formula can be obtained however if the x_E variable is replaced by

$$x_h \equiv \frac{\langle p_T \rangle}{\langle p_{Ttrigg} \rangle} \quad (2.16)$$

Then the formula for $\langle |p_{out}| \rangle$ can be written as

$$\langle |p_{out}| \rangle^2 = 2x_h^2 \langle z_{trigg} \rangle^2 \langle |k_{Ty}| \rangle^2 \quad (2.17)$$

where we used the fact that $\langle |p_{Tjet1}| \rangle = \langle |p_{Tjet2}| \rangle$. Note that this is true **only** on average (k_T smearing also produces parton momentum imbalance in each event; still, due to its random angular distribution, it does not change the mean of the parton momentum distribution).

Let us examine the case when the $\langle |j_{Ty}| \rangle > 0$ for trigger particle and $\langle |j_{Ty}| \rangle = 0$ for associated particle as in Fig.(2.3). The magnitude of x_1 corresponds to

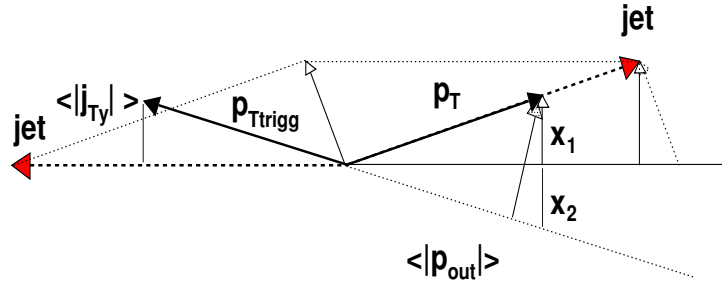


Figure 2.3 Topology of a dijet event with $j_T \neq 0$ only for the trigger hadron.

$\langle |p_{out}| \rangle$ from Fig. 2.2. The $\langle |j_{Ty}| \rangle$ kick on the trigger particle generates an additional component x_2 . The $\langle |p_{out}| \rangle$ value can be obtained from the orthogonal projection of $x_1 \oplus x_2$ to \vec{p}_{Ttrigg} . One can see that

$$\frac{x_2^2}{\langle p_T \rangle^2 - x_1^2} = \frac{\langle |j_{Ty}| \rangle^2}{\langle p_{Ttrigg} \rangle^2 - \langle |j_{Ty}| \rangle^2} \quad (2.18)$$

and

$$\langle |p_{out}| \rangle^2 = (x_1^2 + x_2^2) \frac{\langle p_{Ttrigg} \rangle^2 - \langle |j_{Ty}| \rangle^2}{\langle p_{Ttrigg} \rangle^2} = 2x_h^2 \langle z_{trigg} \rangle^2 \langle |k_{Ty}| \rangle^2 + x_h^2 \langle |j_{Ty}| \rangle^2 \quad (2.19)$$

An approximation, used in the first equality, is that we neglected the term $x_1 \cdot x_2$ because its statistical mean corresponds to the correlation between the acoplanarity vector ($x_1 = \langle |p_{out}| \rangle$) and the transverse fragmentation vector ($x_2 \sim \langle |j_{Ty}| \rangle$), which we suppose independent. Another approximation, used in the second equality, is that $2\langle |j_{Ty}| \rangle^2 \ll \langle p_{Ttrigg} \rangle^2$, which is always the case in our analysis.

In the final step the $\langle |j_{Ty}| \rangle > 0$ of the associated particle is taken into account (see Fig. 2.4). Here x_3 (the $\langle |p_{out}| \rangle^2$ value from (2.19)) gets additional

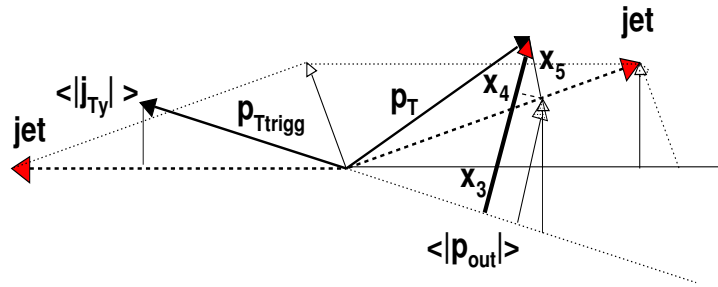


Figure 2.4 Topology of a dijet event with $j_T \neq 0$ for the both hadrons.

component x_4 which correspond to the projection of $\langle |j_{Ty}| \rangle > 0$ from the associated particle to the \vec{p}_{out} direction.

If we neglect the acoplanarity between \vec{x}_5 and \vec{p}_{out} , then we get the final formula for $\langle |p_{out}| \rangle$:

$$\langle |p_{out}| \rangle^2 = 2x_h^2 \langle z \rangle_{trigg}^2 \langle |k_{Ty}| \rangle^2 + (1 + x_h^2) \langle |j_{Ty}| \rangle^2 \quad (2.20)$$

Compared to Eq.(1.6), there are two differences: $\langle |k_{Ty}| \rangle$ gets multiplied by $\langle z_{trigg} \rangle$ and x_E is replaced by x_h .

If $\Delta\phi$ is the relative azimuthal angle between the trigger hadron and an

associated hadron from the opposite jet of the dijet, then

$$\langle |p_{out}| \rangle = -\langle p_T \rangle \sin \langle |\Delta\phi| \rangle = -\langle p_T \rangle \sin \sqrt{\frac{2}{\pi}} \sigma_A \quad (2.21)$$

where σ_A is the width of the away side Gaussian. The final equation for $\langle |k_{Ty}| \rangle$ is:

$$\langle |k_{Ty}| \rangle = \frac{1}{\sqrt{2}x_h \langle z_{trigg} \rangle} \sqrt{\langle p_T \rangle^2 \sin^2 \sqrt{\frac{2}{\pi}} \sigma_A - (1 + x_h^2) \langle |j_{Ty}| \rangle^2} \quad (2.22)$$

Note that $\langle |k_{Ty}| \rangle$ depends not only on σ_A and σ_N (through $\langle |j_{Ty}| \rangle$), but also on $\langle z_{trigg} \rangle$, a quantity which has to be calculated from the fragmentation function. Also, the $\langle |k_{Ty}| \rangle$ formula for fixed (symmetric) correlations is easily obtained from Eq.(2.22) by setting $x_h \equiv 1$.

Note also that in the small angle approximation ($\sin x \approx x$), by using Eq.(2.14) we get the usual formula:

$$\langle |k_{Ty}| \rangle \approx \frac{1}{\sqrt{\pi} \langle z_{trigg} \rangle} \langle p_{Ttrigg} \rangle \sqrt{\sigma_A^2 - \sigma_N^2} \quad (2.23)$$

or,

$$\sqrt{\langle k_T^2 \rangle} \approx \langle p_{Tjet} \rangle \sqrt{\sigma_A^2 - \sigma_N^2} \quad (2.24)$$

Finally, it was J. Rak who first realized the missing $\langle z_{trigg} \rangle$ factor in Feynman, Field and Fox formula Eq.(1.6). We point out here that all the previous measurements of $\sqrt{\langle k_T^2 \rangle}$ based on two hadron correlations (like the CCOR measurements [5]) contain this factor and should be corrected for it.

2.3 Jet Conditional Yields. Jet Fragmentation Function.

The probability that a certain event B occurs given that another event A has occurred is called a *conditional probability* $P(B|A)$ and is given by

$$P(B|A) = \frac{P(A \cap B)}{P(A)} \quad (2.25)$$

where $P(A \cap B)$ is the probability of both A and B occurring, and $P(A)$ is the probability of A occurring without reference to B.

In two-particle correlation analysis, we define in the same way the **near/away conditional yields** as the number of associated hadrons in the near/away

region per trigger hadron:

$$n_{N,A} \equiv \frac{N_{N,A}^{pairs}}{N_{trigg}} = \frac{1}{N_{trigg}} \frac{S_{N,A}}{S} N^{pairs} \quad (2.26)$$

where $N_{N,A}^{pairs}$ are the number of pairs in the near/away region, and N^{pairs} is the total number of pairs entering in the correlation function. In Section 4.2 we will define the correlation function such that the ratio of the near/away Gaussian areas $S_{N,A}$ and its total area S will be equal to the ratio of the number of pairs in these regions.

The z distribution of hadrons from parton fragmentation is called the **parton fragmentation function**. It has been introduced in Section 1.2 and we also mentioned that x_E is used instead of z in many experiments. We extract it by measuring the $\langle x_E \rangle$ dependence of the away conditional yield n_A in assorted correlations with the trigger hadron fixed at some high p_T and scanning with the associated hadron lower p_T values. The trigger approximates well the transverse momentum and direction of the parton, hence the distribution of the number of associated hadrons in x_E will give the fragmentation function. Note that doing this with the near conditional yield n_N imposes a trigger bias on the fragmentation function. Also note that applying this procedure in heavy ion collisions for various centralities measures the modification of the parton fragmentation function in QCD media.

The inverse slope of an exponential fit of the fragmentation function measured as described above is equal to $\langle x_E \rangle$. The rest of this section presents an iterative method for the extraction of $\langle z \rangle$ from $\langle x_E \rangle$ and the measured π^0 spectra.

The high- p_T hadron spectrum from parton fragmentation can be written as a convolution of the fragmentation function $D(z)$ and final state parton spectrum $f_q(p_{Tq})$:

$$\frac{d\sigma}{p_T dp_T} = \int_{x_T}^1 D(z) f_q\left(\frac{p_T}{z}\right) \frac{dz}{z^2} \quad (2.27)$$

where $x_T \equiv 2p_T/\sqrt{s_{NN}}$.

Due to the universality and Q^2 -independence of the fragmentation function, one can use the form found in previous experiments: $D(z) \approx e^{-6z}$. For the hadronic p_T spectrum we use a fit to the data, like the Hagedorn

parametrization. Then, we assume that the partonic p_T spectrum $f_q(p_{Tq})$ has the same form (parametrization) and vary its parameters under the constraint given by Eq.(2.27) until the hadronic spectrum is recovered. This way we extract $f_q(p_{Tq})$.

Note that for $p_T > 3\text{GeV}/c$, when the hadronic spectrum becomes power law $1/p_T d\sigma/dp_T = C/(p_0 + p_T)^n$, the partonic spectrum is also power law with a power index $n - 2$.

Since

$$\langle z \rangle = \frac{\int_{x_T}^1 z D(z) f_q(p_T/z) z^{-2} dz}{\int_{x_T}^1 D(z) f_q(p_T/z) z^{-2} dz} \quad (2.28)$$

using the relationship $\langle x_E \rangle \langle z_{trigg} \rangle = \langle z \rangle$, we get

$$\langle x_E \rangle \cdot \frac{\int_{x_{Ttrigg}}^1 z e^{-z/\langle z \rangle} f_q(p_T/z) z^{-2} dz}{\int_{x_{Ttrigg}}^1 e^{-z/\langle z \rangle} f_q(p_T/z) z^{-2} dz} = \langle z \rangle \quad (2.29)$$

We finally solve Eq.(2.29) numerically for $\langle z \rangle$ for each trigger momentum p_{Ttrigg} .

Note that we can use the "inclusive" $\langle z \rangle$ extracted as above to correct only the $\langle z \rangle \langle |k_{Ty}| \rangle$ from fixed (symmetric) correlation functions. In assorted (asymmetric) correlation functions, the different kinematical restrictions imposed on the trigger-hadron pair generate a "conditional" fragmentation function with a different $\langle z \rangle$. Appendix A presents in detail this issue.

2.4 Collective Quadrupole Azimuthal Correlations.

The previous sections of this chapter dealt in detail with the various parameters of the correlation functions generated by jets.

As mentioned already, in heavy ion collisions, there is another source of two-hadron azimuthal correlations: **collective flow**. The spatial azimuthal anisotropy in the initial state (the "almond" shape of the interaction region) is transformed by the dynamics of the interaction into momentum anisotropy in the final state. This is due to the long range, collective correlations present in the bulk QCD matter formed in such collisions. The azimuthal distribution of the hadrons formed can be described by a Fourier decomposition around the *reaction plane direction* Φ_{RP} (the projection of the impact parameter \vec{b} in

the transversal plane):

$$\frac{dN}{d\phi} = \frac{n}{2\pi} [1 + v_1 \cos(\phi - \Phi_{RP}) + 2v_2 \cos(2(\phi - \Phi_{RP}))] \quad (2.30)$$

where n is the total number of hadrons. The terms of order $n > 3$ of the expansion have been neglected. The expansion coefficients are: *directed flow coefficient* v_1 and *elliptic flow coefficient* v_2 . In the particular case of mid-rapidity collisions at RHIC, directed flow is negligible compared to elliptic flow ($v_1(\eta \approx 0) \approx 0$) [26] so

$$\frac{dN}{d\phi} (\eta \approx 0) \approx \frac{n}{2\pi} [1 + 2v_2 \cos(2(\phi - \Phi_{RP}))] \quad (2.31)$$

The pair relative azimuthal distribution can be obtained from Eq.(2.31) by convoluting it with itself:

$$\frac{d^2 N_{12}}{d\phi_1 d\phi_2} = \int \frac{d\Phi_{RP}}{2\pi} \frac{dN_1}{d\phi_1} \frac{dN_2}{d\phi_2} = \frac{n_1 n_2}{(2\pi)^2} [1 + 2v_2^{(1)} v_2^{(2)} \cos(2(\phi_1 - \phi_2))] \quad (2.32)$$

So the typical elliptic flow correlation function will have a $\cos(2\Delta\phi)$ shape.

The measured elliptic flow coefficient v_2 at RHIC [17] agrees very well with hydrodynamical calculations in the low p_T ($< 2\text{GeV}/c$) region. In the high p_T region ($> 2\text{GeV}/c$), v_2 is approximately independent of p_T deviating systematically from any hydrodynamical model. This is why the historical name of collective "flow" coefficient for v_2 is misleading in the context of high p_T correlations and we will refer to it from now on as the collective "**quadrupole**" coefficient.

2.5 Correlation Function with a Jet Source and a Collective Quadrupole Source

In the previous section we argued that azimuthal correlations in heavy ion collisions have two sources - dijets and collective. The overall azimuthal correlation function with multiple sources is not a linear superposition of individual correlation functions from each source - potentially, large components arise from the **interference** of these sources.

In this section, we will develop a model for the correlation function with a

dijet source and a collective quadrupole source.

In order to describe the azimuthal distribution of hadrons from a jet source, the correlation between the jet emission angle Φ_{Jet} and the reaction plane of the collision Φ_{RP} is introduced by modulating the angular fragmentation function $G(\phi - \Phi_{Jet})$ (which we will suppose normalized to unity) with their difference:

$$\frac{dN}{d\phi}(\Phi_{RP}, \Phi_{Jet}) = nG(\phi - \Phi_{Jet})[1 + 2j_2 \cos(2(\phi_{Jet} - \Phi_{RP}))] \quad (2.33)$$

where j_2 is the *average* effective quadrupole strength of this correlation. Since the jet emission in the transverse plane is random, we can integrate over Φ_{Jet} :

$$\frac{dN}{d\phi}(\Phi_{RP}) = \frac{n}{2\pi}[1 + 2j_2 \cdot g_2 \cos(2(\phi - \Phi_{RP}))] \quad (2.34)$$

where

$$g_2 \equiv \int G(x) \cos(2x) dx \quad (2.35)$$

is the second cosine Fourier moment of function G .

From Eq.(2.31) and Eq.(2.34) we get the following azimuthal hadron distribution:

$$\frac{dN}{d\phi}(\Phi_{RP}) = \frac{n}{2\pi}[1 + 2V_2 \cos(2(\phi - \Phi_{RP}))] \quad (2.36)$$

where

$$V_2 \equiv \frac{n^{(flow)}}{n} v_2 + \frac{n^{(jet)}}{n} j_2 g_2 \quad (2.37)$$

$n^{(flow)}$ being the total number of hadrons from the collective source and $n^{(jet)}$ the total number of hadrons from the jet source, $n^{(flow)} + n^{(jet)} = n$.

Having the forms of the single hadron azimuthal distributions from both sources - Eq.(2.31) for the collective source and Eq.(2.34) for the jet source - we can obtain the hadron pair relative azimuthal distributions by convolution

$$\frac{d^2 N_{12}}{d\phi_1 d\phi_2} = \frac{1}{2\pi} \int d\Phi_{RP} \frac{dN_1}{d\phi_1}(\Phi_{RP}) \cdot \frac{dN_2}{d\phi_2}(\Phi_{RP}) \quad (2.38)$$

and, from it, the relative azimuthal angle correlation function (normalized to

unity):

$$C(\Delta\phi) \equiv \frac{2\pi}{n_1 n_2} \int_0^{2\pi} d\phi_1 \int_0^{2\pi} d\phi_2 \delta(\Delta\phi - (\phi_1 - \phi_2)) \frac{d^2 N_{12}}{d\phi_1 d\phi_2} \quad (2.39)$$

Both hadrons from collective source - corresponds to the convolution of Eq.(2.31) with itself and gives:

$$C_{cc}\Delta\phi) = \frac{n_1^{(flow)} n_2^{(flow)}}{n_1 n_2} [1 + 2v_2^{(1)} v_2^{(2)} \cos(2\Delta\phi)] \quad (2.40)$$

One hadron from collective source, the other from jet source - corresponds to the convolution of Eqs.(2.31) and (2.34) and gives

$$C_{cj}(\Delta\phi) = \frac{n_1^{(flow)} n_2^{(jet)}}{n_1 n_2} [1 + 2v_2^{(1)} j_2^{(2)} g_2^{(2)} \cos(2\Delta\phi)] \quad (2.41)$$

Both hadrons from two different jets - corresponds to the convolution of Eq.(2.34) with itself and gives:

$$C_{j_1 j_2}(\Delta\phi) = \frac{n_1^{(jet)} n_2^{(jet)}}{n_1 n_2} [1 + 2j_2^{(1)} g_2^{(1)} j_2^{(2)} g_2^{(2)} \cos(2\Delta\phi)] \quad (2.42)$$

Both hadrons from the same jet (a monojet) - corresponds to the convolution of the angular fragmentation function $G(\phi - \Phi_{Jet})$ with itself, if we assume *independent fragmentation*, and gives:

$$C_{monojet}(\Delta\phi) = \frac{2\pi n_{12}^{(monojet)}}{n_1 n_2} G(\Delta\phi) \quad (2.43)$$

where $G(\Delta\phi) \equiv \int d\Phi_{Jet} G(\phi_1 - \Phi_{Jet}) G(\phi_2 - \Phi_{Jet})$ is a Gaussian like the single azimuthal distribution $G(\phi - \Phi_{Jet})$, but with a width larger by $\sqrt{2}$ ($\sigma_{2part} = \sqrt{2} \sigma_{1part}$).

Both hadrons from two back-to-back jets (a dijet) - corresponds to the convolution of Eq.(2.33) for a jet with direction Φ_{Jet} with the same form for a back-to-back jet with the direction

$$\Phi'_{Jet} = \Phi_{Jet} - \Psi - \pi \quad (2.44)$$

where Ψ is the dijet acoplanarity. If we denote by $D_{12}(\Psi) \equiv dn_{12}/d\Psi$ the

hadron pair acoplanarity distribution, we have:

$$\begin{aligned} \frac{d^2 N_{12}}{d\phi_1 d\phi_2} &= \int d\Psi D_{12}(\Psi) \int \frac{d\Phi_{RP}}{2\pi} \int \frac{d\Phi_{Jet}}{2\pi} \cdot \eta n_{12}^{(dijet)} \\ &\quad G(\phi_1 - \Phi_{Jet}) [1 + 2j_2^{(1)} \cos(2(\Phi_{Jet} - \Phi_{RP}))] \\ &\quad G(\phi_2 - \Phi'_{Jet}) [1 + 2j_2^{(2)} \cos(2(\Phi'_{Jet} - \Phi_{RP}))] \end{aligned} \quad (2.45)$$

where η is a normalization constant and Ψ , Φ_{Jet} , and Φ'_{Jet} are related through Eq.(2.44). The integrals over Φ_{RP} and Φ_{Jet} are:

$$\begin{aligned} &\int d\Phi_{RP} [1 + 2j_2^{(1)} \cos(2(\Phi_{Jet} - \Phi_{RP}))] [1 + 2j_2^{(2)} \cos(2(\Phi'_{Jet} - \Phi_{RP}))] \\ &= 2\pi [1 + 2j_2^{(1)} j_2^{(2)} \cos(2\Psi)] \end{aligned} \quad (2.46)$$

$$\int d\Phi_{Jet} G(\phi_1 - \Phi_{Jet}) G(\phi_2 + \Psi + \pi - \Phi_{Jet}) = G(\Delta\phi - (\Psi + \pi)) \quad (2.47)$$

where $G(\Delta\phi)$ is again a 2-dimensional Gaussian, so it has the width larger by $\sqrt{2}$ compared to the 1-dimensional Gaussian $G(\phi - \Phi_{Jet})$. By replacing these integrals in Eq.(2.45), we get:

$$\frac{d^2 N_{12}}{d\phi_1 d\phi_2} = \frac{n_{12}^{(dijet)}}{2\pi} \int d\Psi E(\Psi) G(\Delta\phi - (\Psi + \pi)) \quad (2.48)$$

where we defined:

$$E(\Psi) \equiv \eta D_{12}(\Psi) [1 + 2j_2^{(1)} j_2^{(2)} \cos(2\Psi)] \quad (2.49)$$

and the normalization constant η is chosen such that $\int d\Psi E(\Psi) \equiv 1$. Finally, from Eq.(2.48) and Eq.(2.39), we get the correlation function for this last type of hadron pairs:

$$C_{dijet}(\Delta\phi) = \frac{2\pi n_{12}^{(dijet)}}{n_1 n_2} (E \circ G)(\Delta\phi - \pi) \quad (2.50)$$

where by $E \circ G$ we denoted the convolution with respect to the dijet acoplanarity angle Ψ of the angular fragmentation function $G(\Delta\phi)$ and the acoplanarity function $E(\Psi)$.

The treatment presented here for the correlation of hadron pairs from dijets (back-to-back jets) was developed by P. Stankus [20].

We are ready to add up the contributions from all pair types described above to the azimuthal correlation function:

$$\begin{aligned}
C(\Delta\phi) = & \frac{n_1^{(flow)} n_2^{(flow)}}{n_1 n_2} [1 + 2v_2^{(1)} v_2^{(2)} \cos(2\Delta\phi)] \\
& + \frac{n_1^{(flow)} n_2^{(jet)}}{n_1 n_2} [1 + 2v_2^{(1)} j_2^{(2)} g_2^{(2)} \cos(2\Delta\phi)] \\
& + \frac{n_1^{(jet)} n_2^{(flow)}}{n_1 n_2} [1 + 2v_2^{(2)} j_2^{(1)} g_2^{(1)} \cos(2\Delta\phi)] \\
& + \frac{n_1^{(jet)} n_2^{(jet)}}{n_1 n_2} [1 + 2j_2^{(1)} g_2^{(1)} j_2^{(2)} g_2^{(2)} \cos(2\Delta\phi)] \\
& + \frac{2\pi n_{12}^{(monojet)}}{n_1 n_2} G(\Delta\phi) \\
& + \frac{2\pi n_{12}^{(dijet)}}{n_1 n_2} (E \circ G)(\Delta\phi - \pi)
\end{aligned} \tag{2.51}$$

After some regrouping of terms and using the simple identities $n_i = n_i^{(flow)} + n_i^{(jet)}$ ($i = 1, 2$), we get the final formula:

$$\begin{aligned}
C(\Delta\phi) = & 1 + 2V_2^{(1)} V_2^{(2)} \cos(2\Delta\phi) \\
& + \frac{2\pi n_{12}^{(monojet)}}{n_1 n_2} G(\Delta\phi) + \frac{2\pi n_{12}^{(dijet)}}{n_1 n_2} (E \circ G)(\Delta\phi - \pi)
\end{aligned} \tag{2.52}$$

where V_2 is defined in Eq.(2.37) and $E(\Psi)$ is defined in Eq.(2.49).

Comments:

- The correlation between the reaction plane Φ_{RP} and jet axis Φ_{Jet} , as introduced in this model by Eq.(2.33), has the net effect of an increase in the magnitude of the collective quadrupole coefficient.
- The effect of the dijet acoplanarity Ψ on the away two hadron correlation consists of a change (broadening) of its Gaussian shape. The underlying physics for the acoplanarity Ψ in this model is the k_T acquired by the parton in the initial and/or the final state.
- In a constant area normalization of the correlation function ($S \equiv \int d\Delta\phi C(\Delta\phi) \equiv 2\pi$), Eq.(2.52) implies that the ratio between the near/away Gaussian areas is

$$\frac{S_{N,A}}{S} = \frac{n_{12}^{N,A}}{n_1 n_2} \tag{2.53}$$

which is equivalent to Eq.(2.26) for conditional yields.

2.6 Other Sources of Azimuthal Correlations

In this chapter, we presented the main two sources of physical azimuthal correlations: *dijets*, described by one Gaussian in the "near" relative angle region ($|\Delta\phi| \approx 0$) and one Gaussian in the "away" relative angle region ($|\Delta\phi| \approx \pi$), and *collective* correlations (predominantly quadrupole at $\eta \approx 0$), described by a cosine modulation of n times the relative angle of amplitude v_n ($n= 2$ for quadrupole). However, other types of azimuthal correlations are present and we will list them below. They are usually regarded as background and eliminated via various methods.

Resonance Decay Correlations Resonance decays, like $\rho \rightarrow \pi^+ + \pi^-$, $K_0^S \rightarrow \pi^+ + \pi^-$, and $\Lambda \rightarrow K^- + p$, generate near angle correlations. If these decays happen within $1 - 1.5m$ from the collision vertex (the radial size of the magnetic field in the PHENIX spectrometer is $2m$), the products will be bent strongly by the magnetic field since the average p_T of the daughters is quite low (of the order $0.5 - 0.8 GeV/c$). However, depending on the decay length of these resonances, there could be a small fraction of decay products that see only a small magnetic region of the spectrometer; they will therefore be mistakenly reconstructed as high momentum hadrons. This is an important background in the near relative angle region ($\Delta\phi \approx 0$) of azimuthal correlations functions of charged hadrons at low and moderate p_T ($< 2 GeV/c$).

Nonetheless, we can reliably estimate its effects. The width of this correlation depends only on the kinematics of the decay (particle masses and momenta) which is known; the overall effect turns out to be a narrowing of the near angle gaussian. Moreover, correlations from jet fragmentation has little charge dependence, while resonance decay correlations produce only opposite charge hadrons. Considering these two facts, a significant difference between the width of the near angle correlation of same charge hadrons and that of opposite charge hadrons is a good indication of resonance decay contamination.

Conversion Electrons Correlations Photons from π^0 decays are produced

copiously over a broad p_T region. They interact with the detector material and convert to electron pairs ($\gamma \rightarrow e^+e^-$). This results in a kind of background very similar with the one produced by resonance decays: contamination of near angle charged hadron correlation function.

It is more abundant than the first type simply because there are many more π^0 s than ρ s, K_0^S s, or Λ s, but also because there are dense components of the detector outside the magnetic field where conversions take place producing fake high momentum tracks as described above. Most notably, in the PHENIX detector, the entrance metallic frame of the drift chamber is the most important source of this kind of background.

Apart from the usual estimation method (charge dependence of near relative angle width), in this case we have a powerful rejection method: charged tracks that leave any signal (fire a photomultiplier tube) in the Ring Imaging Cherenkov (RICH) detector are discarded. The RICH is a very efficient detector, specially built for electron identification in PHENIX, which is actually used in this analysis to veto them.

Momentum Conservation Correlations Overall momentum conservation for the entire event was proven [39] to generate a v_1 like collective correlation. Soft hadron production has an exponential spectrum that dominates at low- p_T ; however, when a high- p_T hadron (in the tail of the exponential) is produced in a collision, its momentum is balanced by an excess in the production of low- p_T hadrons in the opposite side. The two hadron correlation induced by momentum conservation has the typical form:

$$C = -\frac{2\vec{p}_{T1} \cdot \vec{p}_{T2}}{n_{all} \langle p_T^2 \rangle_{all}} \quad (2.54)$$

and the relative azimuthal angle distribution of hadron pairs is given by

$$\frac{d^2 N_{12}}{d\phi_1 d\phi_2} \approx -\frac{1}{\pi} \frac{n_{meas} p_T^{(jet)} \langle p_T \rangle_{meas}}{n_{all} \langle p_T^2 \rangle_{all}} \cdot \cos(\Delta\phi) \quad (2.55)$$

Note that this type of collective correlation is significant only if the trigger hadron is at high- p_T and the associated hadron at low- p_T (generally, below 1GeV/c); n_{meas} (the multiplicity in the associated p_T bin) decreases exponentially with p_T , while n_{all} (the integrated multiplicity over the entire event) is a constant. Note also that it does not happen if

the high- p_T trigger hadron comes from jet fragmentation since this jet is already balanced in momentum by its back-to-back partner jet.

Residual (Multiplicity Fluctuation) Correlations There is a trivial type of residual correlation that arise from centrality selection [20], due to multiplicity fluctuation within a given fixed centrality interval. Suppose that spectra in AA collisions are independent of N_{part} (which is proportional to the multiplicity). Then,

$$\frac{d^3 N}{dp^3}(N_{part}) = a N_{part} F(\vec{p}) \quad (2.56)$$

$$\frac{d^6 N_{12}}{dp_1^3 dp_2^3}(N_{part}) = ab N_{part}^2 F(\vec{p}_1) F(\vec{p}_2) \quad (2.57)$$

where $F(\vec{p})$ is the normalized spectral shape. If $P(N_{part})$ is the normalized probability distribution of the number of participants, we can build its correlation function:

$$\begin{aligned} C(\vec{p}_1, \vec{p}_2) &= \frac{\sum_{N_{part}} P(N_{part}) d^6 N_{12} / dp_1^3 dp_2^3}{\sum_{N_{part}} P(N_{part}) d^3 N_1 / dp_1^3 \cdot \sum_{N_{part}} P(N_{part}) d^3 N_2 / dp_2^3} \\ &= \frac{\sum_{N_{part}} P(N_{part}) N_{part}^2}{\left(\sum_{N_{part}} P(N_{part}) N_{part}\right)^2} = 1 + \left(\frac{\sigma(N_{part})}{\langle N_{part} \rangle}\right)^2 \end{aligned} \quad (2.58)$$

so, the net effect is an increase of the overall flat background from uncorrelated pairs. The so-called subtraction methods (that calculate and subtract this background to obtain a $dN_{12}/d\Delta\phi$ distribution) must correct for this effect, especially when they use rather large centrality bins (as it can be seen from Eq.(2.58), this residual correlation goes away for very fine centrality binning).

Since the effect on a correlation function is only on the overall multiplicative constant, it can be eliminated through a particular choice of normalization that fixes it, like the constant area normalization used in our analysis (see Section 4.2.1).

Detector (Efficiency Fluctuation) Correlations The shape of two particle azimuthal correlations can be changed by fluctuations of detection efficiency. This type of detector induced deformations of the correlation

functions are corrected by using the event mixing method. See Section 4.2.2 for details.

CHAPTER 3. PHENIX Central Arm Detectors

3.1 Detector Overview

The PHENIX detector is formed by 11 subsystems grouped in four spectrometer arms and three global detectors. Fig.(3.1) shows a beam view and a side view of the detector.

Global Detectors are positioned around the beam pipe at the interaction point (the Multiplicity Vertex Detector - MVD) or at large rapidities (the Beam-Beam Counter - BBC and the Zero Degree Calorimeter - ZDC) and have full azimuthal coverage. They are used in measuring global quantities (vertex position, collision time, reaction plane orientation, centrality and multiplicity) and provide the minimum bias level-1 trigger.

Central Spectrometer Arms are positioned at mid-rapidity ($|\Delta\eta| < 0.35$) and each covers 90° in the azimuthal plane. They track (using the Drift Chambers - DC, Pad Chambers - PC and Time Expansion Chamber - TEC) and identify (using the Time Of Flight - TOF and the Ring Imaging Cherenkov - RICH detectors) charged hadrons and electrons. The outer layers are two electromagnetic calorimeters (the Lead Scintillator - PbSc and Lead Glass - PbGl calorimeters) used in photon and electron detection.

Forward Spectrometer Arms have the $1.15 < |\Delta\eta| < 2.25$ (*South*), 2.44 (*North*) rapidity coverage and full azimuthal coverage. They track (using the Muon Tracking Stations - MuTr) and identify (using the Muon Identifier Panels - MuID) muons.

The PHENIX convention for the coordinate system has the origin at the middle point between the BBCs, the z axis along the beam axis pointing towards the north muon arm, and the (x, y) plane in the transversal plane with the x axis pointing horizontally towards the west arm.

In the rest of this chapter, we will describe only the detectors used in this analysis and the way they are employed in extracting physical quantities.

For an extended description of the PHENIX subsystems, electronics, and online/offline analysis software, see the special NIM issue on RHIC and its detectors [23].

3.2 Global Detectors

The two **Beam-Beam Counters** (BBCs) are composed of 64 identical detector elements placed around the beam pipe (1cm away from it) at $3 \leq |\eta| \leq 3.9$ (1.4m from collision point) and have full azimuthal coverage. They measure charged hadrons emitted from the collision at large rapidity. The detector element is a Cherenkov counter consisting of a 3cm long, hexagonal shaped, Quartz radiator and a 1" diameter photomultiplier tube with 12 stage mesh dynodes. The BBCs are used to:

- measure the vertex position along the beam direction with a resolution of 0.6cm: $z_{vtx} = |T_1 - T_2|/2c$, where $T_{1,2}$ is the average time of charged particles counted in the North/South BBCs.
- give the start time for time-of-flight measurements with a resolution of about 40ps: $T_0 = (T_1 + T_2)/2$.
- reconstruct the reaction plane orientation in heavy ion collisions; because of the large rapidity position, non-collective effects are very small.
- measure the centrality of the collisions (together with the ZDC).
- provide the minimum bias (Level-1) trigger (see description later in this chapter).

The two **Zero Degree Calorimeters** (ZDCs) are small transverse area hadron calorimeters located downstream of the DX dipole magnets at about 18m from the interaction point. They measure the neutral energy (count the number of "spectator" neutrons) within a 2mrad cone about the beam direction (charged particles are swept away by the DX magnet). They are used to:

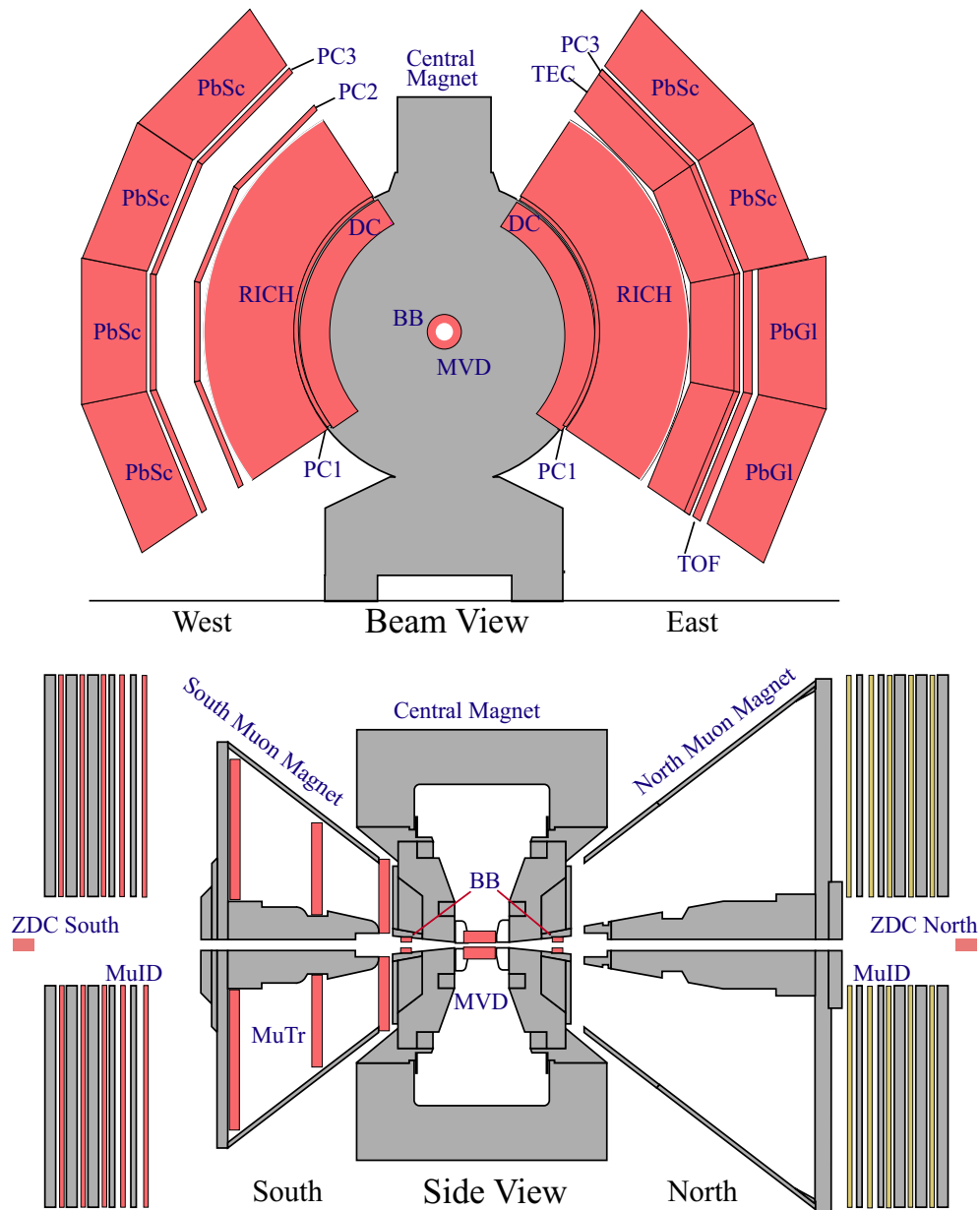


Figure 3.1 The PHENIX detector layout (Run-2 configuration): Upper panel - beam view of the central arms; Lower panel - side view of the muon arms

- measure the vertex position along the beam direction with a resolution of 3cm: $z_{vtx} = |T_1 - T_2|/2c$, where $T_{1,2}$ is the average time of neutrons counted in the North/South ZDCs.
- give the start time for time-of-flight measurements with a resolution of about 100ps: $T_0 = (T_1 + T_2)/2$.
- reconstruct the reaction plane orientation in heavy ion collisions; same rapidity argument as for BBCs; also, using spectators of the collision provides bias free measurement.
- measure the centrality of the collisions (together with the BBC).
- monitor the luminosity; during the Au-Au running the ZDC coincidence rate had an effective cross section of 10.4 barns (with an uncertainty of about 5%).
- provide the minimum bias (Level-1) trigger (see description below).

PHENIX **Level-1 Triggers** use online information from fast subsystems to select interesting events. The *Minimum Bias trigger* (MB) uses BBC and ZDC primitives to select events with $|z_{vtx}| < 30cm$, at least two PMTs hit in each BBC arm (North and South), and at least one neutron detected in each ZDC arm (North and South); the MB trigger efficiency with respect to inelastic *AuAu* collisions is $92 \pm 2\%$. In the central arms, the *ERT trigger* is used at Level-1 to enhance the fraction of events with high- p_T hadrons: it requests a lower threshold discrimination on sums of the analog signals from non-overlapping 2x2 groups of adjacent towers in the electromagnetic calorimeters, equivalent to an energy deposition of about 800MeV. Other Level-1 triggers were used in order to enhance the fraction of events with leptonic (electrons or muons) signals.

Centrality Determination is done in the offline analysis using the correlation between the BBC charge sum and ZDC total deposited energy as shown in Fig.(3.2): the more central the collision, the less "spectator" neutrons reach the ZDC and the more charged hadrons are emitted from the collision towards the BBC. From such a plot we can find the fraction of the total *AuAu* inelastic cross section produced in a particular event (the centrality class of that event) by using the so called "clock" method as shown

in the upper panel of Fig.(3.2). The lower panel of this figure shows the charged hadron multiplicity distribution and how different centrality classes contribute to it (more central events have more charged hadrons).

Then Glauber calculations are used to extract physical quantities like the number of collisions (N_{coll}) and the number of participants (N_{part}). A Glauber model [41] describes nuclear collisions based on the collision geometry (in the absence of any nuclear medium effects) and the elementary total nucleon-nucleon inelastic cross section (from which the nucleon mean free path is obtained).

3.3 Charged Hadron Tracking Detectors

The central spectrometer arms measure the transverse momentum (p_T) and emission direction (ϕ and θ) of charged particles produced in each collision by tracking them in the central arm magnetic field: the global detectors are used to measure the emission z_{vtx} coordinate (displaced vertices are neglected: $x_{vtx} \equiv y_{vtx} \equiv 0$), the tracking chambers are used to measure the exit (x,y,z) coordinates and direction vector from the magnetic field, and a detailed knowledge of the magnetic field map is subsequently used to reconstruct the trajectory and kinematics of charged particles.

The **central magnet** is energized by two pairs of concentric coils that generate an axially symmetric field along the z axis such that *charged particles are bent in the transversal (xy) plane*. The field strength is about 0.48T at $r = 0$ and has an approximately Gaussian dependence on the radial distance. A significant z component develops towards the edge of the magnetic field region ($r \sim 2m, z \sim 80cm$), with an overall focusing effect. We should note that the innermost part of the first tracking chamber (the Drift Chamber) has a residual magnetic field. Fig.(3.3) shows the PHENIX central and muon magnets.

The **Drift Chambers** (DC) are placed between 2 and 2.5 m in radial distance from the interaction point and occupy 1.8 m in the z direction and a 90° sector in ϕ . A DC consists of 40 planes of sensing wires divided in 80 drift cells, arranged in 6 layers - X1, U1, V1, X2, U2, V2 in increasing radial order. The X layers have 12 sense (anode) wires each, oriented parallel to the z axis for precise tracking in the transversal (xy) plane. The U and V layers have

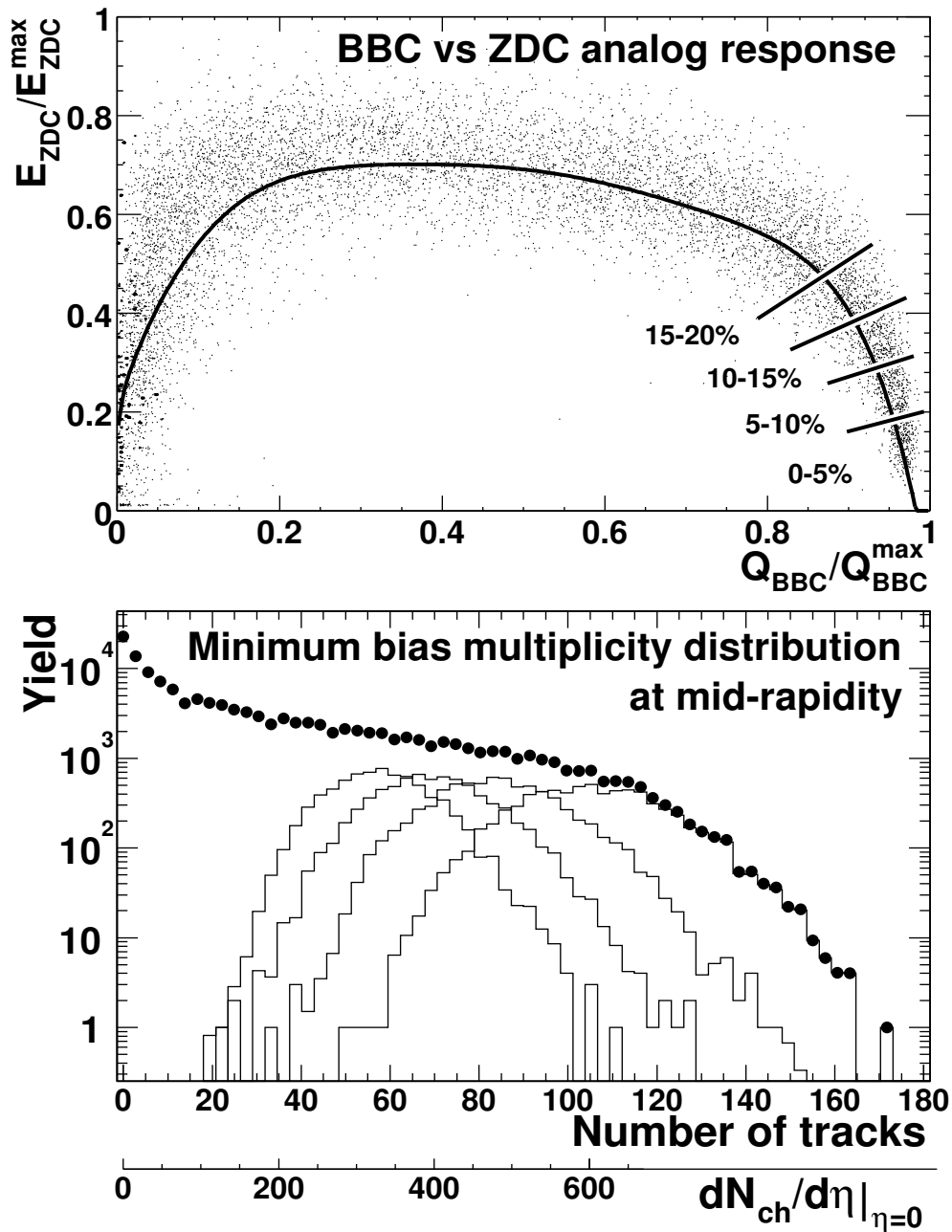
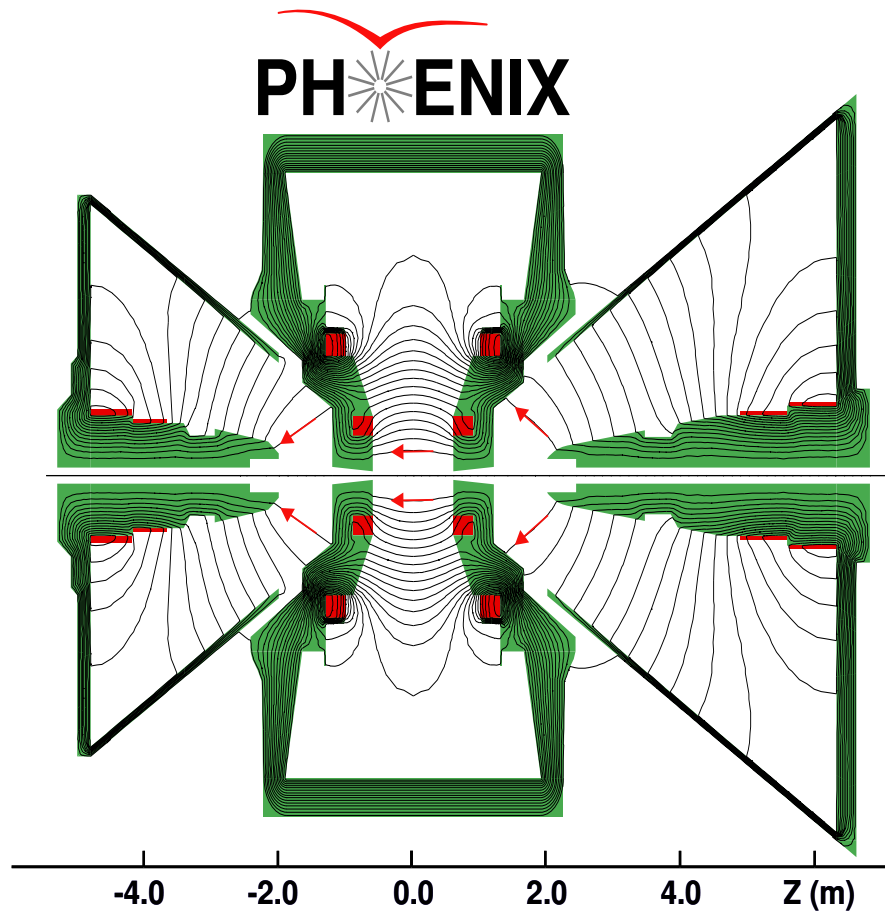


Figure 3.2 Upper Panel: The determination of collision centrality class using the correlation between the BBC charge sum and ZDC total deposited energy with the "clock" method; four examples of centrality classes are shown (0-5%, 5-10%, 10-15%, and 15-20%). Lower Panel: charged hadron multiplicity distribution (filled circles) and its contributions coming from the above four centrality classes.



Magnetic field lines for the two Central Magnet coils in combined (++) mode

Figure 3.3 The PHENIX Magnet: both central arm and muon arm magnets with their field lines are shown.

4 sense (anode) wires each, with $\pm 6^\circ$ stereo angles with respect to the z axis for the precise measurement of the z coordinate of the track, in conjunction with PC1 hit information. DC is intended to provide high resolution p_T measurements and participate in the pattern recognition by providing tracking information that is used to link tracks in the various PHENIX central detector subsystems together.

In order to perform these two functions DC provides the following performance parameters:

- single wire spatial resolution better than 0.15 mm
- single wire two track separation better than 1.5 mm
- spatial resolution in Z direction better than 2 mm
- single wire efficiency better than 95%

The **Pad Chambers** (PC) are thin proportional chambers with one plane of anode wires in a gas volume within two cathode planes. The two PCs used in this analysis (we do not use PC2 because it is installed only in the west central arm) have the following parameters:

Table 3.1 Pad Chamber Parameters; (v_1, v_2) correspond to values in the transversal plane (v_1) and in the z direction (v_2)

	Radius	Pad Size	Single Hit Res	Double Hit Res	Rad Length
PC1	2.45m	$(0.84, 0.85)cm^2$	$(2.5, 1.7)mm$	$(2.8, 2.4)mm$	$1.2\%X_0$
PC3	4.90m	$(1.60, 1.67)cm^2$	$(4.6, 3.6)mm$	$(5.3, 5.0)mm$	$2.4\%X_0$

The PCs measure 3-dimensional hit points of charged hadrons with very good resolution and efficiency ($> 99\%$). PC1 is used together with the DC in charged particle tracking (see below); the generated tracks are matched to PC3 hits in order to reduce the combinatorial background.

The **Ring Imaging Cherenkov Detectors** (RICH) are made from a big vessel ($40m^3$ volume) filled with radiator CO_2 gas that emits Cherenkov photons for electrons above $\sim 20MeV/c$ and charged pions above $\sim 5GeV/c$. In the back of the vessel, two large spherical mirrors ($20m^2$ reflecting area) focus the Cherenkov light onto two arrays of Photo-Multiplier Tubes (PMTs) with

peak quantum efficiency of 27% and timing resolution of 250ps. The mean number of photo-electrons per ring is 10.8 and the ring radius is about 11cm. The e/π separation is at a 10^4 level for single tracks.

The RICH is a detector specially built for electron identification in the central arms. Since the main source of physical background in our analysis are conversion electrons (see comments in Section 2.6), we use it to veto electron tracks. More precisely, we require that there are no fired PMTs associated with our tracks.

The **DC-PC1 charged particle tracking** in PHENIX is based on a Hough transform technique, which is a general technique for translating a list of points into lines (tracks) by using a special parameter space. For example, one point in the (slope, intercept) space corresponds to a line; therefore, all the points which lie in a line will produce a peak in this Hough space.

Hence, the charged particle *tracking model* (trajectory reconstruction) is developed as follows:

1. transform DC hits in the X layers (on average 12) into lines - a (x, y) point and a direction vector with their errors.
2. reconstruct tracks in the (x, y) plane by mapping the above lines in the Hough space defined by azimuth angle (ϕ) and inclination angle (α) with respect to some reference circle, which we placed at $R=220\text{cm}$ between the X1 and X2 wire layers, as shown Fig.(3.4). Peaks in a histogram of ϕ versus α for all X1-X2 lines combinations correspond to DC tracks.
3. associate X hits with the reconstructed track simply by looping over the hits and determining the closest hit to each track within each plane. Any track sharing a majority of its hits with other tracks is removed from the track list.
4. use PC1 hits, BBC vertex position z_{vtx} , and UV hits to track also in z . First, search for PC1 candidate hits within $\pm 2\text{cm}$ from the DC track in the transversal plane determined above. Then, since tracks bend very little in z (barring residual effects at the edge of the magnetic field region), straight lines between z_{vtx} and candidate PC1 z give the track candidate z information. Finally, from all combinations, the one with the most UV hits associated in the DC is declared the correct track.

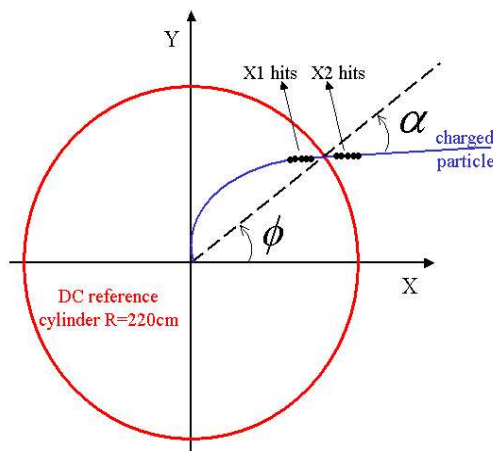


Figure 3.4 Charged Particle Tracking in DC: hits in the X1 and X2 layers are used to reconstruct the charged particle track through a Hough transformation in the (α, ϕ) space.

The track model produces an overall *quality parameter* for the track, depending on how many X, UV, and PC1 hits are associated with it and on the reliability of this association. For example, a candidate PC1 hit can have a good number of UV hits associated, but they can also be associated with candidate PC1 hits for other tracks, so the association is ambiguous; this would reduce the quality associated to the track.

Once we have the track, we use our knowledge of the magnetic field map to reconstruct the kinematics of the charged particle at the vertex (transverse momentum and emission direction): a four dimensional field integral grid $f(p, \theta, r, z)$ (where p is the momentum, θ is the polar angle at the vertex, and r is the radial distance) is generated for the entire extent of the central arms by swimming charged particles through the magnetic field map from survey measurements and numerically integrate at each grid point to obtain $f(p, \theta, r, z)$. The momentum resolution of the PHENIX central arm spectrometers is $\delta p/p \simeq 0.7\% \oplus 1\% \cdot p$.

Also, the above DC-PC1 track is projected to all the outer detectors in the central arms. Then, the closest hit to the projection is found and the ϕ and z

residuals:

$$\Delta\phi \equiv \phi_{hit} - \phi_{proj}, \quad \Delta z \equiv z_{hit} - z_{proj} \quad (3.1)$$

are calculated. The means ($\bar{\phi}$ and \bar{z}) and widths (σ_ϕ and σ_z) of the Gaussian distributions of these residuals are parameterized as a function of p_T and experimental run number. Finally, a *matching cut* of $n\sigma$ means that for each track we require:

$$(\Delta\phi - \bar{\phi}(p_T))^2/\sigma_\phi^2(p_T) + (\Delta z - \bar{z}(p_T))^2/\sigma_z^2(p_T) < n^2 \quad (3.2)$$

where p_T is the transverse momentum of the track.

3.4 Electromagnetic Calorimeters

The **Electromagnetic Calorimeters** (EMCal) measure with very good resolution the 3 dimensional hit position and energy of electromagnetic showers (electrons and photons). Hadronic showers (mesons and baryons) are also detected with significantly lower efficiency and resolution. The EMCal also provides particle identification - shower shape and time of flight are used to separate the following classes of particles: electrons/photons, charged mesons, and protons/neutrons. The west central arm has four sectors of lead scintillator calorimeter, while the east central arm has two sectors of lead scintillator calorimeter and two sectors of lead glass scintillator.

The **lead-scintillator** (PbSc) calorimeter is a honeycomb type of sampling detector consisting of 15552 towers (alternating tiles of lead and scintillator) and covers an area of approximately 48 m^2 . The main characteristics are:

- light yield of about 12,500photons/GeV of deposited electromagnetic energy.
- energy resolution $\sigma(E)/E = 8.1\%/\sqrt{E[GeV]} \oplus 2.1\%$.
- position resolution $\sigma_x(E, \theta) = \sigma_0(E) \oplus L_{rad} \sin \theta$, where θ is the incidence angle, L_{rad} is the radiation length (~ 18 for electromagnetic showers and ~ 1 for hadronic showers), and $\sigma_0(E)[mm] = 1.55 \oplus 5.7/\sqrt{E[GeV]}$ is the position resolution at normal incidence.

- timing resolution for an energy deposition $> 400\text{MeV}$ of about 120ps for electrons(photons) and protons, and of 270ps for charged pions (which have larger shower fluctuations).
- π^0 mass resolution after shower shape and time of flight cuts of 15MeV.

The **lead-glass** (PbGl) calorimeter is a Cherenkov type detector consisting of 9216 modules and covers an area of approximately 16 m^2 . The main characteristics are:

- energy resolution $\sigma(E)/E = 5.9\%/\sqrt{E[\text{GeV}]} \oplus 0.8\%$.
- position resolution $\sigma_x(E)[\text{mm}] = 8.4/\sqrt{E[\text{GeV}]} \oplus 0.2$.
- timing resolution $\sigma_t(E)[\text{ns}] = 3.75/\sqrt{500E[\text{GeV}]} \oplus 0.075$ similar for electrons and charged pions.
- π^0 mass resolution after shower shape and time of flight cuts of 13MeV.

Time of flight (tof) T measurements are done by using the BBC collision time as start signal and the EMCal hit time as stop signal. For hadronic showers, a matching cut with the projection of the closest track is applied to determine the momentum p and path length L (see track model and matching cut description at the end of Section 3.3), and from all these quantities we can determine the *mass* of the charged hadron:

$$M^2 = p^2 \left(\frac{T^2 c^2}{L^2} - 1 \right) \quad (3.3)$$

Electromagnetic and Hadronic Shower Shape measurements: since electromagnetic (γ, e^\pm) and hadronic ($\pi^\pm, k^\pm, p, \bar{p}, n, \bar{n}$) particles produce quite different patterns of energy sharing (showers) between calorimeter towers, second moments of these showers are used to differentiate between them. More specifically, one uses an analytical parametrization of the energy sharing and its fluctuations in measurements of shower shapes produced for electron test beams; a *shower shape* χ^2 is defined:

$$\chi^2 \equiv \frac{\sum_i (E_i^{\text{predicted}} - E_i^{\text{measured}})^2}{\sigma_i^2} \quad (3.4)$$

where $E_i^{measured}$ is the measured energy deposited in the i^{th} tower of the shower and $E_i^{predicted}$ is the predicted deposited energy in the i^{th} tower, from the above parametrization, for a given total energy of the shower of $E_{tot} \equiv \sum_i E_i^{measured}$ and position of the tower. Hence, χ^2 defined as above characterizes how "electromagnetic" is the shape of a shower. Fluctuations are also parameterized in this model and the χ^2 distribution is very close to the theoretical one and nearly independent of energy and impact angle of the electron. A $\chi^2 < 3$ corresponds to 90% electron efficiency - see the cluster χ^2 distribution of 2 GeV/c test beams of electrons and charged pions in Fig. 7 (page 532) of the PHENIX calorimeter section of the quoted NIM issue [23].

CHAPTER 4. Data Analysis

In this chapter, we will present the details of the data analysis: the selection of events and particle pairs, the construction of azimuthal correlation functions (CF) from these pairs, and the extraction and correction of the physical parameters from CFs. All the principles and equations that form the foundation of our approach have been detailed in Chapter 2, so this chapter will elaborate on the technical methods used to apply them.

The same analysis is performed for pp and $AuAu$ collisions. When differences appear, we will specify for which type of event that particular part of the analysis applies.

4.1 Data Selection and Quality Analysis

This section deals with the selection of the data that is appropriate for our physics goals. First, we present the quality analysis performed in order to choose experimental runs with a good performance of the PHENIX subsystems relevant for this analysis. Then, we discuss the event selection and the possibility of trigger biases in the pp analysis. The last two subsections describe single particle and particle pair selection.

4.1.1 Run and Event Selection

All the results presented in this work are based on the analysis of pp and $AuAu$ collisions at $\sqrt{s_{NN}} = 200\text{GeV}$, collected during the PHENIX Run-2 data taking period.

The **run quality analysis** (QA) criteria that have been used for the selection of good runs are:

- **detector QA:** is based on run-by-run information about the performance of each subsystem, stored in the PHENIX online database as

a quality flag that we use to select good runs.

- **physics QA:** the variation of several global physics quantities with run number is studied and runs with deviations larger than 3 standard deviations from the mean are discarded. The quantities being watched are: mean number of charged particle tracks, mean p_T of charged particle tracks, matching to PC3 hits, energy over momentum ratio of electron candidates, proton mass with the TOF detector.

Specific QA for the correlation analysis has been performed also. The method was to split runs into 5000 event segments and assess the degree of difference between their mixed event $\Delta\phi$ distributions based on a χ^2 analysis. A large χ^2/ndf implies that the detector performance changed during that run in such a way that the basic quantity of our analysis ($\Delta\phi$) was affected. Only a very small number (two) of additional "bad" runs were found using this method.

The **event selections** used are:

- minimum bias triggers; in pp collisions we use ERT triggers also (see below).
- $|z_{vtx}| < 30cm$

$AuAu$ correlation functions are classified into the following six centrality classes of the collision: (1) 0-5%, (2) 5-15%, (3) 15-25%, (4) 25-40%, (5) 40-60%, (6) 60-92%. The PHENIX minimum bias Level-1 trigger is sensitive to $92 \pm 2\%$ of the inelastic $AuAu$ cross section. See Section 3.2 for details on centrality determination.

Apart from minimum bias trigger data, in pp analysis we have included also ERT triggered events. See Section 3.2 for the description of PHENIX Level-1 triggers. This can lead to various **trigger biases**, the most obvious being a bias on the inclusive p_T -distribution: the $\langle p_T \rangle$ value within a given p_T -bin is different for different trigger types. This produces a narrowing of the correlation functions because the trigger preferentially selects higher p_T hadrons, which have tighter standard deviations in both near and away regions ($\sigma_{N,A}$ decreases with $\langle p_T \rangle$).

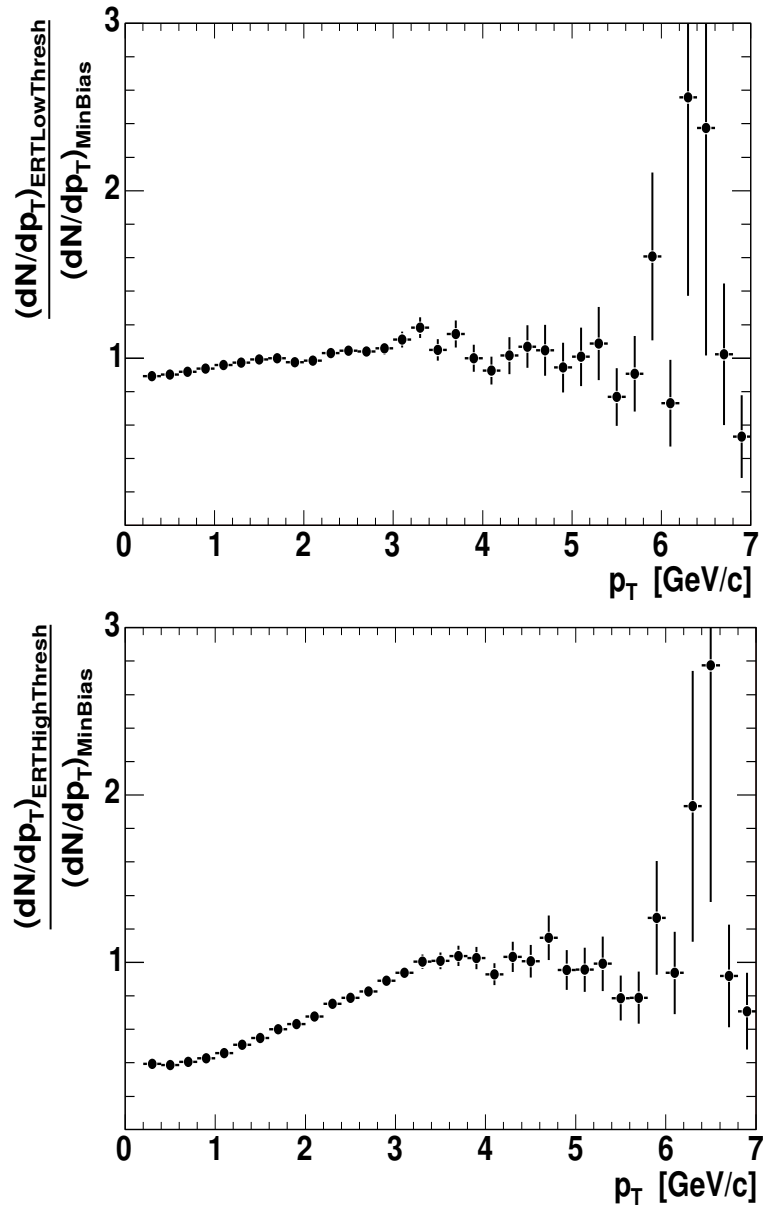


Figure 4.1 $\langle p_T \rangle$ shift in ERT triggered pp collisions. Upper Panel: Ratio of ERT low threshold and Minimum Bias p_T distributions. Lower Panel: Ratio of ERT high threshold and Minimum Bias p_T distributions.

In order to quantify the $\langle p_T \rangle$ shift, we plot the ratio of p_T distributions in ERT and minimum bias triggered events, shown in Fig.(4.1.1), for both versions of the ERT trigger: low threshold ($\sim 300\text{MeV}$) and high threshold ($\sim 800\text{MeV}$). The ratio of spectra were normalized at high p_T .

The $\langle p_T \rangle$ in a p_T -bin shifts proportionally to the variation in slope. This happens in the region where the efficiency of the ERT trigger is not yet saturated (the ratio of p_T distributions in ERT events and min bias events is not flat). The p_T -distribution in ERT triggered events with low threshold has a very small increase over min bias (basically, for all practical purposes, this version of the ERT trigger can be treated as a minimum bias sample), while that with high threshold has a larger increase (a factor of 3 over 3GeV). However, since the p_T -distribution is steeply falling, even this larger relative increase has still small impact on $\langle p_T \rangle$. This is demonstrated in Table(4.1), where the $\langle p_T \rangle$ value is shown for p_T bins below the saturation region and different trigger types used in this analysis. The relative variation of $\langle p_T \rangle$ is less than 0.5%, which means that we can safely neglect ERT trigger biases.

Table 4.1 The mean p_T values for the 3 different trigger configurations (minimum bias, ERT low threshold = 0.3 GeV and ERT high threshold = 0.8 GeV) for the p_T bins below the saturation region.

	0.75–1.	1.–1.5	1.5–2.	2.–2.5	2.5–3.	3.–4.
MinBias	0.862	1.200	1.705	2.209	2.707	3.371
ERTLow	0.863	1.201	1.705	2.210	2.710	3.373
ERTHigh	0.864	1.208	1.712	2.214	2.716	3.380

4.1.2 Single Particle Selection

For **the selection of charged hadrons** we used the following criteria:

- $1.5 < p_T < 5$ GeV/ c in $AuAu$ analysis in order to reduce the main background contributions (fake high- p_T tracks from resonance decays at low p_T , and conversion electrons at high p_T). See discussion in Section 2.6.
- track model quality 31 or 63, which corresponds to the highest track quality (all X1,X2,UV1,UV2 and PC1 hits are found and their associa-

tion with the track is unique). See details about the tracking model in Section 3.3.

- 2- σ radial matching cut in $\Delta\phi$ and Δz at PC3, as described by Eq.(3.2), to reduce the combinatorial background.
- RICH veto (no RICH PMTs associated to the track) and $|Z_{DC}| \leq 75\text{cm}$ (a lot of conversion electrons are generated in the DC frame) in order to reduce conversion electron background.

In order to estimate the combinatorial background, let us consider the following charged hadron minimum bias p_T spectra in the west central arm: (A) after applying the cuts from the above list; (B) after applying the same cuts from the above list, plus a PC2 2- σ radial matching cut; (C) after applying the cuts from the above list, except that a "flipped" PC3 2- σ radial matching cut (see below) is used instead of the normal PC3 2- σ radial matching cut. Matching with PC2 (which has similar characteristics with the outer pad chamber that we use - PC3) gives us information about the effect of the matching cut on p_T spectra. Matching with a flipped outer detector is a standard technique to estimate combinatorial background: if a DC-PC1 track reconstructed in an arm matches a hit in the PC3 from the other arm (geometrically flipped in the software before the matching), then it can only be a random match. Then, the ratio of the p_T spectra with matching to "flipped" PC3 and the p_T spectra with matching to "normal" PC3 gives an estimate of the fraction of charged hadron tracks with random (combinatorial) PC3 association.

In Fig.(4.2), we estimate the **charged hadron combinatorial background** by plotting the (B)/(A) (squares) and (C)/(A) (circles) ratios of charged hadron p_T spectra. We can see that the background contribution starts to become important above $\sim 5\text{GeV}/c$.

For **the selection of π^0 s** we used following criteria:

- cluster energy $> 500\text{MeV}$ in order to avoid the Minimum Ionizing Peak (MIP) contributions of charged hadrons.
- track veto: any cluster that matches a track within 2- σ is rejected.
- time of flight cut: $|Tof| < 1.2\text{ns}$

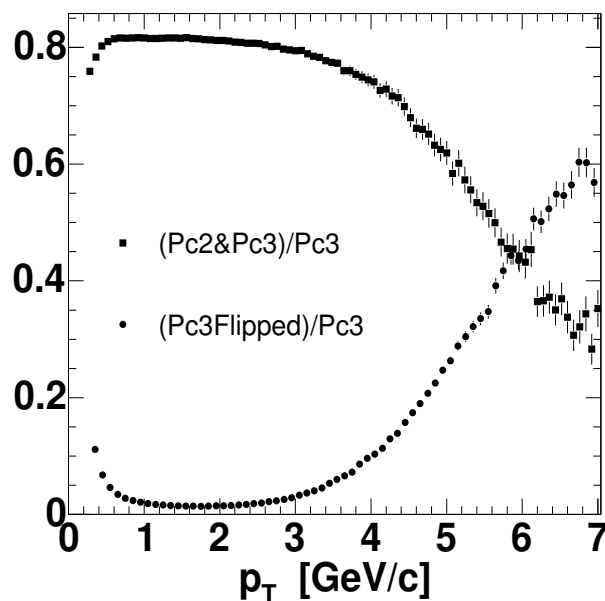


Figure 4.2 Estimation of charged hadron combinatorial background through the effect of outer pad chamber association on the p_T distribution (see text).

- shower shape cut: $\chi^2 < 3$; see Eq.(3.4) and comments for details.
- energy asymmetry cut for π^0 : $\alpha \equiv |E_{\gamma 1} - E_{\gamma 2}| / (E_{\gamma 1} + E_{\gamma 2}) < 0.7$. Simulations of π^0 decays for $p_T(\pi^0) > 1 \text{ GeV}/c$ show that α is flat up to ~ 0.7 , followed by a strong decrease up to 1; on the other hand, combinatorial photon pairs have a flat asymmetry distribution in the entire $0 \leq \alpha \leq 1$ region, so the above cut increases the π^0 signal over background ratio by about 20-30%.

4.1.3 Particle Pair Selection

In a high multiplicity environment many distortions can appear at small relative distances or angles: *hit merging* happens due to detector resolution when they are too close to each other, *track splitting or duplication* happens in the track reconstruction software producing so-called "ghost" tracks. A major source of correlation distortions are track pairs that share track segments. All these effects produce shape distortions of the correlation function at small relative azimuthal angle.

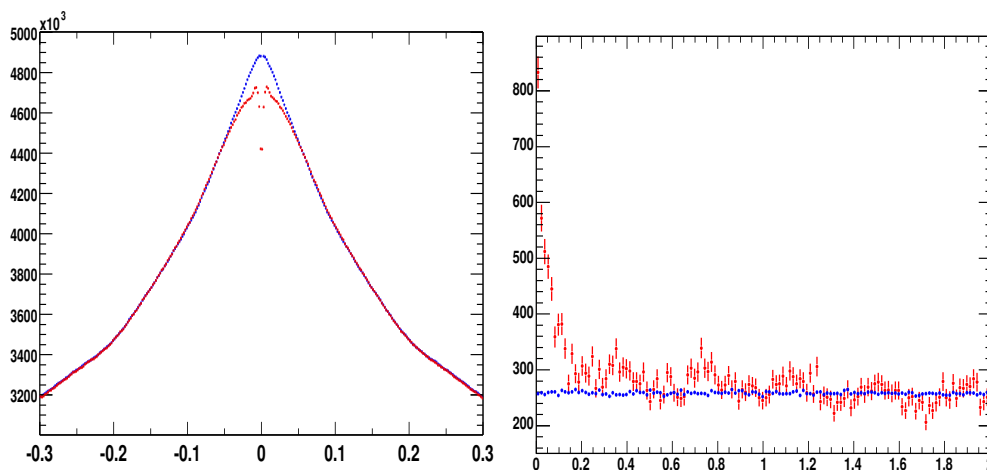


Figure 4.3 Drift Chamber "Ghost" Tracks Cut: we compare the measured (red) and mixed (blue) $\Delta\phi_{DC}$ (left panel) and Δz_{DC} (right panel) distributions and cut out the regions where they do not match.

We use a mixed event technique (see Section 4.2.2) to identify and reject pairs of particles affected by such distortions. The method is: first apply all the single-particle selections described in the previous section; then, for each detector involved in the analysis (DC, PC1, PC3), compare the measured and mixed event distributions of relative distance variables (specific to that detector) of particle pairs:

- Ghost Track Cuts: $|\Delta\phi_{DC}| > 50\text{mrad}$ and $|\Delta z_{DC}| > 0.2\text{cm}$ based on Fig. 4.3, where the measured (red) and mixed event (blue) distributions are plotted for these drift chamber variables. The deviations at small $\Delta\phi_{DC}$ and Δz_{DC} are produced by track duplication or splitting which artificially changes the number of tracks. The periodical "bumps" in the Δz_{DC} distribution are related to the granularity of the tracking chamber along this coordinate, but they show up only for $\Delta\phi_{DC} < 50\text{mrad}$, so this cut eliminates them.
- PC Hit Resolution Cuts: $\Delta R_{PC1} > 10\text{cm}$ and $\Delta R_{PC3} > 15\text{cm}$ based on Fig. 4.4 - the ratio of measured and mixed distributions of in-plane radial distance $\Delta R(\equiv \sqrt{(\Delta x)^2 + (\Delta y)^2 + (\Delta z)^2})$ of PC hits associated with track pairs. The dip at small ΔR is produced by hit merging which artificially

decreases the number of hits. Its size corresponds to the hit resolutions in PC1(4cm) and PC3(8cm).

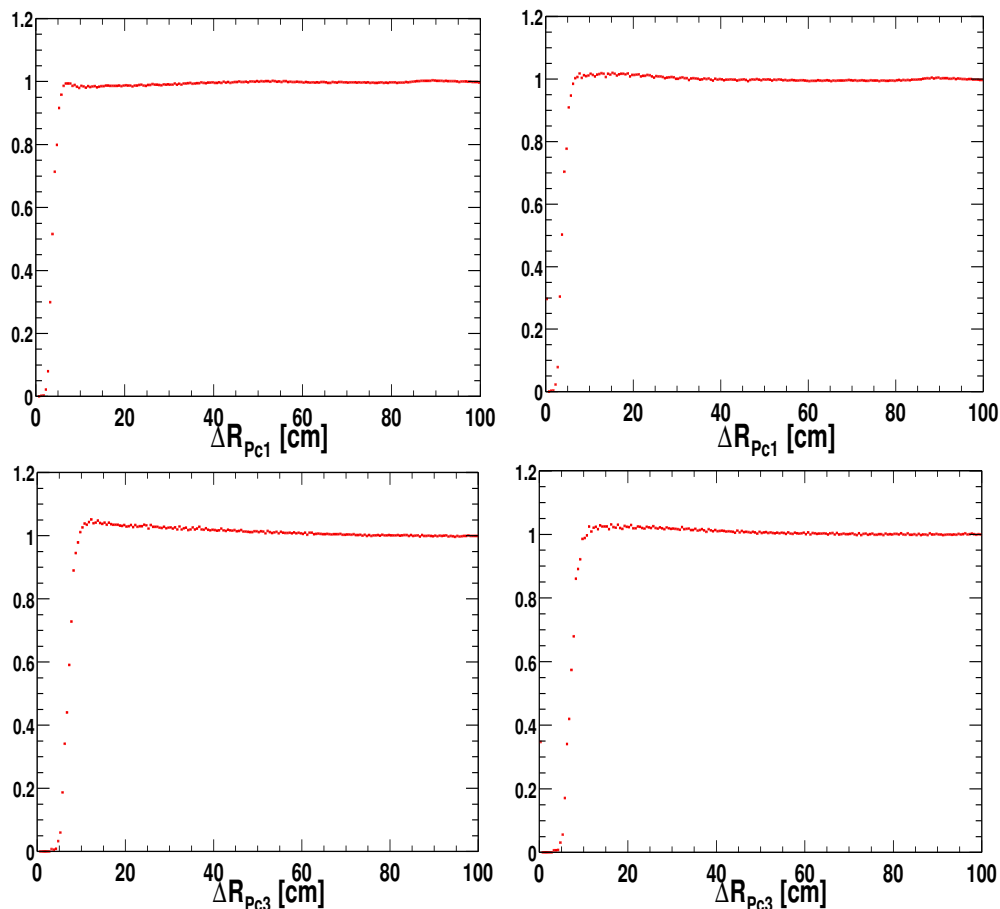


Figure 4.4 Pad Chamber Resolution Pair Cuts: Ratio of measured and mixed ΔR distributions for Pad Chamber (PC) hits associated with charged track pairs: Upper Left - PC1, opposite charge. Upper Right - PC1, same charge. Lower Left - PC3, opposite charge. Lower Right - PC3, same charge.

Not all the features of these small distance distributions are completely understood, however we always cut out the regions where the measured and mixed event distributions do not match. Studies have shown that these two-particle effects have a large impact on azimuthal correlation functions only at low p_T and high centrality. The reason is that they are obviously dependent on the multiplicity environment.

Another two-particle cut that we apply each time pairs of identical hadrons are used is the HBT cut: at low relative momenta, pairs of identical hadrons are correlated due to the Handbury-Brown-Twiss (HBT) effect. These correlations have been measured by PHENIX [12] and we eliminate their contribution by requiring that the invariant Q^2 of the pair is larger than 100MeV, which is actually quite conservative. Since our analysis uses only $p_T > 1.5\text{GeV}/c$ particles, the impact of this type of correlations is negligible.

4.2 Azimuthal Correlation Functions

4.2.1 Definition and Normalization

The azimuthal correlation function (CF) is constructed, using the mixed event technique, as follows:

$$C(\Delta\phi_i) \equiv \frac{N_{meas}(\Delta\phi_i)}{N_{mix}(\Delta\phi_i)}, \quad 1 \leq i \leq N_{bins} \quad (4.1)$$

where $N_{meas}(\Delta\phi_i)$ is the measured number of particle pairs in the i^{th} bin of the relative azimuthal angle distribution and $N_{mix}(\Delta\phi_i)$ is the same quantity, but for pairs of particles from *different* events. For details on how the mixed event relative azimuthal angle distribution is constructed, see next section. Obviously the number of entries of this distribution depends on the size of the event pool for mixing, a non-physical quantity. This is why we need to normalize a correlation function introduced as in Eq.(4.1).

As follows from the definition of the correlation function, if there is no correlation, the values of $C(\Delta\phi_i)$ are equal to unity for any relative angle bin i . Hence, for a CF constructed in the $-\pi < \Delta\phi < \pi$ range, the natural normalization is that the integral should be

$$\int_{-\pi}^{+\pi} C(\Delta\phi)d\Delta\phi = 2\pi \quad (4.2)$$

This is a **constant area normalization** and it eliminates the residual correlations induced by multiplicity fluctuations in the centrality interval where the two particle correlations are defined (see details in Section 2.6).

In order to fulfill the normalization in Eq.(4.2), we define the CF as follows:

$$C(\Delta\phi_i) \equiv \frac{N_{meas}(\Delta\phi_i)}{N_{mix}(\Delta\phi_i)} \cdot \frac{1}{\sum_i N_{meas}(\Delta\phi_i)/N_{mix}(\Delta\phi_i)} \quad (4.3)$$

Obviously, when working with histograms, one has to bear in mind that

$$\sum_i C(\Delta\phi_i) = \frac{\int_{-\pi}^{+\pi} C(\Delta\phi) d\Delta\phi}{bw} = N_{bins} \quad (4.4)$$

where $bw = 2\pi/N_{bins}$ is the bin width and N_{bins} is the number of bins of the CF.

The general form of CFs in the two source model developed in Section 2.5, within the Gaussian jet profile approximation, can be expressed as

$$C(\Delta\phi) = \mathcal{F}(1 + 2V_2^2 \cos 2\Delta\phi) + \frac{S_N}{\sqrt{2\pi}\sigma_N} \exp\left(-\frac{\Delta\phi^2}{2\sigma_N^2}\right) + \frac{S_A}{\sqrt{2\pi}\sigma_A} \exp\left(-\frac{(\Delta\phi \pm \pi)^2}{2\sigma_A^2}\right) \quad (4.5)$$

where the effect of the dijet acoplanarity is incorporated in a broadening of the away side correlation ($\sigma_A > \sigma_N$), and the effect of the interference between the jet and collective sources is incorporated in a larger quadrupole magnitude V_2 . Of course, in pp or $p(d)Au$ collisions there are no quadrupole collective effects, so $V_2 \equiv 0$.

By fitting Eq.(4.5) to a CF one can extract the near/away conditional yields from the Gaussian areas $S_{N,A}$ and the total number of pairs n_{meas} :

$$n_{N,A} = \frac{1}{N_{trigg}} \frac{S_{N,A}}{2\pi} n_{meas}, \quad n_{meas} \equiv \sum_i N_{meas}(\Delta\phi_i) \quad (4.6)$$

and the jet shape parameters $\langle |j_{Ty}| \rangle$ and $\langle |k_{Ty}| \rangle$ from the Gaussian widths $\sigma_{N,A}$. Note that, since we are fitting histograms, the bin width has to be taken into account, so $S_{N,A}$ in Eq.(4.5) are actually $bw \cdot S_{N,A}$.

The multiplier \mathcal{F} is the fraction of the total CF integral in the quadrupole modulation. It is not a free parameter, being constrained by the normalization condition in Eq.(4.2):

$$\mathcal{F} = 1 - \frac{S_N + S_A}{2\pi} \quad (4.7)$$

4.2.2 Mixed Event Technique

In the previous section, we introduced the two particle azimuthal correlation function (see Eq.(4.3)) using the mixing event technique.

By pairing particles from different events, the mixed event $\Delta\phi$ distribution contains all the detector induced azimuthal correlations, like the correlations induced by efficiency fluctuations, but none of the physical ones. Therefore, by dividing it out from the measured $\Delta\phi$ distribution, which contains both the physical and the detector induced correlations, we extract only the physical correlations. Also, the mixed event distribution gives a good description of the detector acceptance, so it corrects the shape of the correlation function for acceptance effects. Note that it is only the shape that is corrected; pair loss due to such effects must be corrected otherwise.

The actual technique of event mixing involves a rolling buffer of events with fixed depth (based on the principle first event in - last event out). The current event is the header of the buffer and its particles are correlated with particles from the other events in the buffer. However, *only one random particle* is used from each event in order to avoid introducing 2^{nd} order physical correlations: each event has at least one underlying collective correlation - flow. Hence, if one would correlate a particle from the header event with multiple particles from another event, one would then pick up all underlying collective correlations from that event.

The size of the mixing buffer (event pool) is bounded by two restrictions: it has to be smaller than the typical time interval of detector efficiency fluctuations (otherwise the average correlations induced by them would contribute differently in the measured and mixed distributions, defeating the purpose of the technique), and it has to be large enough such that the contribution of the mixed distribution to the statistical errors of the correlation function to be very small. Following these criteria, we used a depth of the mixing pool of 1000 events. This corresponds to at most 3 seconds of data taking, which is well within the stability period of our detectors, and it assured a contribution from mixed events to statistical errors of at most 9%.

The mixing pools are sorted by centrality and vertex position in the sense that two events are allowed to mix (enter the same pool) only if their centrality differs by at most 10% and their vertices differ by at most 3cm. This way, detector effects, which are potentially multiplicity and vertex dependent, are

properly taken into account.

4.2.3 Fitting Methods for $AuAu$ analysis

As described in Section 4.2.1, we construct two-particle correlation functions (CFs) according to Eq.(4.3) and we fit them with Eq.(4.5) in order to extract the four parameters we are interested in: $\sigma_{N,A}$ and $S_{N,A}$. In pp (and dAu) collisions, where $V_2 \equiv 0$, this strategy works very well.

However, in $AuAu$ collisions, the away (dijet) Gaussian broadens quickly with centrality, making the fit more and more difficult. The reason is very simple - the standard deviation of $1 + 2V_2^2 \cos(2\Delta\phi)$ is:

$$\sigma_{V_2} = \sqrt{\frac{\pi^2}{12} - V_2^2} \approx 0.8 - 0.9rad \quad (4.8)$$

depending on p_T and centrality. So, if any of the two Gaussians has a width comparable with or larger than σ_{V_2} , the fit would fail to resolve it from the background quadrupole modulation. This never happens with the near Gaussian because its width is always less than $0.5rad$ in the p_T region we are analyzing, but one can see even by visual inspection of the CF s presented in Fig.(E.1) that it does happen with the away Gaussian. The simple fit by Eq.(4.5) without any constraint or external information causes a major part of the quadrupole oscillation in the away region ($|\Delta\phi| > \pi/2$) to be assigned to the Gaussian.

Two types of approaches have been developed to address this problem:

Eliminate the quadrupole collective source by using the symmetry of the quadrupole modulation ($\sim \cos(2\Delta\phi)$) around $\pm\pi/2$.

In one approach, called **the normalization subtraction method**, the absolute value of the normalization F is calculated externally and subtracted from Eq.(4.5); then, the quadrupole correlation oscillates around 0 and has a null integral in both the near ($|\Delta\phi| < \pi/2$) and the away ($|\Delta\phi| > \pi/2$) regions, which allows the extraction of the jet integrals in these regions (but not the real jet integrals as argued bellow). The two issues with this approach are the sensitivity on the precise determination of F and the fact that, in order to get the full jet yields from the

above jet integrals, we also need some external information about the jet widths: the broadening of the away Gaussian makes it "leak" in the near region.

In our approach, called **the $\pi/2$ subtraction method**, the away region ($|\Delta\phi| > \pi/2$) of the CF is subtracted from the near region ($|\Delta\phi| < \pi/2$); see details below. This is probably the cleanest method, but it requires very good statistics, especially in the region of the CF around $|\Delta\phi| \approx \pi/2$; the PHENIX detector does not have very good coverage in this region.

Use external information about the quadrupole collective source to fix V_2 in the fitting procedure; then, even if the away Gaussian has the same shape (standard deviation) as the quadrupole modulation, the fit is successful because it can disentangle them based on their relative amplitudes.

In one approach, reaction plane analysis is used in various ways to get V_2 information.

In our approach, the fit is performed in two stages - V_2 is extracted in the first stage under some assumption, and it is fixed in a fit without assumptions in the second stage. The method will be detailed below.

In general, the major issue with this second type of approaches is the sensitivity of the away Gaussian parameters on the V_2 value used: a small variation in V_2 induces large variations in the extracted away Gaussian parameters (the usual problem of extracting a small signal on top of a large background by estimating the amount of background).

We will use two of the methods introduced above to attempt to disentangle the away Gaussian from the quadrupole modulation.

The $\pi/2$ subtraction method

Speculating the symmetry of the quadrupole correlation around $|\Delta\phi| = \pi/2$, we apply a simple transformation to the CFs: we fold the $|\Delta\phi| > \pi/2$ regions into the $|\Delta\phi| < \pi/2$ region (such that the points at $|\Delta\phi| = \pi$ correspond to the point at $\Delta\phi = 0$) and subtract. Fig.(4.5) shows the resulting *subtracted two-particle correlation functions* (SCFs) from $AuAu$ CFs of $3 \leq p_{Ttrigger} \leq 5 GeV/c$ trigger hadrons and $1.5 \leq p_T \leq 3 GeV/c$ associated hadrons for various centralities.

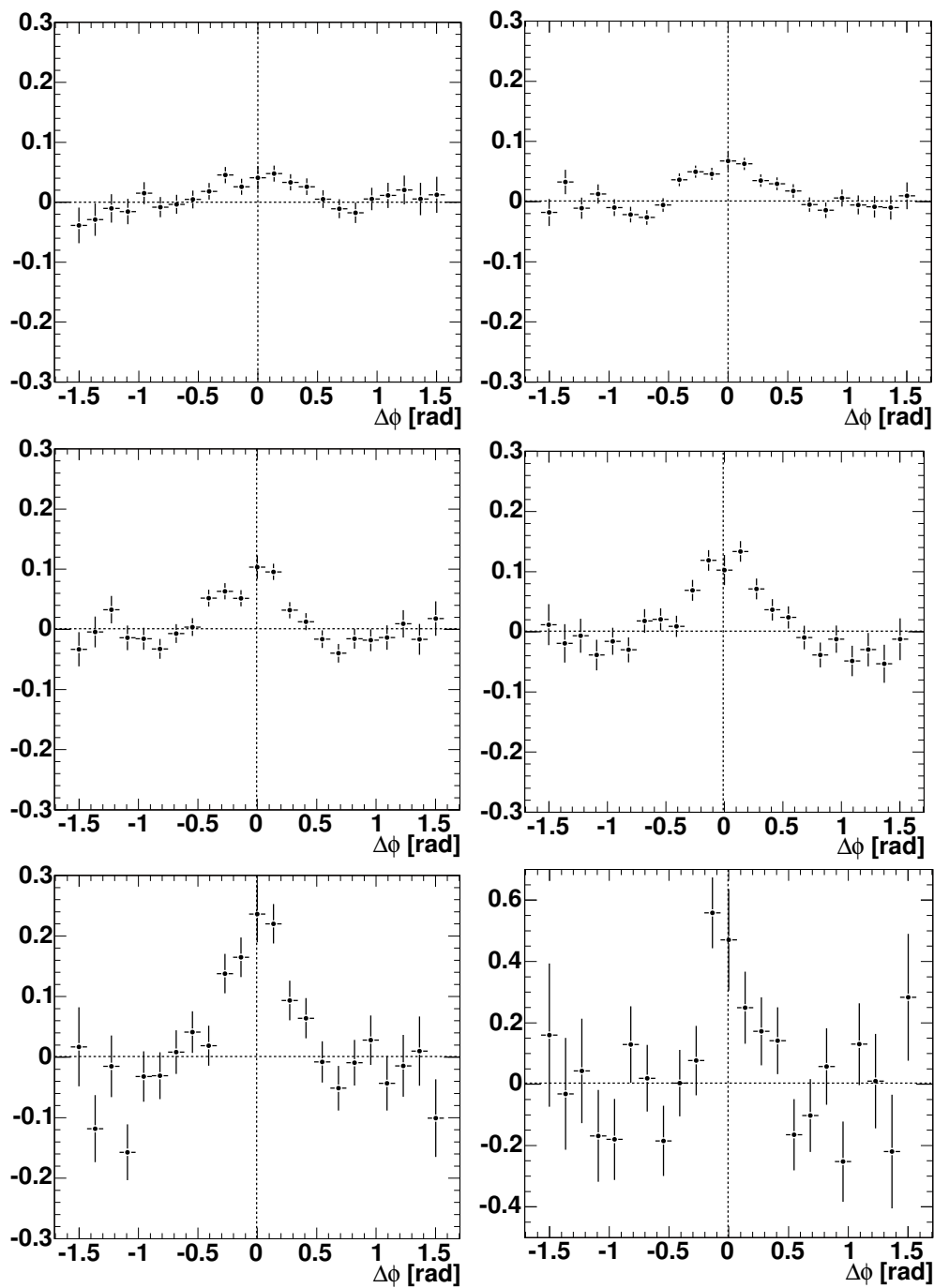


Figure 4.5 $\pi/2$ Subtracted Correlation Functions of $1.5 \leq p_T \leq 3\text{GeV}/c$ associated hadrons with $3 \leq p_{Ttrigg} \leq 5\text{GeV}/c$ trigger hadrons for the following centrality classes of the *AuAu* collision: top row - 0-5% left and 5-15% right; middle row - 15-25% left and 25-40% right; bottom row - 40-60% left and 60-90% right.

Before going further, let us outline a few facts. First, these SCFs contain **only** particle pairs from the jet source. Second, since $\sigma_A > \sigma_N$, they will have the typical shape of the difference between two Gaussians with different widths and, therefore, *the absence of a negative amplitude component is in itself a signature of the away Gaussian suppression*.

We can extract the jet parameters by fitting these SCFs with:

$$SC(\Delta\phi) = G(0, \sigma_N) - G(0, \sigma_A) + G(+\pi, \sigma_A) + G(-\pi, \sigma_A) \quad (4.9)$$

where $G(c, w)$ is a Gaussian centered at c of width w . In this equation, we used the fact that the near Gaussian is confined in the near region ($|\Delta\phi| < \pi/2$) and the away Gaussian "leaks" in the near region as centrality increases due to its broadening. Note that the integral of the SCF is:

$$\int_{-\pi/2}^{+\pi/2} SC(\Delta\phi) = \int_{-\pi/2}^{+\pi/2} C(\Delta\phi) - 2 \int_{\pi/2}^{\pi} C(\Delta\phi) = S_N + (1 - 2x)S_A \quad (4.10)$$

where

$$x \equiv \text{Erf} \left(\frac{\pi}{2\sqrt{2}\sigma_A} \right) \quad (4.11)$$

is the fraction of the away gaussian above $\pi/2$. An alternative implementation of the method involves using Eq.(4.10) as an additional constrain (left hand side is measurable from the SCF) on the usual fit of the CF.

We presented this method here for future reference, because of its simplicity and because we consider the SCFs interesting even without fits. Nonetheless, when fitting our current SCFs with Eq.(4.9), we get very large errors. The reason, as mentioned already, is that the method relies on the data points around $|\Delta\phi| \approx \pi/2$ and we do not have enough statistics there yet. So, we are going to use another method, outlined below, to extract the jet parameters.

The method of minimum jet amplitude point (MJAP)

The method of minimum jet amplitude point (MJAP) is inspired from N. Ajitanand's "ZYAM" (Zero Yield At Minimum) procedure [21], but it has a different implementation.

The fitting procedure is a minimization in the 5-dimensional parameter

space $(V_2, \sigma_N, \sigma_A, S_N, S_A)$ of:

$$\chi^2 \equiv \sum_i \frac{(C(\Delta\phi_i) - CF(\Delta\phi_i))^2}{\delta C(\Delta\phi_i)^2}, \quad 1 \leq i \leq N_{bins} \quad (4.12)$$

where $C(\Delta\phi_i)$ is the value of the correlation function in the i^{th} bin, $\delta C(\Delta\phi_i)$ is the error of this value, and $CF(\Delta\phi_i)$ is the value of the fit function given in Eq.(4.5) at $\Delta\phi_i$.

We start from the rough approximation that, at the point where the near and away Gaussians meet (which is the $\Delta\phi_{min}$ value at which the total jet amplitude has its minimum), the dominant contribution into the correlation function comes from the quadrupole source

$$CF(\Delta\phi_{min}) \approx F(1 + 2V_2^2 \cos(2\Delta\phi_{min})) + O(\Delta\phi_{min}) \quad (4.13)$$

and we apply the following two-step procedure:

- **Extraction of V_2 using the assumption of minimum jet amplitude point:** in every step of the χ^2 minimization procedure, we calculate the current minimum value $O(\Delta\phi_{min})$ of the total jet (Gaussian) amplitude ($\Delta\phi_{min}$ is the point where this function has its minimum). This value is then added in the χ^2 formula given by Eq.(4.12): $CF(\Delta\phi_i) \rightarrow CF(\Delta\phi_i) + O(\Delta\phi_{min})$. Since there is no other free parameter which may compensate for this additional offset (remember, in constant area normalization the normalization F is not a free parameter), the minimization algorithm will find the location in the parameter space with the best χ^2 value, where $O(\Delta\phi_{min})$ is smaller than the experimental error bars.
- **Free fit with V_2 fixed:** we fit the CF with Eq.(4.5) in which we fix the V_2 parameter to the value obtained in previous step, and drop all the assumptions made.

Extensive prior simulations (fits of Monte Carlo generated CFs with various shapes, one example being presented in Fig.(4.6)) have shown that the first step of the method returns a very accurate value for the quadrupole amplitude V_2 . The Gaussian parameters are returned accurately as long as their widths are narrower than $\sim 0.7 - 0.8rad$; once a Gaussian becomes broader than this, it is effectively truncated by the MJAP requirement. This is shown

in Fig.(4.7): the V_2 (and σ_N) is returned correctly, no matter how broad is the away Gaussian, but the away Gaussian width and area are returned systematically smaller than the input values when $\sigma_A > 0.7 - 0.8 \text{ rad}$. As a matter of fact, the outcome for σ_A saturates around this value, no matter what input value we use. Considering Eq.(4.8), it is not difficult to understand why.

Nonetheless, since V_2 always come out correct from this first step, we fix it in the second step, drop the MJAP assumption, and refit to get the jet parameters.

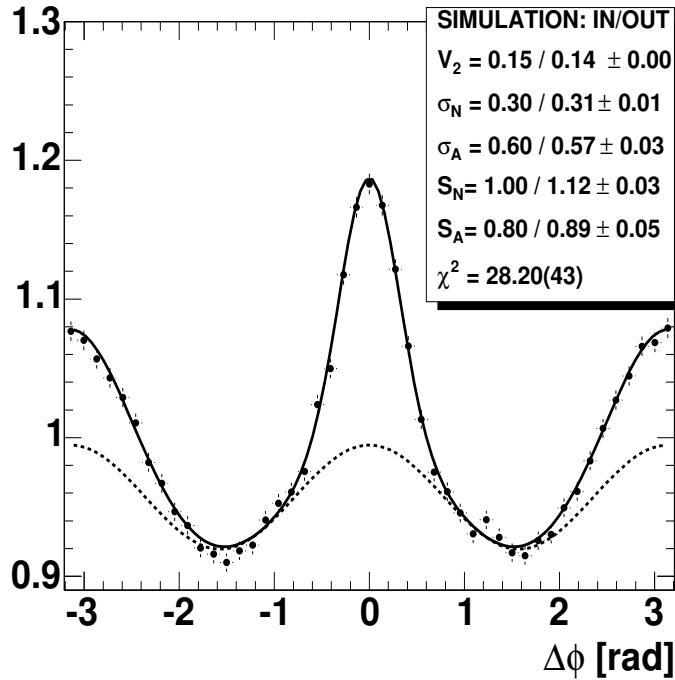


Figure 4.6 The Method of Minimum Jet Amplitude Point - Example of Monte-Carlo generated correlation function with its input and output parameters.

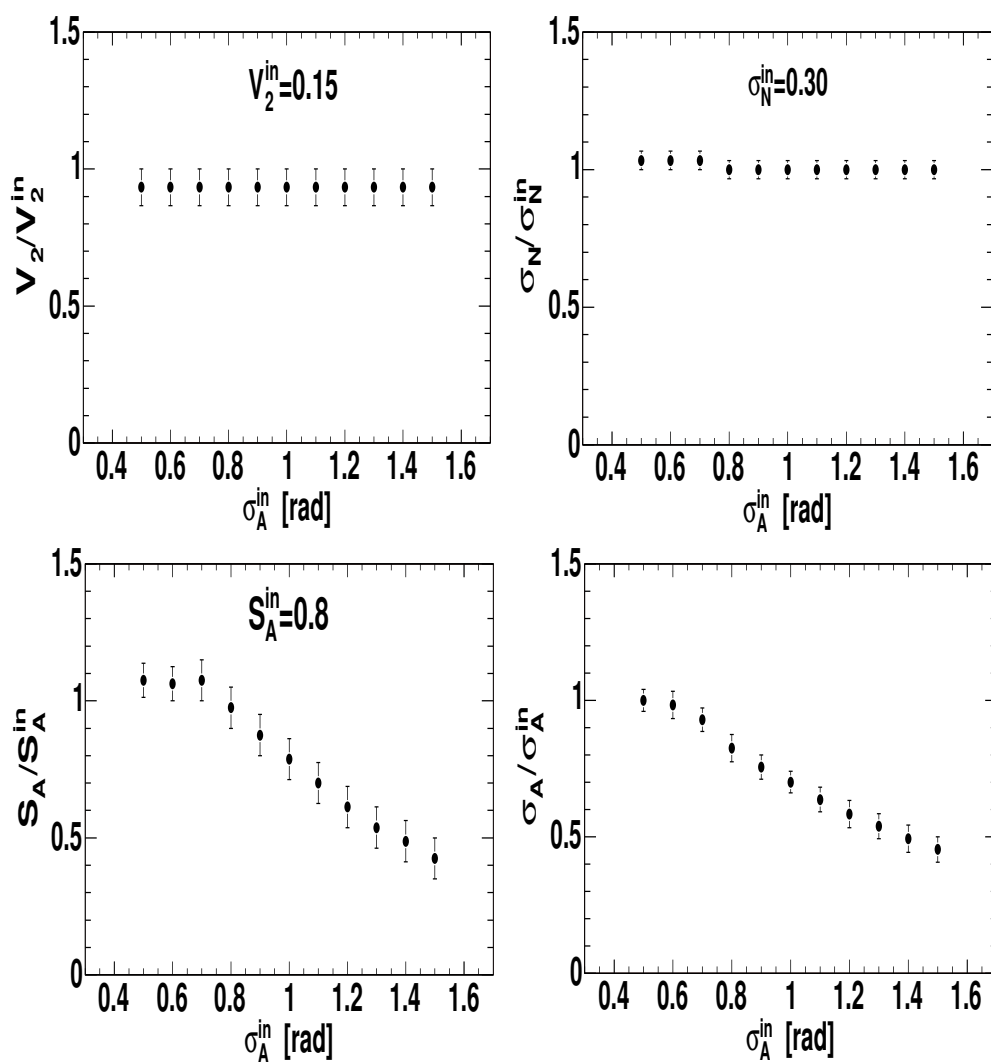


Figure 4.7 The Method of Minimum Jet Amplitude Point: ratios of output to input values for the simulated CF parameters as a function of the input away Gaussian width.

4.3 Acceptance and Efficiency Corrections.

The mixed event technique corrects only the shape distortions of azimuthal correlation functions due to detector efficiency and acceptance. This is enough for the shape parameters V_2 and $\sigma_{N,A}$, but not for the conditional yields $n_{N,A}$ - we must include a correction factor to account for the loss of associated hadrons Eq.(4.6). So the number of associated hadrons of transverse momentum p_T with a trigger particle of transverse momentum p_{Ttrigg} (the conditional yield) in a collision with N_{part} participants is calculated according:

$$n_{N,A}(N_{part}, p_T, p_{Ttrigg}) = \frac{1}{N_{trigg}(N_{part}, p_{Ttrigg})} \frac{S_{N,A}}{2\pi} n_{meas} \frac{F_{corr}(p_T)}{Eff(N_{part})} \quad (4.14)$$

where the correction term factorizes into a p_T dependent correction function $F_{corr}(p_T)$ due to acceptance loss of associated hadrons, and a multiplicity (N_{part}) dependent associated hadron efficiency correction function $Eff(N_{part})$.

Notes on the validity of Eq.(4.14):

- we supposed that the corrections for the associated and trigger hadron factorize:

$$F_{corr}(p_T, p_{Ttrigg}) \approx F_{corr}(p_T) \cdot F_{corr}(p_{Ttrigg}) \quad (4.15)$$

This is not true for pairs that are very close in space (in high multiplicity events), but we have excluded them by applying the pair cuts described in Section 4.1.3.

- the corrections for the trigger hadron $F_{corr}(p_{Ttrigg})$ do not need to be included since we compute yields per trigger hadron, so they cancel in the ratio.

The approximation in Eq.(4.15) allows us to use the correction factors extracted via simulations and charged hadron embedding techniques in the analysis of single charged hadron spectra [22].

- Single track p_T dependent correction (evaluated at $\langle p_T \rangle$ of the associated hadron):

$$F_{corr}(p_T) = A/p_T + B + C \cdot p_T + D \cdot p_T^2$$

$$A = 0.7512, B = 4.3982, C = -0.0586, D = -0.0020 \quad (4.16)$$

- Single track multiplicity dependent correction: shown in the left panel of Fig.(4.3).

$$Eff(N_{part}) = A + B \cdot N_{part} + C \cdot N_{part}^2$$

$$A = 0.995, B = -3.44 \cdot 10^{-04}, C = -3.05 \cdot 10^{-07} \quad (4.17)$$

Note that it is p_T independent only for $p_T > 1.5$ GeV/c

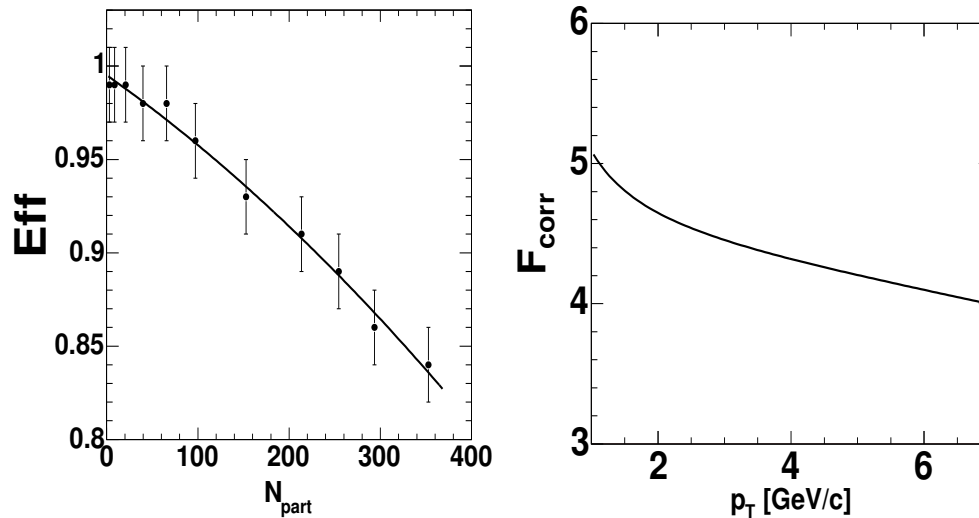


Figure 4.8 Single charged hadron multiplicity dependent DC-PC1-PC3 efficiency (left panel) and the p_T -correction function $F_{corr}(p_T)$ (right panel) for $AuAu$.

CHAPTER 5. Results

5.1 Jet Fragmentation Function in pp Collisions

In order to extract the vacuum jet fragmentation function, we follow the method outlined in Section 2.3: assorted (asymmetric) correlation functions (CFs), like the ones in Fig.(C.2) from Appendix C, are constructed as described in Section 4.2.1. In particular, we use sets of assorted CFs with one hadron (called "trigger") fixed in a given p_T bin and the other hadron (called "associated") scanning the entire accessible p_T region. From these CFs , we extract the dependency on x_E of the away conditional yield, as given by Eq.(4.14), for various values of $\langle p_{Ttrigg} \rangle$. This is presented in Fig.(5.1): the dashed lines are exponential fits and the legend lists the resulting slopes for all four p_T regions of the trigger hadron.

Note that the slope of the vacuum fragmentation function is independent of $\langle p_{Ttrigg} \rangle$ for $p_{Ttrigg} > 3$ GeV/c and equal to $\sim 5 \pm 0.4$. This value agrees with measurements at lower collision energy (CCOR measurements) [3]. So, as expected, *the vacuum fragmentation function is Q^2 and \sqrt{s} independent, as long as p_{Ttrigg} is above a certain threshold, which for $\sqrt{s} = 200$ GeV is in the region 2-3 GeV/c.*

This is easy to understand if we consider the fact that the measured π^0 spectrum in pp collisions [13] has a power-law shape only for $p_T > 3$ GeV/c. The Hagedorn parametrization given in Eq.(5.2) is often used to fit both the low p_T region and the high p_T region of the spectrum. So, $p_T < 2-3$ GeV/c is the region where the soft (non-perturbative) component of the jet fragmentation starts to become significant and triggering on this type of fragments changes the slope of the fragmentation function.

After extracting the x_E slope we use the iterative method presented in the second part of Section 2.3, based on Eq.(2.29), to obtain the p_T dependence

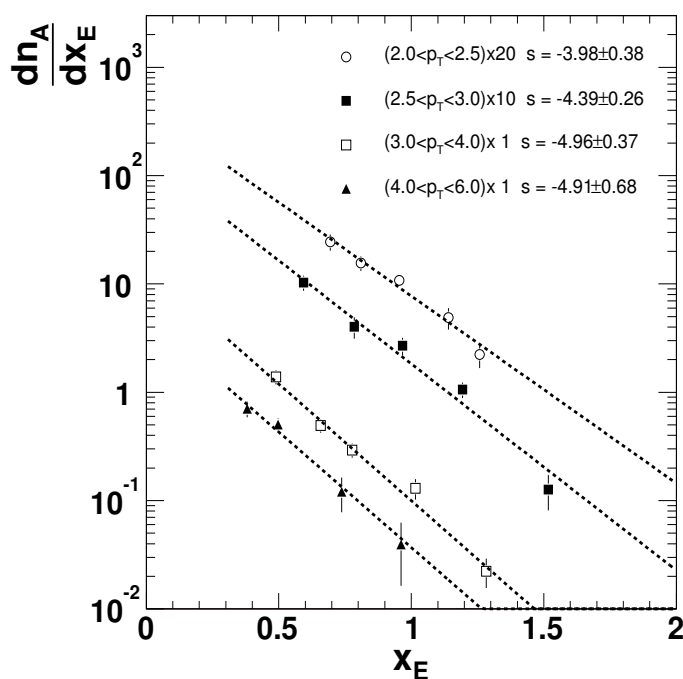


Figure 5.1 Jet fragmentation function in vacuum for various $\langle p_{Ttrigg} \rangle$. Dashed lines represent exponential fits and the resulting slopes are given in the legend.

of $\langle z \rangle$. This will allow us to extract $\langle |k_{Ty}| \rangle$ (which depends on $\langle z_{trigg} \rangle$). The method has two steps:

Extract the final parton spectrum by assuming $1/\langle z \rangle = 6$: We use both a Wood-Saxon corrected power-law parametrization

$$\frac{d\sigma}{p_T dp_T} = \frac{p_0^n}{p_T^n \cdot (1 + e^{-(p_T - p_{cut})/\lambda})} \quad (5.1)$$

and a Hagedorn parametrization

$$\frac{d\sigma}{p_T dp_T} = c \cdot \left(\frac{p_0}{p_0 \exp(-ap_T) + p_T} \right)^n \quad (5.2)$$

of the π^0 spectrum, as shown in Fig.(5.2); they both give a good description, but we choose the first one as it describes slightly better the data and generate a power index closer to the value of $n = 8$, which is what a power-law fit of the high p_T data (> 3 GeV/c) gives.

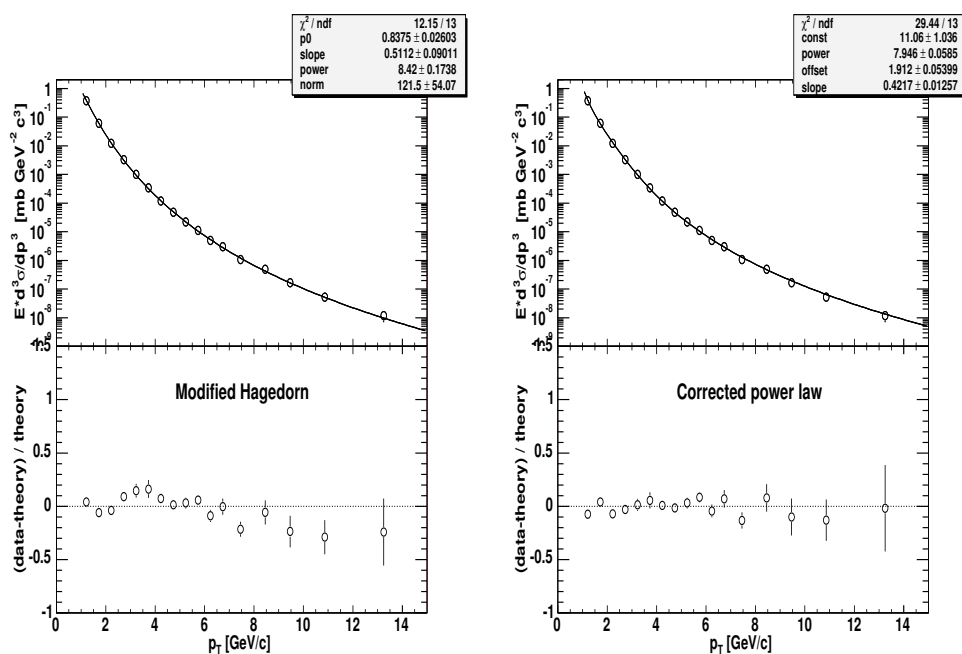


Figure 5.2 The π^0 p_T spectrum from [13] is fitted by the Hagedorn function (left panel) and the Wood-Saxon corrected power law function (right panel).

Then, we assume the same shape (Wood-Saxon corrected power-law) for the final parton spectrum $f_q(p_{Tq})$ and we also use a slope of the fragmentation function of $1/\langle z \rangle = 6$ (which should be close to the correct value because $\langle z \rangle$ is \sqrt{s} independent) to invert Eq.(2.27) and get the parameters describing the parton spectrum (red line in Fig.(5.3)): $n = 8.05 \pm 0.05$, $p_0^n = 11.1 \pm 1.0$, $p_{cut} = 2.70 \pm 0.05 \text{ GeV}/c$, $\lambda = 0.46 \pm 0.01 \text{ GeV}/c$. Now, if we put this parton spectrum back into Eq.(2.28), we get the $\langle z \rangle$ dependency on p_T signified by the line in Fig.(5.4); the shaded area corresponds to a variation of input fragmentation function slope by 17% (one unit).

Extract the p_T dependency of $\langle z_{trigg} \rangle$ by solving analytically Eq.(2.29) for the p_{Ttrigg} values used in the correlation analysis with the parton spectrum derived above. The black squares in Fig.(5.4) represent the results of this procedure. Table 5.1 shows the final results; the error bars on $\langle z_{trigg} \rangle$ are determined from the variation of $\langle x_E \rangle$ within its errors.

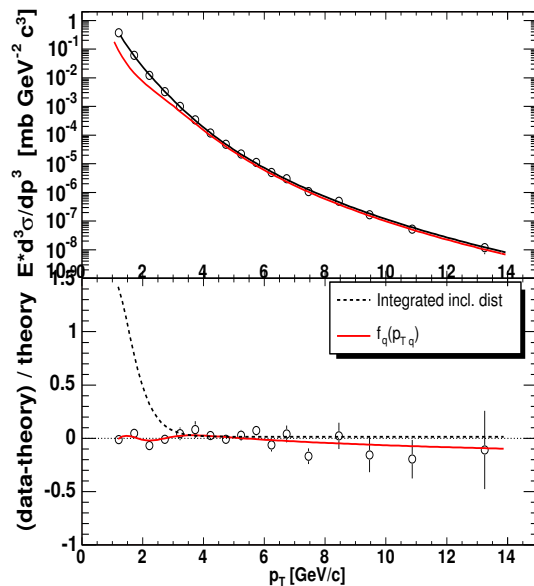


Figure 5.3 Extraction of the parton spectrum (red line) from the measured π^0 spectrum (empty circles). Note the shape deviation below $p_T \sim 2\text{-}3\text{GeV}/c$.

This value of $\langle z_{trigg} \rangle(p_{Ttrigg})$ will be used in the following section to obtain $\langle |k_{Ty}| \rangle$ from fixed CF s. The $\langle z_{trigg} \rangle$ derived above cannot be used for extracting $\langle |k_{Ty}| \rangle$ from assorted CF s; the slope of a "conditional" fragmentation function should be used instead. We will talk more about this in Appendix A.

Table 5.1 p_T dependence of $\langle x_E \rangle$ and $\langle z_{trigg} \rangle$

p_{Ttrigg} (GeV/c)	$1/\langle x_E \rangle$	$\langle z_{trigg} \rangle$
2.0-2.5	-3.98 ± 0.38	0.704 ± 0.016
2.5-3.0	-4.39 ± 0.26	0.729 ± 0.018
3.0-4.0	-4.96 ± 0.37	0.730 ± 0.020
4.0-7.0	-4.91 ± 0.68	0.749 ± 0.019

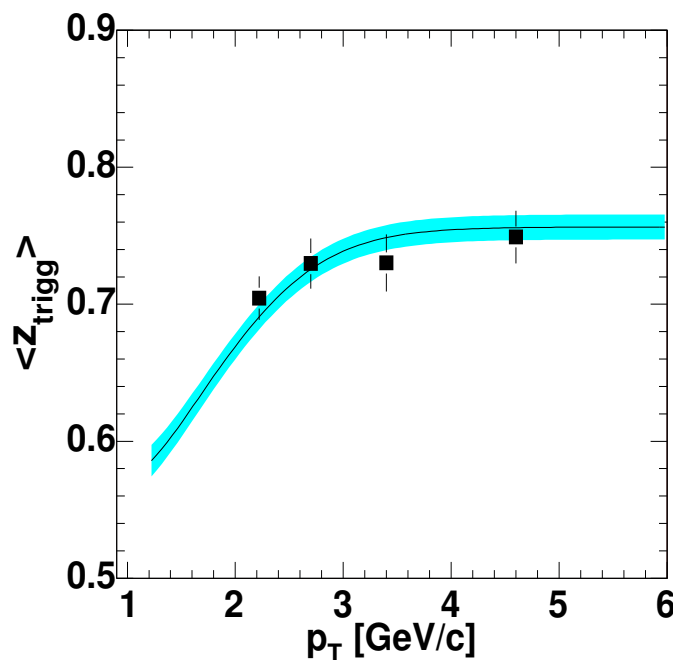


Figure 5.4 The p_T dependence of $\langle z \rangle$: from $1/\langle z \rangle = 6 \pm 1$ assumption (line with shaded band corresponding to the variation by one unit) and after iterative solution (filled squares).

5.2 Jet Shape Parameters

5.2.1 Jet Shape Parameters in pp Collisions

We use the fixed (symmetric) azimuthal correlation functions in pp collisions constructed as explained in Section 4.2.1 and presented in Fig.(C.1) from Appendix C to extract the near and away Gaussian parameters. Table 5.2 shows these parameters for the five p_T bins used and some other relevant parameters (number of pairs in the $dN_{12}/d\phi_1 d\phi_2$ distribution, the χ^2 per degree of freedom of the fit - $ndf = 29$, and the ratio R of number of pairs in the measured and mixed event $\Delta\phi$ distributions).

We derived the jet shape parameters $\langle |j_{Ty}| \rangle$ and $\langle z \rangle \langle |k_{Ty}| \rangle$ from the widths presented in Table 5.2 and the equations derived in Section 2.2. Fig.(5.5) shows the resulting $\langle |j_{Ty}| \rangle$ and $\langle z \rangle \langle |k_{Ty}| \rangle$ dependency on p_T . Points corresponding to $\langle p_T \rangle < 1.5 \text{ GeV/c}$, have not been used because of the resonance decay contamination of the near-angle region; this will be detailed in Ap-

Table 5.2 Table with the fit results for $h^\pm - h^\pm$ fixed correlations in pp collisions as a function of the $\langle p_T \rangle$ of the five p_T bins used.

$\langle p_T \rangle$	1.71	2.21	2.71	3.38	4.70
N_{pairs}	13.1k	2352	555	381	128
χ^2/ndf	1.40	1.67	0.87	0.76	0.31
R	0.9%	1.1%	1.6%	2.7%	8.7%
$\sigma_N(\text{rad})$	0.373 ± 0.017	0.287 ± 0.018	0.233 ± 0.023	0.185 ± 0.016	0.161 ± 0.021
$\sigma_A(\text{rad})$	0.764 ± 0.096	0.642 ± 0.057	0.622 ± 0.103	0.403 ± 0.065	0.336 ± 0.079

pendix D. This Appendix will also present a series of studies that have been done in order to establish the presence of systematic effects or errors in these results. Since no background or method related systematic effects turned up to be significant, the only contribution to the systematic errors of $\langle |j_{Ty}| \rangle$ and $\langle |k_{Ty}| \rangle$ is the measured momentum resolution: $\delta p/p = 0.7\% \oplus 1\% \cdot p$.

Another important cross-check is the extraction of the same jet shape parameters from π^0 - h^\pm azimuthal correlation functions. They are constructed and fitted the same way as h^\pm - h^\pm azimuthal correlation functions and a comparison of the resulting near/away angle widths, as presented in Fig.(5.6), shows a good agreement between these two types of correlations. The number of π^0 s is smaller than that of charged hadrons, so the p_T reach is lower.

We should note here that, because of the low multiplicity environment in pp collisions, the π^0 candidates from the two photon invariant mass spectrum are very clean for $p_T^{\pi^0} > 1\text{GeV}/c$ (the background is less than 10% for the π^0 s used in the above correlations). In order to achieve the same π^0 "cleanness" in central $AuAu$ collisions, we would have to go as high as $p_T^{\pi^0} > 5 - 6\text{GeV}/c$, which was not statistically possible with Run-2 $AuAu$ data. Using p_T bins where π^0 candidates have a large fraction of "background" (photon pairs accidentally falling in the π^0 mass region) in correlation analysis is a difficult task because these "background" π^0 s are formed also by pairing photons from the decay of different π^0 s. Hence, they would also present all the correlations (collective and jet) of the "real" π^0 s in that p_T bin, but corresponding to various other lower p_T bins.

Finally, we get $\langle |k_{Ty}| \rangle$ by dividing $\langle z \rangle \langle |k_{Ty}| \rangle$ with the $\langle z \rangle$ presented in the previous section. Fig.(5.7) shows the $\langle |k_{Ty}| \rangle$ dependence on $\langle p_T \rangle$.

The corresponding standard deviations ($\sqrt{\langle j_T^2 \rangle}$ and $\sqrt{\langle k_T^2 \rangle}$) can be easily calculated using Eq.(2.8).

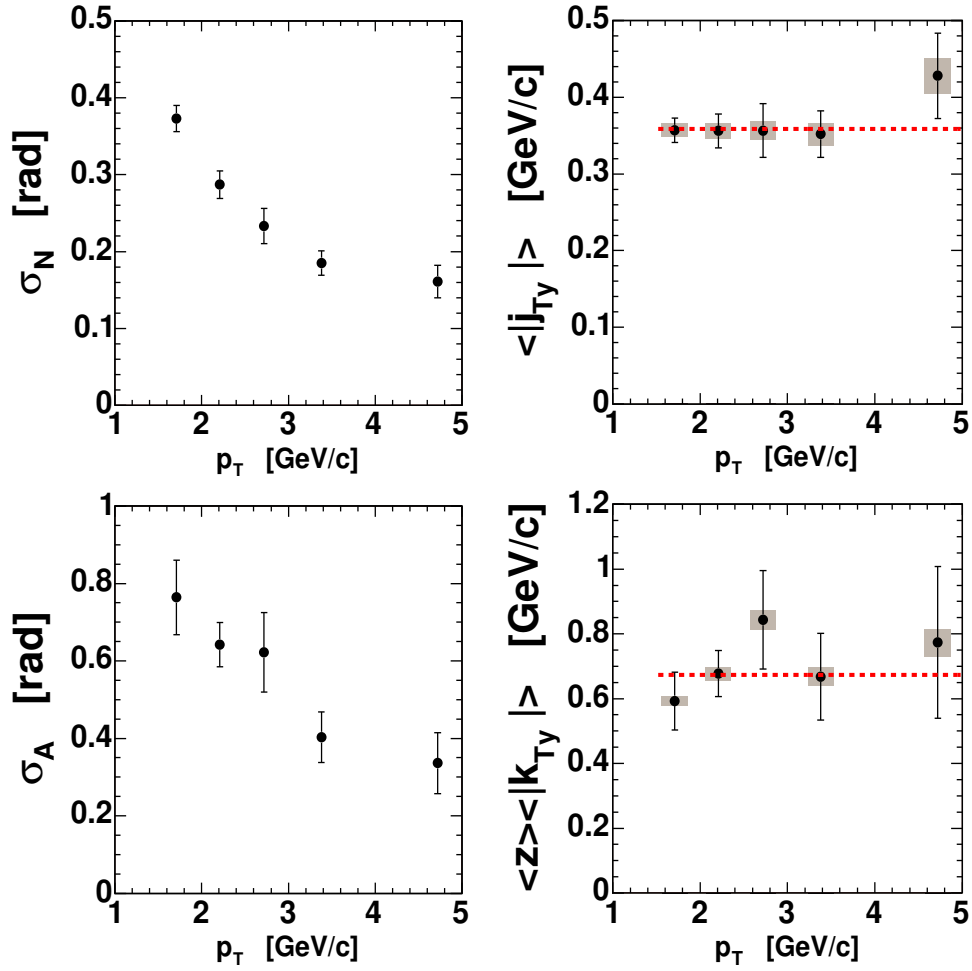


Figure 5.5 Extraction of $\langle |j_{Ty}| \rangle = 359 \pm 11(\text{stat}) \pm 6(\text{syst})$ MeV/c and $\langle z \rangle \langle |k_{Ty}| \rangle = 673 \pm 48(\text{stat}) \pm 16(\text{syst})$ MeV/c. Upper left: near-angle width vs p_T ; Lower left: away-angle width vs p_T ; Upper right: $\langle |j_{Ty}| \rangle$ vs p_T ; Lower right: $\langle z \rangle \langle |k_{Ty}| \rangle$ vs p_T .

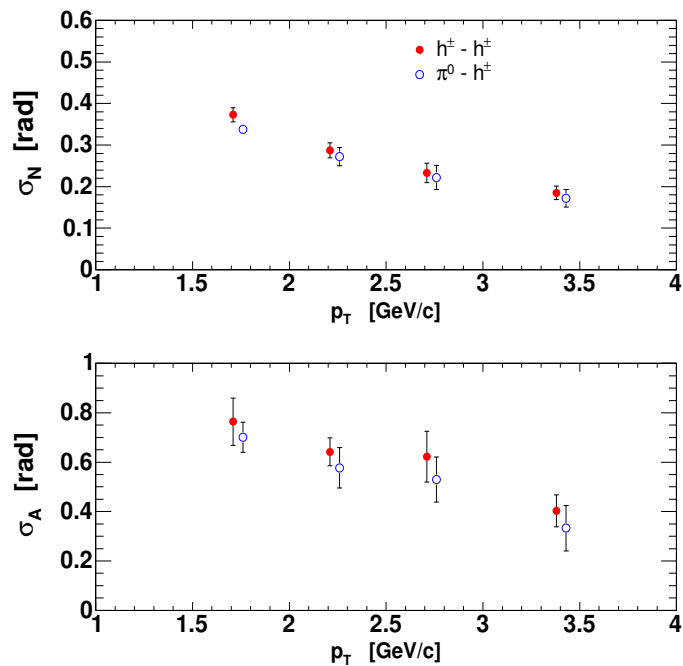


Figure 5.6 Comparison between Gaussian widths in π^0-h^\pm (empty circles) and $h^\pm-h^\pm$ (filled circles) azimuthal correlations.

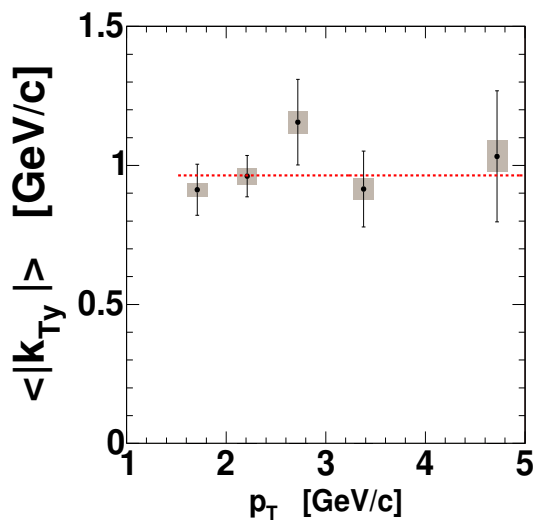


Figure 5.7 Extraction of $\langle |k_{Ty}| \rangle = 964 \pm 49(\text{stat}) \pm 16(\text{syst}) \text{ MeV/c}$: $\langle z \rangle \langle |k_{Ty}| \rangle$ in Fig.(5.5) is divided by $\langle z_{trigg} \rangle$.

Table 5.3 Table with $\langle |j_{Ty}| \rangle$ and $\langle |k_{Ty}| \rangle$ dependency on $\langle p_T \rangle$ in pp collisions. Statistical error first, systematical error second.

$\langle p_T \rangle$	1.71 GeV/c	2.21 GeV/c	2.71 GeV/c
$\langle j_{Ty} \rangle$	$0.357 \pm 0.016 \pm 0.009$	$0.356 \pm 0.022 \pm 0.010$	$0.357 \pm 0.035 \pm 0.012$
$\langle k_{Ty} \rangle$	$0.912 \pm 0.092 \pm 0.024$	$0.962 \pm 0.074 \pm 0.030$	$1.156 \pm 0.154 \pm 0.041$
$\langle p_T \rangle$	3.38 GeV/c	4.70 GeV/c	
$\langle j_{Ty} \rangle$	$0.352 \pm 0.030 \pm 0.014$	$0.428 \pm 0.056 \pm 0.023$	
$\langle k_{Ty} \rangle$	$0.915 \pm 0.136 \pm 0.038$	$1.033 \pm 0.235 \pm 0.057$	

A discussion of the Seagull effect and its influence on these results is presented in Appendix B.

Fits with a constant (dashed lines in the figures mentioned above) give the final results of:

$$\begin{aligned}
 \langle |j_{Ty}| \rangle &= 359 \pm 11(\text{stat}) \pm 6(\text{syst}) \text{ MeV/c} \\
 \langle z \rangle \langle |k_{Ty}| \rangle &= 673 \pm 48(\text{stat}) \pm 16(\text{syst}) \text{ MeV/c} \\
 \langle |k_{Ty}| \rangle &= 964 \pm 49(\text{stat}) \pm 16(\text{syst}) \text{ MeV/c}
 \end{aligned}$$

5.2.2 Jet Shape Parameters in $AuAu$ Collisions

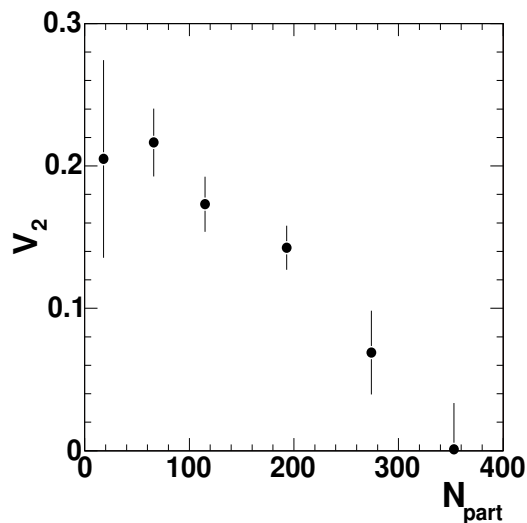
For reasons detailed in Section 4.2.3, the fitting method for $AuAu$ correlation functions is more convoluted than the one for pp (or dAu) correlation functions. In particular, we used the method of minimum jet amplitude point (MJAP) to fit CF s of trigger hadrons with $3 \leq p_{Ttrigg} \leq 5 \text{ GeV/c}$ and associated hadrons with $1.5 \leq p_T \leq 3 \text{ GeV/c}$, as presented in Appendix E.

More precisely, Fig.(E.1) shows the first step of this fit method, which is used to obtain the magnitude V_2 of the collective quadrupole correlation in these CF s. The centrality dependence of V_2 is presented in Fig.(5.8) and in Table 5.4. At this stage we expect that the away Gaussian width and the $\langle z \rangle \langle |k_{Ty}| \rangle$ parameter calculated from it exhibit the same truncation effect seen in simulations (see Fig.(4.7) and comments).

Before going to the second step, let us notice that the fit does not identify any collective quadrupole or away Gaussian correlations in the most central class (0-5%) - both V_2 and S_A are returned null, as shown in the upper left plot of Fig.(E.1), which means that an extreme broadening and/or a complete suppression happens at this centrality. However, it is beyond the statistical errors and the capability of our method to quantify these parameters. This

Table 5.4 V_2 from MJAP method

	0-5%	5-15%	15-25%	25-40%	40-60%	60-90%
V_2	0.00 ± 0.03	0.07 ± 0.03	0.14 ± 0.02	0.17 ± 0.02	0.22 ± 0.02	0.21 ± 0.07

Figure 5.8 V_2 dependency on centrality from MJAP method.

is why we dropped this centrality class from our final results and we show them only in the plots for the first step and only for the near angle.

Keeping only the V_2 from above, we go to the second step of the method, as shown in Fig.(E.2). This provides us with the final results for the jet shape parameters in $AuAu$ collisions. They are presented in Fig.(5.10). A comparison with Fig.(5.9) shows that a certain amount of truncation was indeed present in the first step.

We present the final result as $\langle z \rangle \langle |k_{Ty}| \rangle$ since extracting the fragmentation function in $AuAu$ (and $\langle z \rangle$ from it, as for pp collisions) requires a higher p_T reach than the statistics of Run-2 allows. This remains one of the goals of correlation analyses of future high luminosity PHENIX runs.

Even though the statistical and systematical errors are rather large, the broadening effect seems strong. In order to quantify it, we subtract the $\langle z \rangle \langle |k_{Ty}| \rangle$ value in pp collisions from its four values in $AuAu$ collisions which

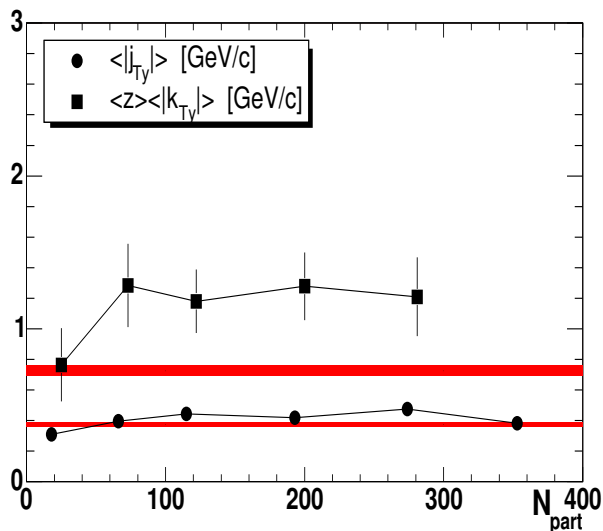


Figure 5.9 Jet shape parameters in $AuAu$ collisions from MJAP method: $\langle |j_{T_y}| \rangle$ with filled circles, $\langle z \rangle \langle |k_{T_y}| \rangle$ with filled squares, and the two bands correspond to the respective values of $\langle |j_{T_y}| \rangle$ and $\langle z \rangle \langle |k_{T_y}| \rangle$ in pp collisions.

exhibit broadening (centrality 5-15%, 15-25%, 25-40%, and 40-60%) and fit with a constant. The resulting overall magnitude of the broadening is $\delta \langle z_{trigg} \rangle \langle |k_{T_y}| \rangle = 0.849 \pm 0.218(stat) + 0.253 - 0.128(syst)$ GeV/c; for the central value, this represents a 3.89σ effect, or a 99.57% confidence level.

Table 5.5 Final jet shape parameters in $AuAu$ collisions. First error is statistical, last two errors are systematical.

	$\langle j_{T_y} \rangle$ [GeV/c]	$\langle z \rangle \langle k_{T_y} \rangle$ [GeV/c]
5-15%	$0.475 \pm 0.050 + 0.024 - 0.173$	$1.609 \pm 0.564 + 0.254 - 0.140$
15-25%	$0.419 \pm 0.043 + 0.021 - 0.145$	$1.614 \pm 0.431 + 0.291 - 0.114$
25-40%	$0.444 \pm 0.046 + 0.022 - 0.158$	$1.503 \pm 0.357 + 0.219 - 0.143$
40-60%	$0.396 \pm 0.048 + 0.020 - 0.152$	$1.628 \pm 0.470 + 0.267 - 0.113$
60-90%	$0.310 \pm 0.046 + 0.016 - 0.095$	$0.766 \pm 0.240 + 0.053 - 0.252$

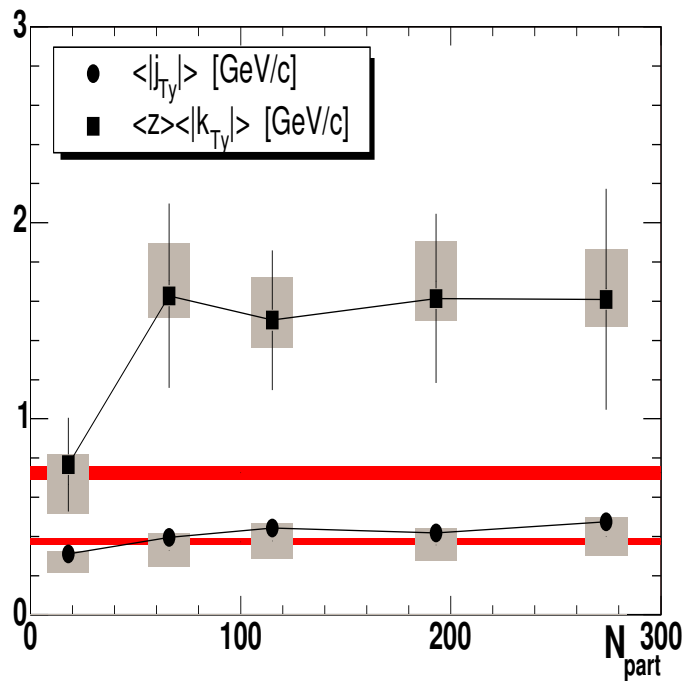


Figure 5.10 Final jet shape parameters in $AuAu$ collisions: $\langle |j_{Ty}| \rangle$ with filled circles, $\langle z \rangle \langle |k_{Ty}| \rangle$ with filled squares, and the two bands correspond to the respective values of $\langle |j_{Ty}| \rangle$ and $\langle z \rangle \langle |k_{Ty}| \rangle$ in pp collisions.

5.3 Jet Conditional Yields in $AuAu$ Collisions

From the same CF s presented in Appendix E, we also extract the near and away Gaussian areas $S_{N,A}$. Then, using the method summarized by Eq.(4.14), we calculate the near and away conditional yields.

Fig.(5.11) shows the conditional yields from the first step of the MJAP procedure. Just as for the away widths, we expect the away conditional yield to be truncated. Hence, we continue with the second step of the method, and the resulting conditional yields are presented in Fig.(5.12). Indeed, a rising trend with centrality can be observed in the second set of results.

For comparison, the pp correlation analysis is repeated for the p_T bins used in $AuAu$ analysis - (1.5-3) GeV/c for the associated hadron and (3-5) GeV/c for the trigger hadron. The resulting near and away conditional yields are shown in Fig.(5.12) with filled triangles.

Table 5.6 gives the final values for the conditional yields in $AuAu$ collisions, while Table 5.5 gives the final values for the jet shape parameters. The first number is the value, the statistical error as reported by the fit comes second, and the systematic errors are the last two numbers.

Table 5.6 Final conditional yields in $AuAu$ collisions. First error is statistical, last two errors are systematical.

	n_N	n_A
5-15%	0.206±0.028+0.010-0.042	0.163±0.057+0.008-0.033
15-25%	0.185±0.019+0.009-0.038	0.156±0.039+0.008-0.033
25-40%	0.190±0.020+0.010-0.041	0.156±0.039+0.008-0.033
40-60%	0.142±0.017+0.007-0.030	0.107±0.035+0.005-0.023
60-90%	0.147±0.014+0.007-0.031	0.109±0.021+0.005-0.024

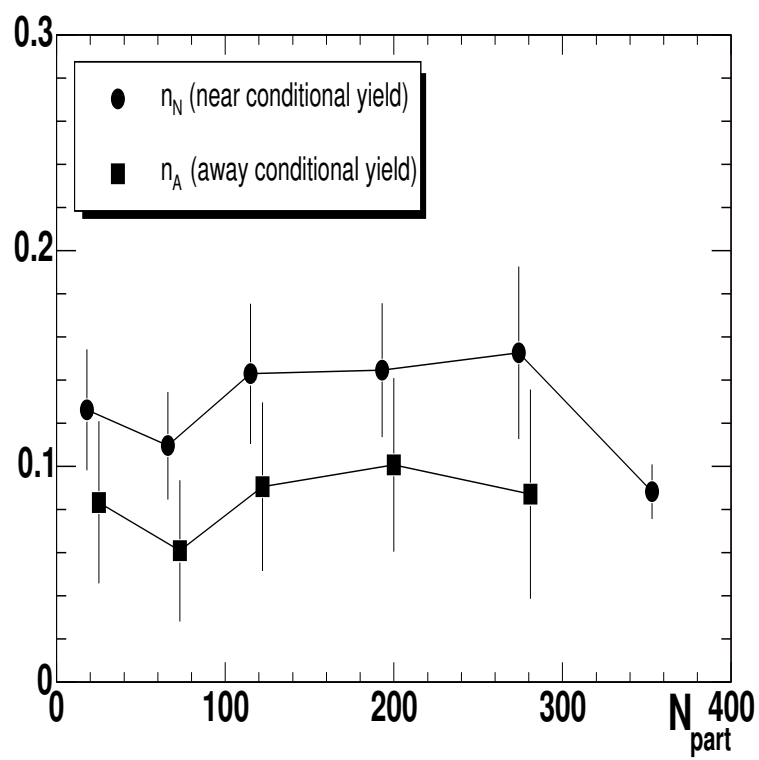


Figure 5.11 Near (filled circles) and away (filled squares) conditional yields from MJAP method.

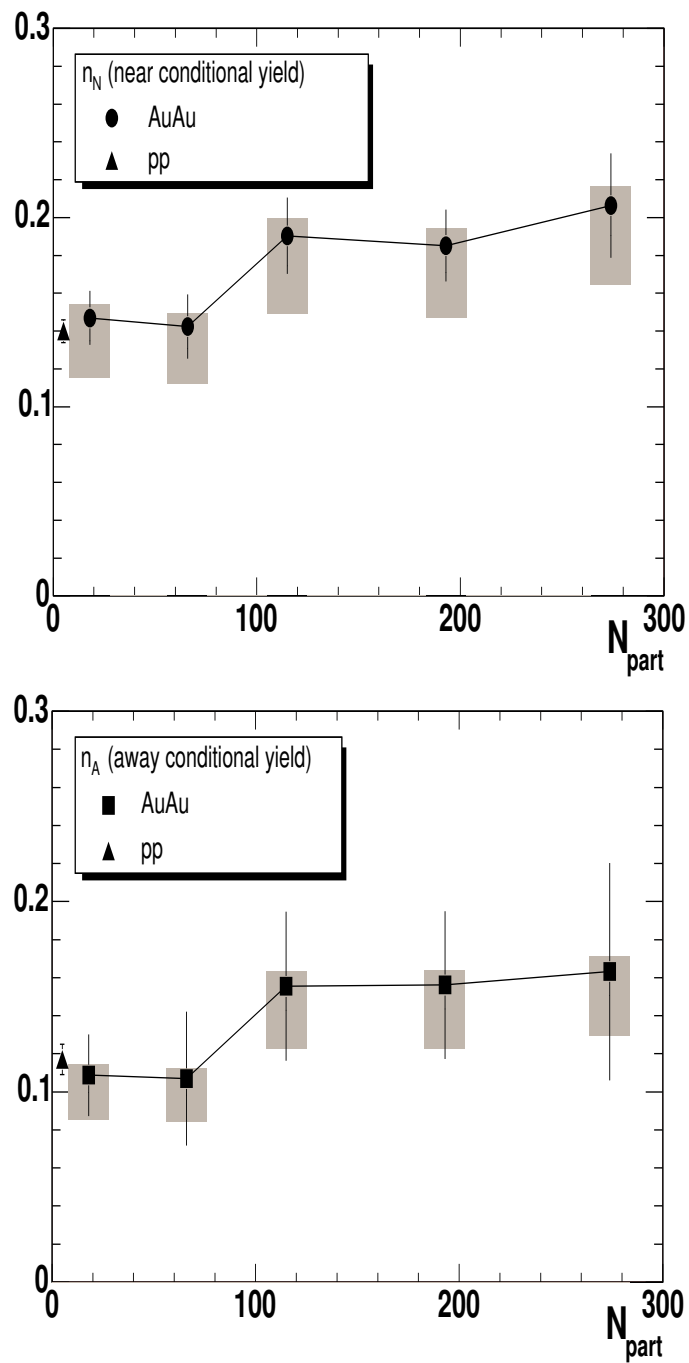


Figure 5.12 Near (filled circles) and away (filled squares) final *AuAu* conditional yields with their corresponding *pp* conditional yields (filled triangles).

CHAPTER 6. Conclusions

We argued that the analysis of two particle azimuthal correlation functions is a method that can go further in the study of hadronic jet properties than the hadronic spectra at high p_T . In particular, a more detailed study of the hadronic jet quenching found in the nuclear modification of high- p_T hadronic spectra of central $AuAu$ collisions can be performed using this method.

We developed the formalism that relates a full set of jet quantities - the shape parameters ($\langle |j_{Ty}| \rangle$ and $\langle |k_{Ty}| \rangle$), the conditional yields ($n_{N,A}$), and the parton fragmentation function (dn_A/dx_E with fixed trigger hadron) - to the parameters extracted from fits of azimuthal correlation functions (Gaussian widths and areas).

The first result from the analysis of pp collisions is the parton fragmentation function, built as the x_E distribution of hadrons associated with a back-to-back trigger hadron of fixed transverse momentum. Exponential fits of this distributions have a constant slope for $p_{Ttrigg} > 3\text{GeV}/c$ and agree with similar measurements performed at lower \sqrt{s} , which is what one expects from the Q^2 and \sqrt{s} independence of the parton fragmentation function. Deviations from this behavior appear for $p_{Ttrigg} < 2 - 3\text{GeV}/c$, which is the soft p_T region of the fragmentation at RHIC energies.

Since we realized that in all previous formulas for $\langle |p_{out}| \rangle$ (originating from the Feynman, Field and Fox formula (1.6)) there was a missing $\langle z \rangle$ term, we developed an iterative method that employed the slope of the above fragmentation function and PHENIX measurements of the π^0 spectrum in pp collisions to get the $\langle z \rangle$ dependence on p_T needed for the extraction of $\langle |k_{Ty}| \rangle$. In the hard region of the fragmentation, we found a constant $\langle z_{trigg} \rangle = 0.74 \pm 0.02$.

The last part of the pp analysis used fixed azimuthal correlation functions to obtain the jet shape parameters in the $\langle p_T \rangle$ region from 1.5 GeV/c to 5 GeV/c. The fragmentation transverse momentum $\langle |j_{Ty}| \rangle$ is p_T independent and \sqrt{s} independent (based on comparisons with lower collision energy ex-

periments); its value is $\langle |j_{Ty}| \rangle = 359 \pm 11(\text{stat}) \pm 6(\text{syst}) \text{ MeV}/c$. The parton transverse momentum $\langle |k_{Ty}| \rangle$ does not have a significant p_T dependence in the region studied and its value is $\langle |k_{Ty}| \rangle = 964 \pm 49(\text{stat}) \pm 16(\text{syst}) \text{ MeV}/c$. Fig.(6.1) shows a comparison of our result with a compilation [34] of k_T measurements in various processes (dilepton, diphoton, dijet); the results are presented using an equivalent quantity, the total transverse momentum of the parton pair:

$$\langle p_{T\text{pair}} \rangle \equiv \sqrt{\pi/2} \sqrt{\langle k_T^2 \rangle} \quad (6.1)$$

This measurement of k_T is an important addition to the \sqrt{s} scan of this quantity, but also an essential ingredient in many theoretical calculations of high- p_T hadronic spectra in pp , pA and AA collisions.

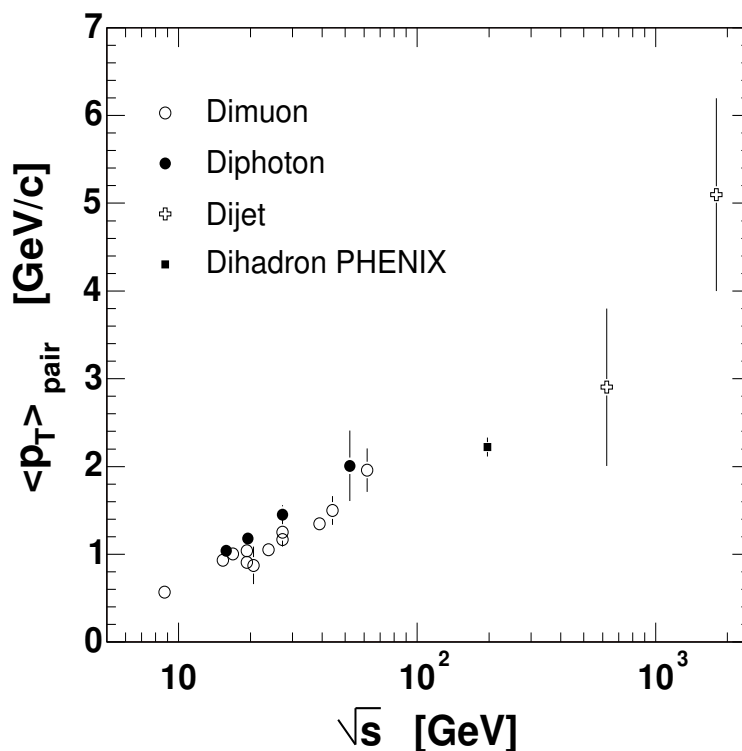


Figure 6.1 Comparison with pp world data on k_T . The PHENIX data point is the filled square at $\sqrt{s} = 200 \text{ GeV}$.

Exactly the same analysis method has been used by the PHENIX collaboration to extract the p_T dependence of $\langle |k_{Ty}| \rangle$ in dAu collisions [24] at the same collision energy. Fig.(6.2) compares the values found in pp and dAu collisions.

As mentioned before (see Section 1.3.2), a k_T enhancement in pA collisions over the value in pp collisions is attributed to the Cronin effect (multiple soft scattering). The present errors on this quantity do not allow a test of the enhancement seen in R_{dAu} (see Fig.(1.4)).

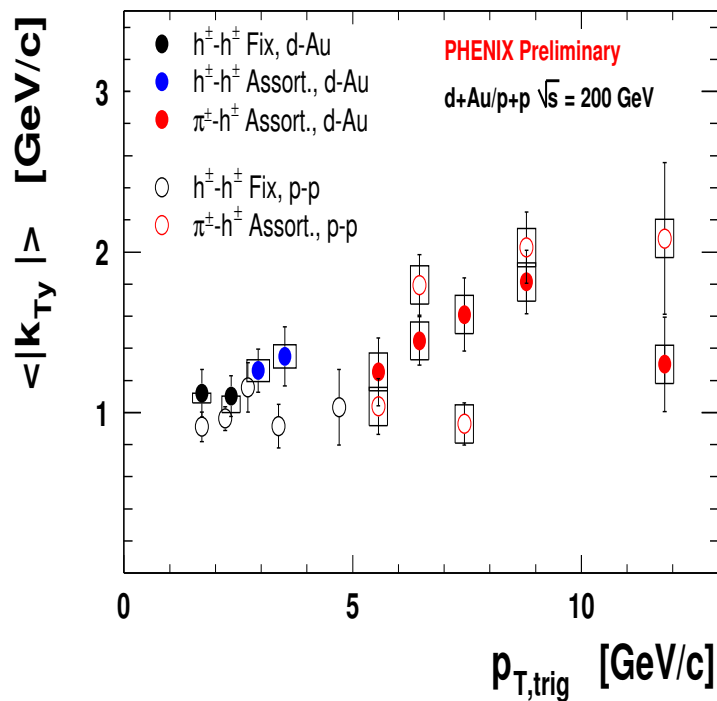


Figure 6.2 Comparison between k_T in pp and dAu collisions. Open circles represent pp values and filled circles dAu values.

The presence of another source of two particle correlations in $AuAu$ collisions, the collective quadrupole correlations, raises a difficult technical problem in extracting the back-to-back (dijet) component of jet induced correlations: due to its broadening and suppression in central collisions, its shape closely resembles the one of collective quadrupole correlations (the Gaussian width becomes larger or equal with the standard deviation of a $\cos(2\Delta\phi)$ modulation), making the simple fit fail. After we review various special methods to deal with this problem, the practical application of two of them is presented. The $\pi/2$ subtraction method is used only to obtain the quadrupole subtracted azimuthal correlation functions ($SCFs$), which we believe to be in-

interesting even without any jet parameters extracted from them because they are the only distributions that allow a visual inspection of the existence of the dijet source. However, with the existing statistics in Run-2 $AuAu$ data, this method proves inefficient in extracting the dijet parameters with reasonable precision. Hence, the method of minimum jet amplitude point (MJAP) is finally used to do the analysis.

Azimuthal correlation functions of trigger hadrons with $3 \leq p_{Ttrigg} \leq 5 \text{ GeV}/c$ and associated hadrons with $1.5 \leq p_T \leq 3 \text{ GeV}/c$ are fitted using the MJAP method and the centrality (N_{part}) dependence of the jet shape parameters and jet conditional yields is obtained, as presented in Figs.(5.10) and (5.12). Even though the current statistical and systematical errors are rather large, we can observe several important trends in the data.

The fragmentation transverse momentum $\langle |j_{Ty}| \rangle$ in $AuAu$ collisions is centrality independent and agrees with the value from pp collisions. This implies that the *measured* fragmentation in $AuAu$ collisions happens in vacuum. On the other hand, the parton transverse momentum $\langle z \rangle \langle |k_{Ty}| \rangle$ (uncorrected for $\langle z \rangle$ due to lack of knowledge about the parton fragmentation function in QCD media) shows a strong enhancement with centrality. This implies a strong interaction (accompanied by energy loss) of energetic partons with the hot, high density QCD medium they travel through. The proposed scenario of skin jet emission by a strongly interacting Quark Gluon Plasma explains these findings. Near angle (around the trigger hadron) jet correlations are dominated by jet fragments originating from hard scattering at the skin of the QGP, since the others are quenched by the plasma and less likely to be detected. In this sense, the centrality independence of $\langle |j_{Ty}| \rangle$ is a trigger bias. However, once we trigger on a high- p_T hadron and search for back-to-back associated hadrons, we pick up those fragments from the fragmentation of partons that travelled through the whole interacting region and hence interacted strongly with the high gluon density plasma.

Another interesting finding lies in the fact that both the near and, even more interestingly, the away conditional yields are increasing slightly with centrality. However, higher p_T R_{AA} measurements and away conditional yields measured by the STAR collaboration [25] show a strong suppression with centrality. If it is true that this suppression at higher p_T is due to energy loss in the QGP, then it must be accompanied by a small enhancement at

somewhat lower p_T based on simple energy conservation considerations. So, as our results indicate, the strong suppression with centrality of the away conditional yield at higher p_T is balanced by the small enhancement with centrality of the away conditional yield at lower p_T .

With the present measurement precision, we can establish the only existence of such important phenomena, like the strong enhancement of the acoplanarity of back-to-back jets with the centrality in $AuAu$ collision, but we cannot make detailed comparisons with existing models of parton energy loss. This will be done with the coming high luminosity run (Run-4 data set) which is already ready to be analyzed at the time we are writing these conclusions.

All these measurements provide more insight into the hadronic jet quenching phenomenon. Together with other observations, like the binary scaling of direct photon [18] and open charmed yields [19] in $AuAu$ collisions, they prove the formation of an extremely dense QCD matter in central $AuAu$ collisions. For example, the GLV (Gyulassy, Levai, Vitev) model of energy loss uses an initial gluon density of $dn/dy \approx 1000$ and an initial energy density of $\epsilon \approx 15 \text{ GeV}/\text{fm}^3$ to describe the observed R_{AA} [37], values which are well above all the lattice QCD results for the quark deconfinement phase transition: $\epsilon_c \approx 1 \text{ GeV}/\text{fm}^3$.

Nonetheless, before we can claim to understand this new state of QCD matter formed in our detectors, a consistent theoretical picture of its dynamics must be found such that spectra, HBT, collective flow, baryon to meson ratio, jet physics and other measurements are *simultaneously* described.

APPENDIX A. Conditional Mean Fragmentation Momentum Fraction

As mentioned already, the $\langle z \rangle$ derived in Section 5.1 can be used to extract $\langle |k_{Ty}| \rangle$ only from fixed azimuthal correlation functions. In assorted correlation functions, with one hadron kept at fixed p_T and the other one allowed to have varying p_T , a different $\langle z \rangle$ has to be used instead. Basically, the $\langle z \rangle$ "inclusive" formula given by Eq.(2.28) has to be replaced by a "conditional" $\langle z \rangle$ formula. The p_{Tt} distribution of the trigger hadron conditioned on a given transverse momentum p_{Ta} of the associated hadron is

$$\begin{aligned} \frac{d^2\sigma}{dp_{Tt}dp_{Ta}} &= \int_{\min(p_{Tt}, p_{Ta})}^{\sqrt{s}/2} f_q(p_{Tq}) \cdot D\left(\frac{p_{Ta}}{p_{Tq}}\right) \cdot D\left(\frac{p_{Tt}}{p_{Tq}}\right) \frac{dp_{Tq}}{p_{Tq}} \\ &= \frac{1}{p_{Tt}} \int_{x_{Tt}}^{p_{Tt}/p_{Ta}} \frac{1}{z_t} f_q\left(\frac{p_{Tt}}{z_t}\right) D(z_t) D\left(\frac{p_{Ta}}{p_{Tt}} z_t\right) dz_t \end{aligned} \quad (\text{A.1})$$

where $z_t \equiv p_{Tt}/p_{Tq}$ and $x_{Tt} \equiv 2p_{Tt}/\sqrt{s}$.

Then, the mean value of trigger hadron momentum fragmentation fraction can be calculated in the same way as Eq.(2.28):

$$\langle z_t \rangle = \frac{\int_{x_{Tt}}^{p_{Tt}/p_{Ta}} f_q\left(\frac{p_{Tt}}{z_t}\right) D(z_t) D\left(\frac{p_{Ta}}{p_{Tt}} z_t\right) dz_t}{\int_{x_{Tt}}^{p_{Tt}/p_{Ta}} \frac{1}{z_t} f_q\left(\frac{p_{Tt}}{z_t}\right) D(z_t) D\left(\frac{p_{Ta}}{p_{Tt}} z_t\right) dz_t} \quad (\text{A.2})$$

Extensive Monte-Carlo simulations were done to test these $\langle z \rangle$ formulas. In particular, Fig.(A.1) shows $\langle z_{trigg} \rangle$ and $\langle z_{assoc} \rangle$ dependence on p_{Tassoc} for fixed $\langle p_{Ttrigg} \rangle = 3.4$ GeV/c. The interesting feature is the variation of $\langle z_{trigg} \rangle$ with p_{Tassoc} . In the leading order, when the two jets in a dijet are balanced ($\vec{p}_{jet1} = \vec{p}_{jet2}$), we expect $z_{trigg} \sim z_{assoc}/p_{Tassoc}$ for fixed p_{Ttrigg} . Next to leading order corrections (k_T effects), taken into account in our simulations, change these relationships, but the general trends remain similar, as the figure shows. Note, for example, that $\langle z_{assoc} \rangle$ becomes equal to $\langle z_{trigg} \rangle$ and consistent (within

the approximations of the simulation) with the "inclusive" $\langle z \rangle$ when p_{Tassoc} crosses the fixed p_{Ttrigg} value.

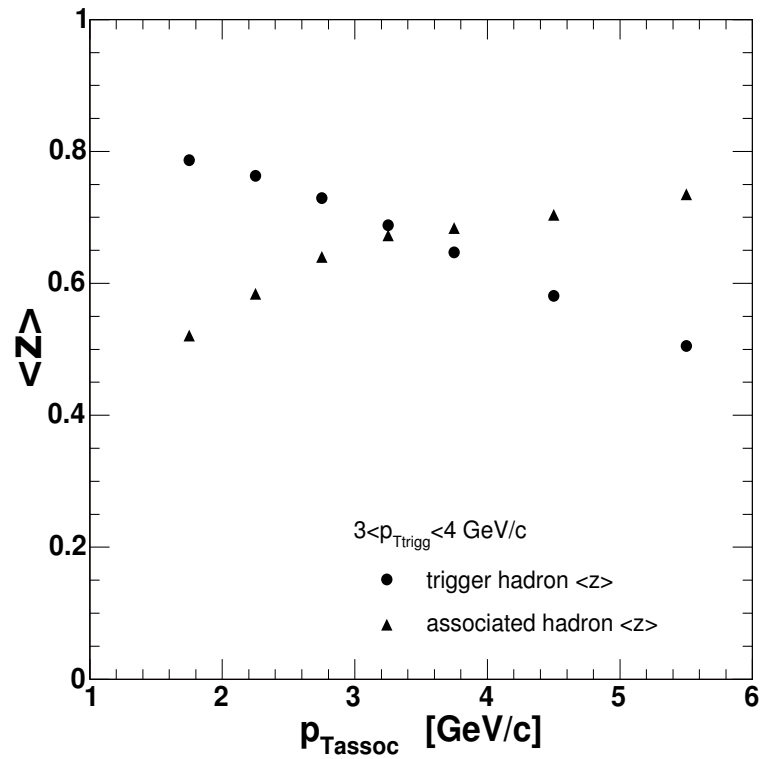


Figure A.1 Monte Carlo simulations of $\langle z_{trigg} \rangle$ and $\langle z_{assoc} \rangle$ dependency on p_{Tassoc} with p_{Ttrigg} kept fixed in 3-4 GeV/c.

APPENDIX B. The Seagull Effect

The Seagull effect [11] is a kinematical effect with simple consequences on the fragmentation of a parton: since a vector's component (j_{Ty}) cannot be larger than vector's magnitude (p_T), there is a **truncation factor** f such that $\langle |j_{Ty}| \rangle < f \cdot \langle p_T \rangle$. This fact will effectively reduce (truncate) the measured $\langle |j_{Ty}| \rangle$ by this factor f for fragments which have transverse momenta close to the true $\langle |j_{Ty}| \rangle$.

This effect can be easily taken into account by using the following fit formula for $\langle |j_{Ty}| \rangle$ vs. $\langle p_T \rangle$:

$$\langle |j_{\perp y}| \rangle = \sqrt{\frac{\pi}{2}} \frac{1}{N} \int_{-f_0}^{+f_0} dj_{\perp} |j_{\perp}| e^{-\frac{j_{\perp}^2}{2\sigma^2}} \quad (\text{B.1})$$

where $f_0 \equiv f < p_{\perp} >$ and $N \equiv \int_{-f_0}^{+f_0} dj_{\perp} \exp(-\frac{j_{\perp}^2}{2\sigma^2})$ is the normalization constant. The fit parameters are the truncation factor f and the standard deviation of the $\langle |j_{Ty}| \rangle$ distribution σ .

We notice that the fit function describes accurately the data, as shown in Fig.(B.1). We also note that only the first data point (which was dropped anyway due to resonance decay contamination) is affected by the Seagull effect; nonetheless, the resulting $\langle |j_{Ty}| \rangle$ from the Seagull fit of all points agrees very well with the $\langle |j_{Ty}| \rangle$ from a fit with a constant above $p_T > 1.5 \text{ GeV}/c$.

Finally, the truncation factor discussed above is $f = 0.497 \pm 0.033$. Interestingly, it is ≈ 0.5 , corresponding to $R \equiv \sqrt{\Delta\phi^2 + \Delta\eta^2} = 0.5\sqrt{2}\sqrt{2} = 1$ which is the typical jet fragmentation cone; the two factors of $\sqrt{2}$ come about from the fact that there are two fragments in the cone and from the similar opening in $\Delta\eta$ (we remind here that these $\langle |j_{Ty}| \rangle$ values have been extracted from an azimuthal correlation function).

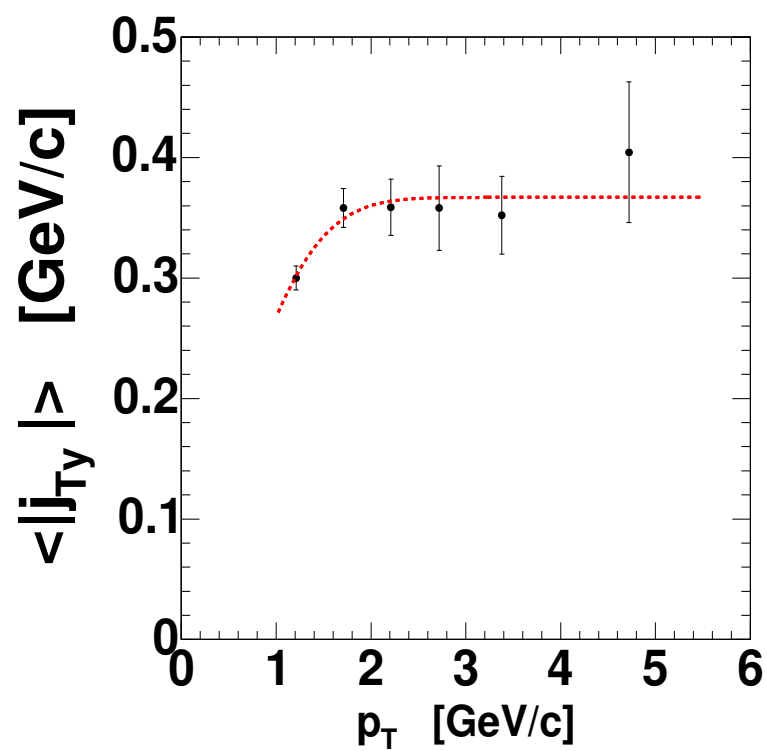


Figure B.1 Seagull fit to $\langle |j_{Ty}| \rangle$ vs $\langle p_T \rangle$. The results are: $\langle |j_{Ty}| \rangle = 367 \pm 15$ MeV/c and $f_{trunc} = 0.497 \pm 0.033$.

APPENDIX C. Correlation Functions in pp Collisions

This Appendix contains plots with $h^\pm - h^\pm$ correlation functions and their fits in pp collisions:

- Fig.(C.1) shows all the fixed (symmetric) CF s in (1-1.5)GeV/c (upper left), (1.5-2)GeV/c (upper right), (2-2.5)GeV/c (middle left), (2.5-3)GeV/c (middle right), (3-4)GeV/c (lower left), and (4-7)GeV/c (lower right).
- Fig.(C.2) shows several examples of assorted (asymmetric) CF s with the trigger hadron in (4-7)GeV/c and the associated hadron in (3.5-4)GeV/c (upper left), (3-3.5)GeV/c (upper right), (2.5-3)GeV/c (lower left) and (2-2.5)GeV/c (lower right). All CF s are normalized to the number of entries in the real $\Delta\phi$ distribution.
- Fig.(C.3) shows x_E distributions in pp collisions for various associated p_T -bins and the trigger p_T -bin in (2.5,3.5)GeV/c. The solid lines correspond to fits with Landau distribution.

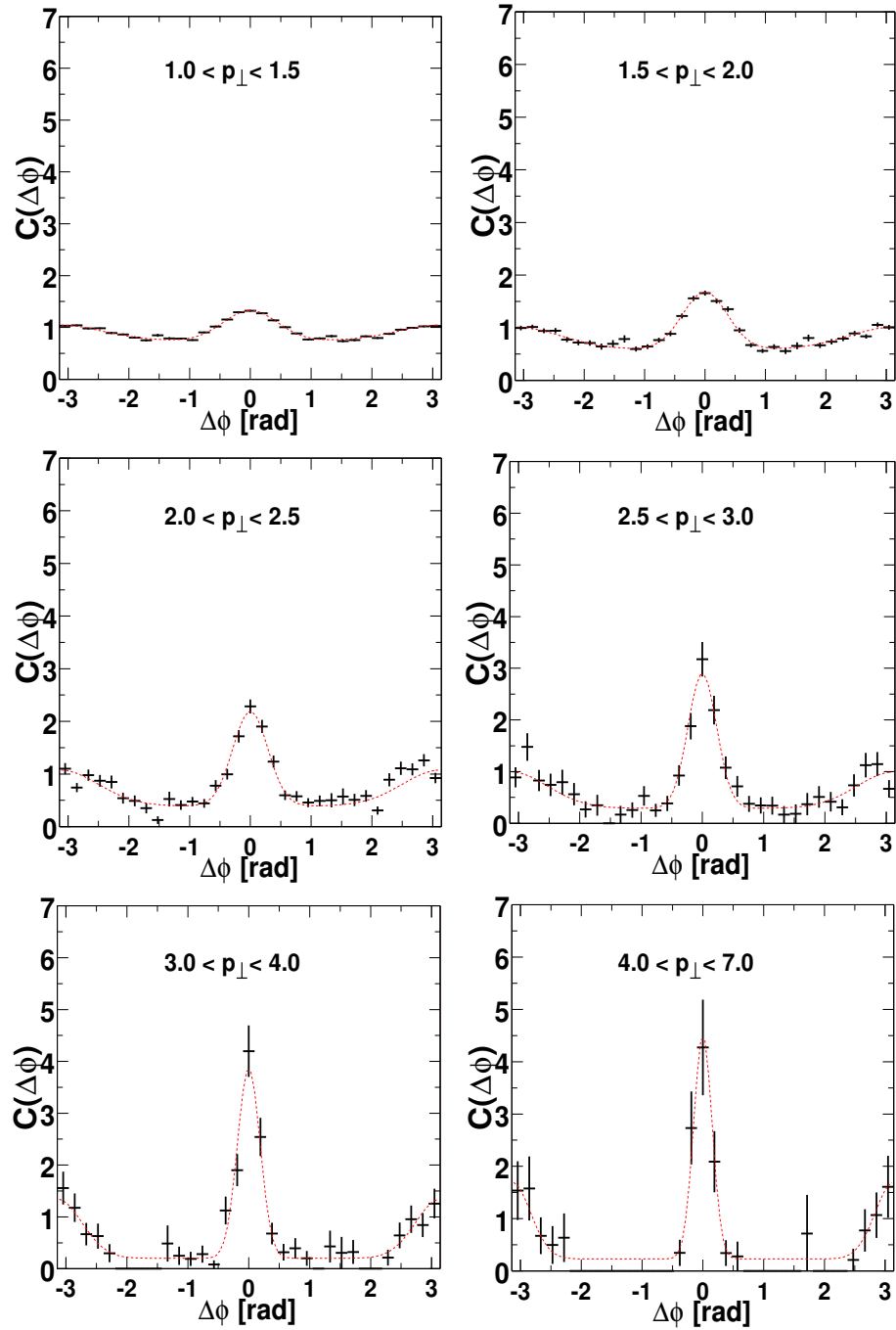


Figure C.1 $h^{\pm} - h^{\pm}$ fixed correlations and fits in pp collisions in (1-1.5)GeV/c (upper left), (1.5-2)GeV/c (upper right), (2-2.5)GeV/c (middle left), (2.5-3)GeV/c (middle right), (3-4)GeV/c (lower left), and (4-7)GeV/c (lower right).

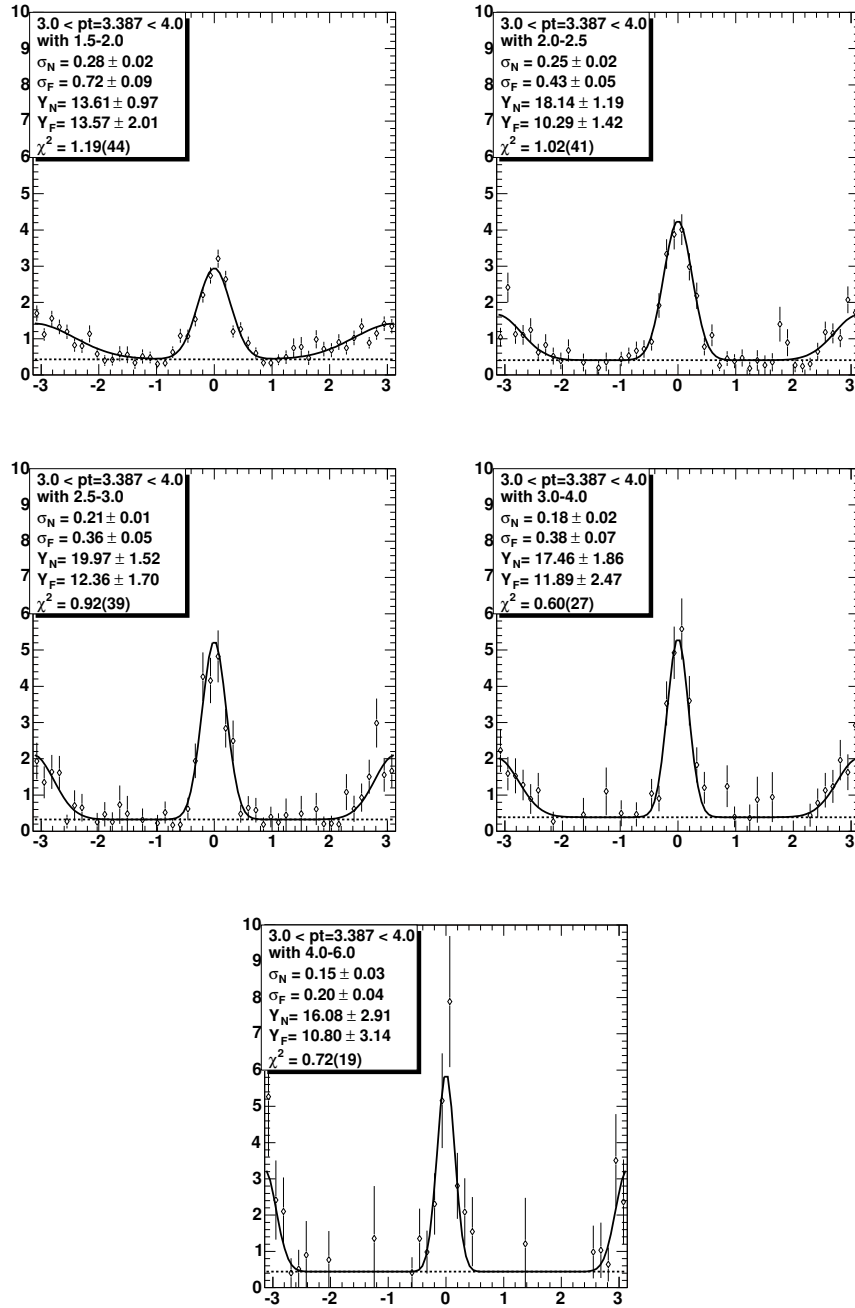


Figure C.2 $h^\pm - h^\pm$ assorted correlations and fits in pp collisions between trigger hadrons in (3-4)GeV/c and associated hadrons in (1.5-2)GeV/c (upper left), (2-2.5)GeV/c (upper right), (2.5-3)GeV/c (middle left), (3-4)GeV/c (middle right), and (4-6)GeV/c (lower).

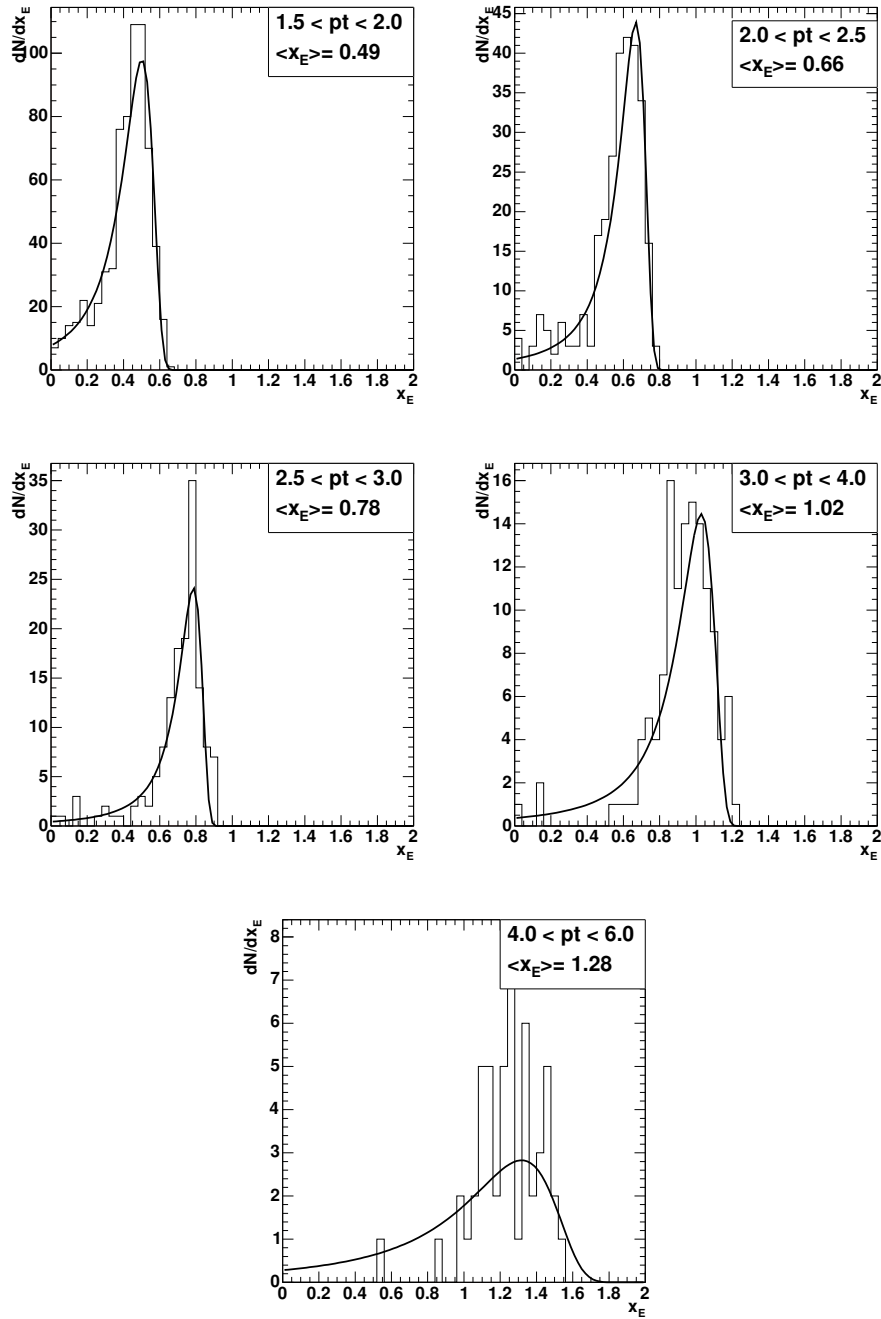


Figure C.3 x_E distributions in pp collisions for various associated p_T -bins and the trigger p_T -bin in $(2.5, 3.5)$ GeV/c. The solid lines correspond to fits with Landau distribution.

APPENDIX D. Systematic Checks of pp Results

In this Appendix we check the existence of systematic effects and errors on the pp jet shape parameters. First, we will assess the impact of the main background correlations. After that, potential effects of the analysis method will be studied. Finally, we will check the Gaussian jet profile assumption. We call "nominal" correlations or quantities those obtained under the standard cuts and methods outlined in Section 4.

D.1 The Systematic Effects of Background Correlations

This study is based on the dependence of near/away widths on the hadron charge (see Fig.(D.1)). Apart from the σ_N value in the first p_T bin, they all agree within one sigma. The probable source of deviations from a jet fragmentation behavior of the near-angle correlation at low p_T is the presence of resonance decays (see Section 2.6).

To study this possibility, we assumed all tracks are charged pions and obtained the invariant mass distribution by subtracting the same charge mass distribution from the opposite charge mass distribution (see upper left panel in Fig.(D.2)). A clear K_0^S mass peak is visible and the fit gives its position at $504 \pm 12 \text{ MeV}$.

Furthermore, we obtained the invariant mass distributions for pairs of hadrons entering into the first three p_T bins of our CF s: this is presented in the other three panels of Fig.(D.2) for pairs within the near-angle cone ($\Delta\phi < 2\sigma_{Near}$) that have p_T in (1,1.5)GeV/c, (1.5,2)GeV/c, and (2,2.5)GeV/c respectively. One can observe that, indeed, for hadron pairs in 1-1.5 GeV/c there is a mass excess (with a small K_0^S peak), while the other p_T bins are basically flat.

Based on this study we decided to derive our final quantities ($\langle |j_{Ty}| \rangle$ and $\langle z \rangle \langle |k_{Ty}| \rangle$) only for $p_T > 1.5 \text{ GeV}/c$. We should note here that the Seagull

effect also starts to affect the widths below 1.5 GeV/c (see Appendix B).

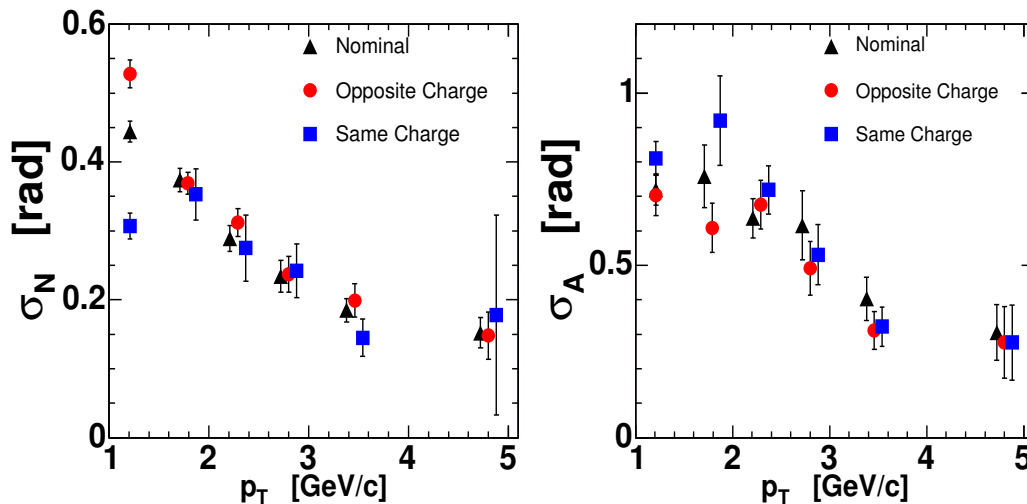


Figure D.1 Charge dependence of the near angle (left panel) and away angle (right panel) widths from fixed- p_T correlations: All Charge Correlations - triangles, Opposite Charge Correlations - circles, Same Charge Correlations - squares. Points are slightly shifted horizontally for visualization.

D.2 The Systematic Effects of the Analysis Method

We vary the characteristics of pairs entering our correlation functions (track cuts, pair cuts, histogram binning) and assess the effect on the quantities extracted by fitting them, in particular the near/away Gaussian widths. The tables below show how they depend on the cuts and binning used to construct the correlation functions: (A) nominal correlation, (B) correlation of track pairs without Pc3 matching cut, (C) correlation of track pairs without pair cuts ("ghost" and minimum radial distance at Pc1 and Pc3), (D) unsigned correlations (between $[0, \pi]$) with 18 bins (nominal correlations have 33 bins).

Case (B) accepts a sizable fraction (especially at lower p_T - about 15%) of background tracks into the correlation function (see the pair multiplicities quoted in parentheses in the first table for "nominal" and "no Pc3 cut" corre-

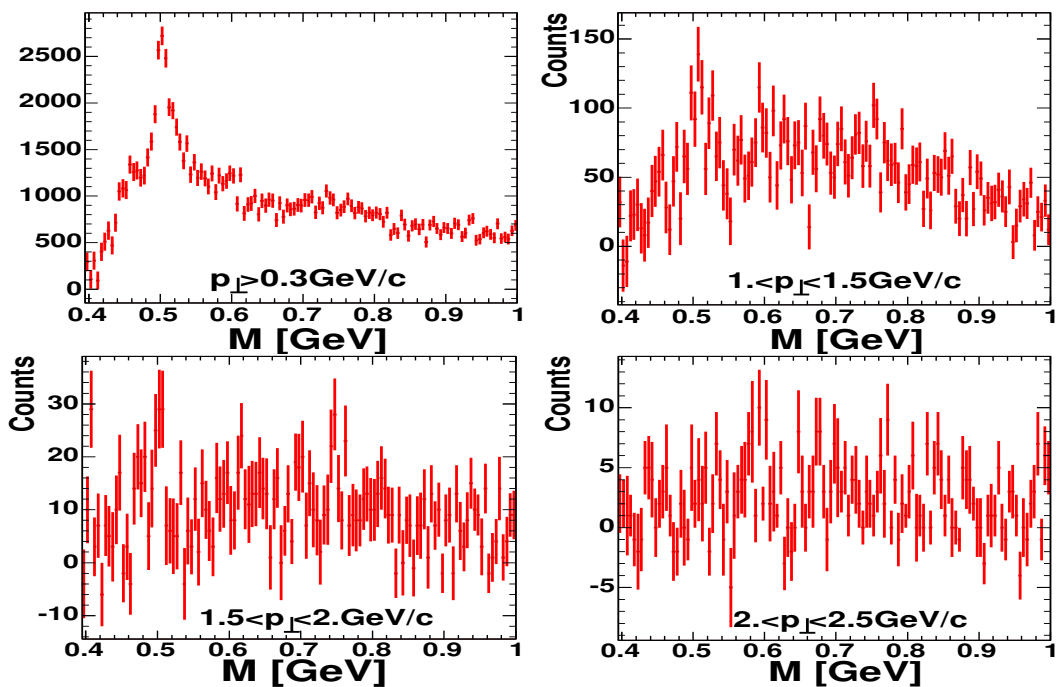


Figure D.2 Upper Left: invariant mass of all track pairs - the K_0^S mass peak is visible at $504 \pm 12 \text{ MeV}$; Upper Right: invariant mass of track pairs within the near-angle cone and with $1 < p_{\perp} < 1.5 \text{ GeV}/c$; Lower Left: invariant mass of track pairs within the near-angle cone and with $1.5 < p_{\perp} < 2 \text{ GeV}/c$; Lower Right: invariant mass of track pairs within the near-angle cone and with $2 < p_{\perp} < 2.5 \text{ GeV}/c$.

lations). Correlations in cases (C) and (D) have similar pair multiplicities as the nominal ones for these p_T bins.

All extracted widths are within one sigma of the nominal quoted value (widths agree within the quoted errors) and there is no visible systematic effect, therefore these become systematic checks of the current errors and no systematic errors should be assigned. These data are plotted in Fig.(D.3).

D.3 Check of the Gaussian Jet Profile Assumption

As mentioned in Section 2.1, we always assumed that jets have a Gaussian profile and approximated the standard deviations of jet $\Delta\phi$ distributions

Table D.1 Table with the **near-angle widths** extracted from fixed- p_T hadron-hadron $h^\pm - h^\pm$ correlations in different analysis conditions (see text).

$p_T(\text{GeV}/c)$	(A)	(B)	(C)	(D)
1.5-2.0	$0.374 \pm 0.017(13k)$	$0.358 \pm 0.017(15k)$	0.373 ± 0.017	0.363 ± 0.018
2.0-2.5	$0.289 \pm 0.019(2.4k)$	$0.307 \pm 0.021(2.6k)$	0.297 ± 0.019	0.289 ± 0.018
2.5-3.0	$0.234 \pm 0.023(555)$	$0.231 \pm 0.022(594)$	0.246 ± 0.023	0.259 ± 0.022
3.0-4.0	$0.185 \pm 0.017(381)$	$0.185 \pm 0.021(395)$	0.191 ± 0.016	0.187 ± 0.017
4.0-7.0	$0.152 \pm 0.022(128)$	$0.121 \pm 0.029(131)$	0.122 ± 0.016	0.158 ± 0.024

Table D.2 Table with the **away-angle widths** extracted from fixed- p_T hadron-hadron $h^\pm - h^\pm$ correlations in different analysis conditions (see text).

$p_T(\text{GeV}/c)$	(A)	(B)	(C)	(D)
1.5-2.0	0.758 ± 0.091	0.750 ± 0.085	0.782 ± 0.095	0.771 ± 0.095
2.0-2.5	0.637 ± 0.057	0.700 ± 0.064	0.660 ± 0.062	0.621 ± 0.062
2.5-3.0	0.616 ± 0.100	0.541 ± 0.089	0.599 ± 0.100	0.493 ± 0.067
3.0-4.0	0.403 ± 0.063	0.365 ± 0.059	0.376 ± 0.059	0.389 ± 0.047
4.0-7.0	0.305 ± 0.081	0.264 ± 0.101	0.288 ± 0.070	0.339 ± 0.076

with the widths of the Gaussian fits to these distributions in both near and away regions. However, it is known that power-law tails are developed at large $\Delta\phi$. We can assess the magnitude of these deviations by comparing the standard deviations (RMS) of the near/away $\Delta\phi$ distributions with the widths of their Gaussian fits. Hence, we subtracted the fitted flat component (F) from each CF in Fig.(C.1) and compute the standard deviation in both $|\Delta\phi| < \pi/2$ and $|\Delta\phi| > \pi/2$ regions. As an example, we show in Fig.(D.4) the CF for $2.0 < p_T < 2.5$ GeV/ c with the flat component subtracted; the dashed lines show the near and away regions used in the RMS calculation. As expected, there is a certain interval in each of the two regions that should be used: it cannot be too small because it would truncate the distribution and produce an smaller RMS , but it also cannot be too large because it would include a contribution from the flat transition region and produce a larger RMS . We present this for the mentioned CF (Fig.(D.4)), by systematically including more $\Delta\phi$ bins into the calculation of the near and away RMS and

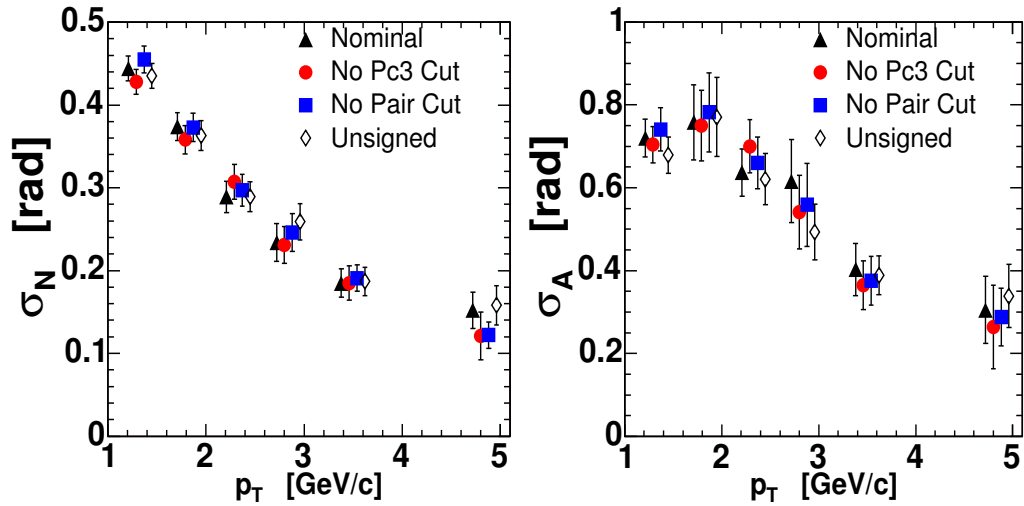


Figure D.3 Systematics of the extracted near angle (left panel) and away angle (right panel) widths from fixed- p_T correlations: Nominal Correlations - black triangles, Correlations without Pc3 Cut - red circles, Correlations without Pair Cuts - blue squares, Unsigned Correlations - black open diamonds. Points are slightly shifted horizontally for visualization.

watching the deviation of the RMS from the gaussian width in terms of its error $((\sigma - RMS)/\delta_\sigma)$ versus the size of the interval used for the RMS calculation in terms of the gaussian width $(Interval(\Delta\phi)/\sigma)$, as shown in Tables D.3 and D.4.

The bottom line is that, for all CF s in Fig.(C.1), the point where the near/away distributions dissolve into the flat component (CF becomes flat - denoted by dashed red lines in Fig.(D.4)) corresponds to an interval of $\approx 5\sigma_N/4\sigma_A$; if we use these $C(\Delta\phi)$ intervals, the resulting RMS always agrees with its corresponding Gaussian width within better than one δ_σ .

Table D.3 Example of **near angle** *RMS* calculation for the *CF* for $2.0 < p_T < 2.5$ GeV/*c*; in this case, the fit result is $\sigma \pm \delta_\sigma = 0.289 \pm 0.019$

Number Of Bins	4	6	8	10	12	14	16
$Interval(\Delta\phi)/\sigma$	2.64	3.96	5.28	6.59	7.91	9.23	10.55
$(\sigma - RMS)/\delta_\sigma$	+3.42	+0.82	-0.72	-2.16	-3.60	-7.19	-4.77
RMS	0.224	0.273	0.302	0.330	0.357	0.425	0.379

Table D.4 Example of **away angle** *RMS* calculation for the *CF* for $2.0 < p_T < 2.5$ GeV/*c*; in this case, the fit result is $\sigma \pm \delta_\sigma = 0.637 \pm 0.057$

Number Of Bins	4	6	8	10	12	14	16
$Interval(\Delta\phi)/\sigma$	1.49	2.09	2.69	3.29	3.89	4.48	5.08
$(\sigma - RMS)/\delta_\sigma$	+5.22	+3.36	+1.71	+1.50	+0.58	+0.34	+1.32
RMS	0.342	0.447	0.541	0.553	0.604	0.618	0.562

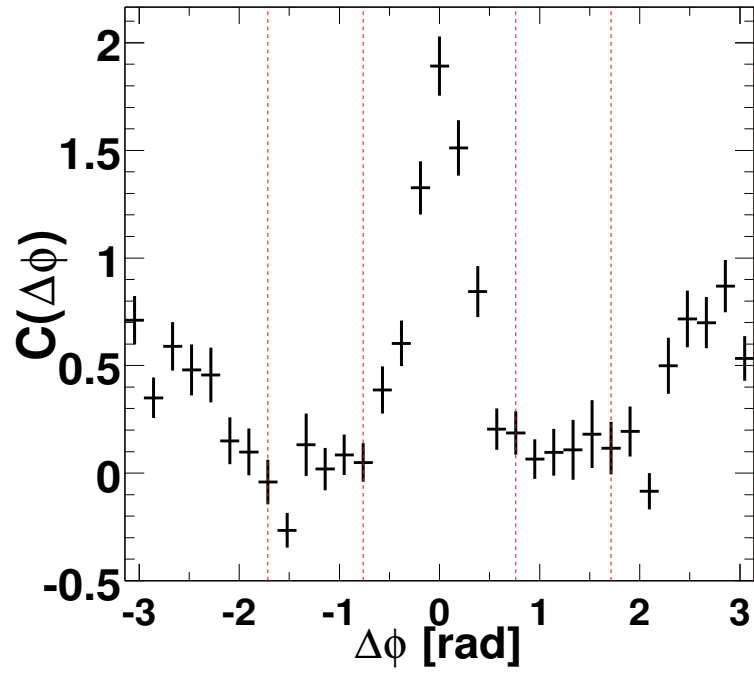


Figure D.4 Example of *RMS* calculation: CF for $2.0 < p_{\perp} < 2.5$ GeV/ c with the flat component subtracted. Dashed lines show the near and away regions used in the *RMS* calculation (see text).

APPENDIX E. Correlation Functions in $AuAu$ Collisions

This Appendix contains plots with $h^\pm - h^\pm$ correlation functions of trigger hadrons with $3 \leq p_{Ttrigg} \leq 5 \text{ GeV}/c$ and associated hadrons with $1.5 \leq p_T \leq 3 \text{ GeV}/c$ in $AuAu$ collisions for the following centrality classes: 0-5%, 5-15%, 15-25%, 25-40%, 40-60%, 60-90%.

Fig.(E.1) shows the first step of the MJAP method (see Section 4.2.3) and Fig.(E.2) shows the second step of this method applied to the same CFs .

Note that the away angle parameters σ_A and S_A are significantly higher after the second step of the fit procedure when compared with their values after the first step.

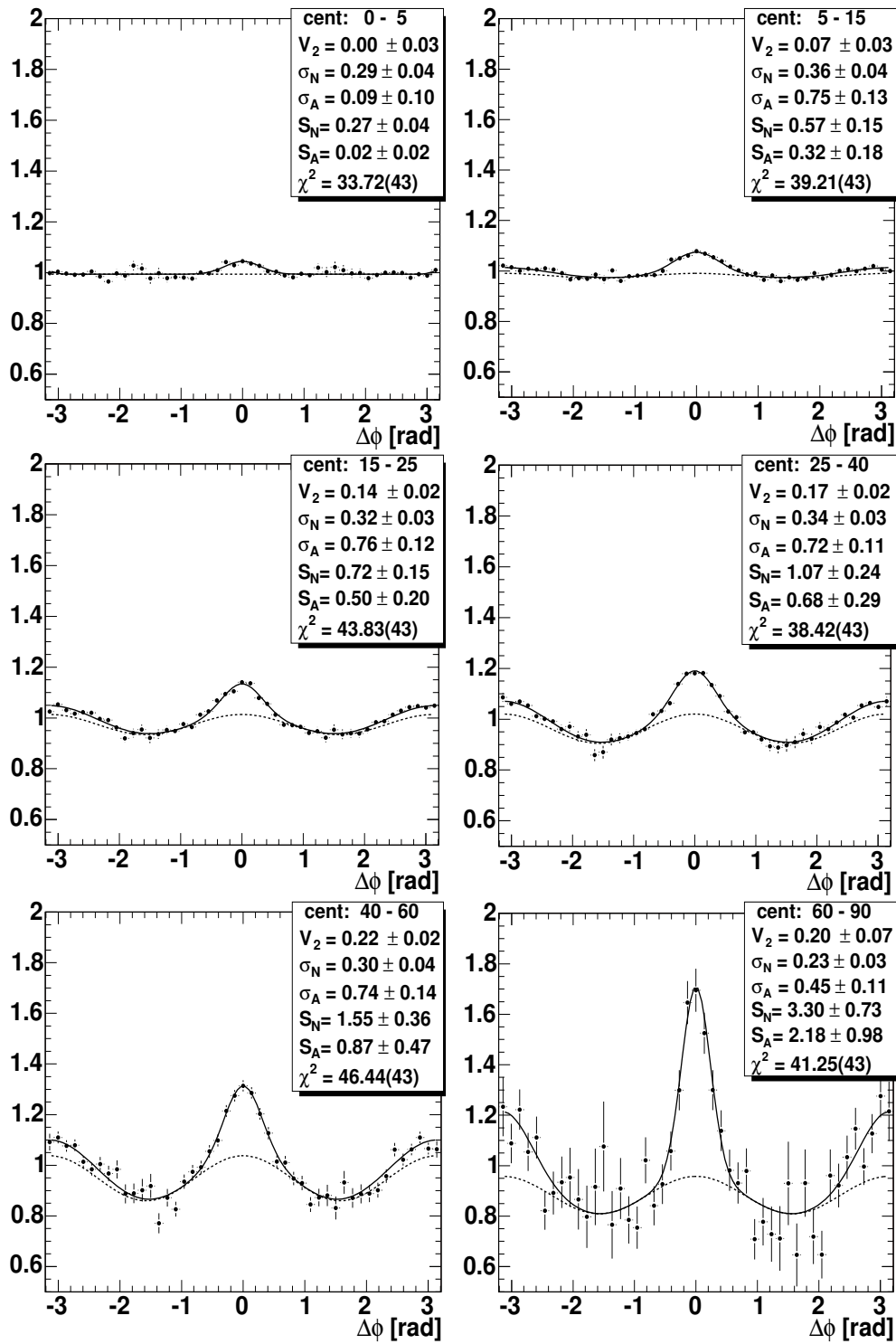


Figure E.1 The first step of the MJAP fit of $h^\pm - h^\pm$ assorted correlations in AuAu collisions between trigger hadrons in (3-5)GeV/c and associated hadrons in (1.5-3)GeV/c.

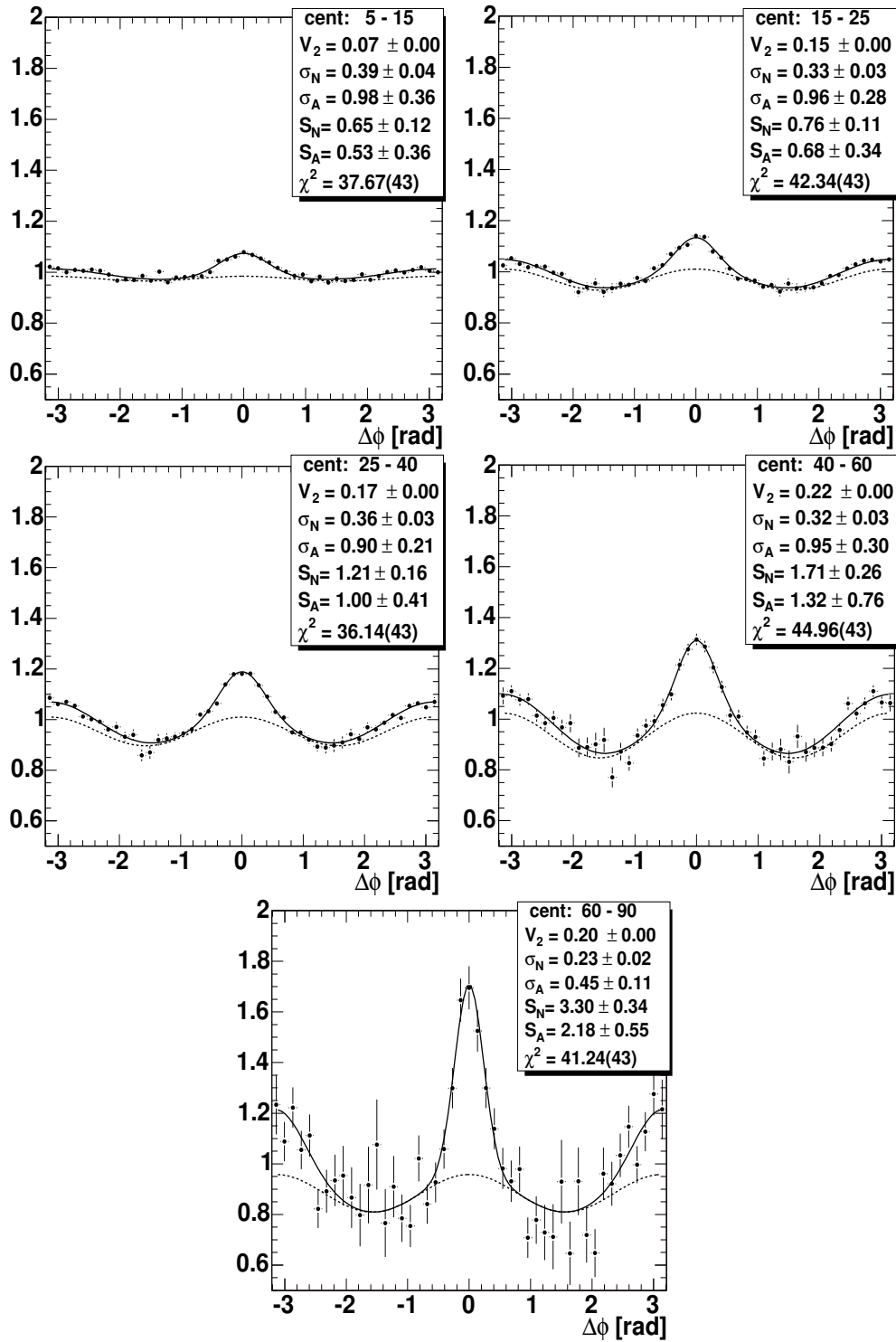


Figure E.2 The second step of the MJAP fit of $h^\pm - h^\pm$ associated correlations in $AuAu$ collisions between trigger hadrons in (3-5)GeV/c and associated hadrons in (1.5-3)GeV/c.

APPENDIX F. Systematic Errors of $AuAu$ Results

In this Appendix we estimate the size of the various systematic errors of the $AuAu$ jet parameters, as presented in Figs.(5.10) and (5.12).

The largest contribution comes from the MJAP fit method used to disentangle the away Gaussian from the quadrupole modulation and, of course, it will affect more the away Gaussian parameters.

The systematic errors have three components, which are added in quadrature:

- the largest contribution comes from the V_2 variation within its errors. This part of the systematic error is estimated by fixing V_2 to $V_2^{MJAP} + \delta V_2^{MJAP}$ and $V_2^{MJAP} - \delta V_2^{MJAP}$ (where by V_2^{MJAP} we mean the V_2 values resulting from the first step of the method and listed in Table 5.4) and repeating the second step. This type of error ranges from 10% to 25% and it is asymmetric - positive variations (above V_2^{MJAP}) have larger impact than negative variations (below V_2^{MJAP}).
- a symmetric systematic error due to momentum resolution ($\delta p/p = 0.7\% + 1\% p$) which has values in the range 2% (peripheral) to 5% (central).
- an overall symmetric 7% systematic error from the other sources. This is the maximum amount of variation when we drop the matching with PC3 of charged hadron tracks. Other variations of the CF characteristics (like the pair cuts) do not produce any significant change of the results.

The tables included below show the variation of the near/away angle widths and areas, as extracted by fitting the azimuthal correlation functions with the MJAP values of V_2 described above. The variations in the jet parameters (shape and conditional yields) listed as systematic errors in Tables 5.5 and 5.6 are calculated from these values by applying the specific formula for each parameter.

Table F.1 Near angle width variation with the amplitude of the quadrupole modulation: $V_2 = V_2^{MJAP}$ in first line, $V_2 = V_2^{MJAP} + \delta V_2^{MJAP}$ in second line, and $V_2 = V_2^{MJAP} - \delta V_2^{MJAP}$ in third line.

60-90%	40-60%	25-40%	15-25%	5-15%
0.305±0.024	0.413±0.031	0.454±0.028	0.426±0.027	0.490±0.036
0.234±0.035	0.299±0.036	0.336±0.035	0.317±0.033	0.360±0.038
0.255±0.031	0.343±0.033	0.384±0.029	0.356±0.029	0.410±0.033

Table F.2 Away angle width variation with the amplitude of the quadrupole modulation: $V_2 = V_2^{MJAP}$ in first line, $V_2 = V_2^{MJAP} + \delta V_2^{MJAP}$ in second line, and $V_2 = V_2^{MJAP} - \delta V_2^{MJAP}$ in third line.

60-90%	40-60%	25-40%	15-25%	5-15%
0.468±0.082	0.786±0.163	0.773±0.123	0.777±0.125	0.823±0.174
0.455±0.106	0.951±0.301	0.933±0.123	0.959±0.278	0.983±0.194
0.558±0.093	0.940±0.211	0.897±0.215	0.937±0.175	0.979±0.362

Table F.3 Near angle area variation with the amplitude of the quadrupole modulation: $V_2 = V_2^{MJAP}$ in first line, $V_2 = V_2^{MJAP} + \delta V_2^{MJAP}$ in second line, and $V_2 = V_2^{MJAP} - \delta V_2^{MJAP}$ in third line.

60-90%	40-60%	25-40%	15-25%	5-15%
4.642±0.369	2.404±0.238	1.723±0.151	1.101±0.094	0.915±0.102
3.842±0.350	1.994±0.230	1.423±0.129	0.919±0.090	0.765±0.089
4.679±0.377	2.456±0.258	1.770±0.151	1.164±0.103	0.973±0.109

Table F.4 Away angle area variation with the amplitude of the quadrupole modulation: $V_2 = V_2^{MJAP}$ in first line, $V_2 = V_2^{MJAP} + \delta V_2^{MJAP}$ in second line, and $V_2 = V_2^{MJAP} - \delta V_2^{MJAP}$ in third line.

60-90%	40-60%	25-40%	15-25%	5-15%
3.443±0.559	1.808±0.493	1.402±0.292	0.935±0.193	0.725±0.211
2.843±0.501	1.498±0.470	1.162±0.255	0.775±0.130	0.605±0.192
3.472±0.578	1.862±0.515	1.460±0.314	0.991±0.206	0.788±0.230

BIBLIOGRAPHY

- [1] B. Alper, *et al.* Nucl. Phys. **B** 87 (1975) 19;
- [2] A.L.S. Angelis, *et al.* Phys. Lett. **B** 79 (1978) 505;
- [3] A.L.S. Angelis, *et al.* Nucl. Phys. **B** 209 (1982) 284;
- [4] A.L.S. Angelis, *et al.* Phys. Scripta 19 (1979) 116;
- [5] A.L.S. Angelis, *et al.* Phys. Lett. **B** 97 (1980) 163;
- [6] A.L.S. Angelis, *et al.* Nucl. Phys. **B** 209 (1982) 284;
- [7] M. Della Negra, *et al.* Nucl. Phys. **B** 127 (1977) 1;
- [8] C. Kourkoumelis, *et al.* Z. Phys. **C** 5 (1980) 95;
- [9] C. Stewart, *et al.* Phys. Rev. **D** 42 (1990) 1385; M.D. Corcoran, *et al.* Phys. Lett. **B** 259 (1991) 209; D. Naples, *et al.* Phys. Rev. Lett. 72 (1994) 2341;
- [10] D. Antreasyan, *et al.* Phys. Rev. **D** 19 (1979) 764;
- [11] Phys. Lett. **B** 320 (1994) 411;
- [12] K. Adcox, *et al.* Phys. Rev. Lett. 88 (2002) 192302; S.S. Adler, *et al.* nucl-ex/0401003 (submitted to PRL);
- [13] S.S. Adler, *et al.* Phys. Rev. Lett. 91 (2003) 241803;
- [14] K. Adcox, *et al.* Phys. Rev. Lett. 88 (2002) 022301; K. Adcox, *et al.* Phys. Lett. **B** 561 (2003) 82; S.S. Adler, *et al.* Phys. Rev. Lett. 91 (2003) 072301;
- [15] S.S. Adler, *et al.* Phys. Rev. **C** 69 (2004) 034909;

- [16] S.S. Adler, *et al.* Phys. Rev. Lett. 91 (2003) 072303 ;
- [17] S.S. Adler, *et al.* Phys. Rev. Lett. 91 (2003) 182301; K. Adcox, *et al.* Phys. Rev. Lett. 89 (2002) 212301;
- [18] J. Frantz, Quark Matter 2004 (Oackland) Proceedings, nucl-ex/0404006;
- [19] K. Adcox, *et al.* Phys. Rev. Lett. 88 (2002) 192303; S. Kelly, Quark Matter 2004 (Oackland) Proceedings, nucl-ex/0403057;
- [20] P. Stankus, PHENIX Analysis Note (internal document);
- [21] N. Ajitanand, *et al.* PHENIX Analysis Note AN237 (internal document);
- [22] J. Jia, *et al.* PHENIX Analysis Note AN179 (internal document); J. Jia, Ph.D. Thesis, 2003, "High Transverse Momentum Charged Hadron Suppression in AuAu Collisions at Center of Mass Energy $\sqrt{s_{NN}} = 200$ GeV";
- [23] Nucl. Instr. and Meth., **A** 499 (2003) 469-593;
- [24] J. Rak, Quark Matter 2004 (Oackland) Proceedings, hep-ex/0403038;
- [25] C. Adler, *et al.* Phys. Rev. Lett. 90 (2003) 082302;
- [26] C. Adler, *et al.* Phys. Rev. Lett. 92 (2004) 062301;
- [27] J.W. Harris, B. Muller, Annual Review of Nuclear and Particle Science 46 (1996) 71;
- [28] J.D. Bjorken, Phys. Rev. **D** 179 (1969) 1547;
- [29] S.M. Berman, J.D. Bjorken, J.B. Kogut, Phys. Rev. **D** 4 (1971) 3388;
- [30] R.D. Field, R.P. Feynman, G.C. Fox, Phys. Rev. **D** 18 (1978) 3320;
- [31] R.F. Calahan, K.A. Geer, J. Kogut, L. Susskind, Phys. Rev. **D** 11 (1975) 1199;
- [32] J.F. Owens Reviews of Modern Physics Vol.59, No.2 (1987);
- [33] N.A. McCubbin Reports on Progress in Physics Vol.44, No.10 (1981);
- [34] L. Apanasevich, *et al.* Phys. Rev. **D** 59 (1999);

- [35] J.D. Bjorken, preprint Fermilab-Pub-82/59-THY (1982);
- [36] M. Gyulassy, X.-N. Wang, M. Plumer Phys. Lett. **B** 243 (1990) 432; Nucl. Phys. **B** 351 (1991) 491; Phys. Rev. Lett. 68 (1992) 1480; Nucl. Phys. **B** 480 (1994) 583;
- [37] I. Vitev and M. Gyulassy, Phys. Rev. Lett. 89 (2002) 252301;
- [38] R. Baier, Yu.L. Dokshitzer, A.H. Mueller, D. Schiff, S. Peigne Phys. Lett. **B** 345 (1995) 277; Nucl. Phys. **B** 483 (1997) 291; Nucl. Phys. **B** 484 (1997) 265; Phys. Rev. **C** 58 (1998) 1706;
- [39] Borghini, *et al.* Phys. Rev. **C** 62 (2000) 034902;
- [40] F. Karsch, Nucl. Phys. **A** 698 (2002) 199; Z. Fodor and S.D. Katz, JHEP 03 (2002) 014;
- [41] R.J. Glauber, "High Energy Collision Theory" in Lectures in Theoretical Physics, vol.1; W.E. Brittin and L.G. Duham (eds.), Interscience, New York, 1959;
- [42] L.V. Gribov, E.M. Levin and M.G. Ryskin, Phys. Rept. 100 (1983) 1; A.H. Mueller and J. Qiu, Nucl. Phys. **B** 268 (1986) 427; J.P. Blaizot and A.H. Mueller, Nucl. Phys. **B** 289 (1987) 847; L. McLerran and R. Venugopalan, Phys. Rev. **D** 49 (1994) 2233, 3352, **D** 50 (1994) 2225;